Fachbereich Physik
Universität Dortmund
Lehrstuhl Experimentelle Physik V

Search for High Energy Neutrinos from Generic AGN classes with AMANDA-II

Dissertation zur Erlangung des Doktorgrades

vorgelegt von

Andreas Groß

Dortmund, Februar 2006

Contents

1

Introduction

Astronomy was integrated in modern science by the assumption that the same laws of nature are valid on Earth and in space. Until the beginning of the 19th century, all astronomical observations were made with optical light only. The invention of the telescope in the 17th century lead to improvement thereafter. The first extension of the use of messengers was the detection of infrared light from the Moon in 1856 and from stars in the beginning of the 20th century [Wal00]. In the following, astronomical observations were rapidly extended to all photon energies.

The field of neutrino astronomy is extending astronomical observations to neutrinos as new messenger particles. It is motivated by the ideal propagation properties of neutrinos through space. Due to their small cross sections with matter, absorption and deflection are negligible and neutrinos propagate from the inner source region directly to the observer. The existence of the measured flux of charged Cosmic Rays motivates the expectation of the emission of detectable neutrino fluxes. Due to the propagation properties of neutrinos and the predicted correlations to other particle fluxes, neutrino astronomy has the capability to solve the challenging question of the origin of Cosmic Rays. However, the small cross sections result in substantial requirements for the detection of astrophysical neutrinos. Very large instrumented volumes are necessary to provide the observer with sufficiently high event rates. The currently most sensitive neutrino telescope is the Antarctic Muon And Neutrino Detector Array (AMANDA) at the geographic South Pole with a geometric volume of 0.016 km^3. The AMANDA detector is operating in its final configuration (AMANDA-II) since the year 2000 and has measured the atmospheric neutrino spectrum up to an energy of 300 TeV. However, up to now no astrophysical sources of high energy neutrinos have been detected by AMANDA.

The main aim of this thesis is the improvement of the sensitivity to astrophysical sources of high energy neutrinos by the application of new analysis techniques. In photon astronomy, the source stacking method is commonly used in order to improve the sensitivity by the evaluation of the cumulative signal of samples of generic

sources. In this thesis, the source stacking method is applied to neutrino astronomy for the first time. Here, as neutrino source candidates Active Galactic Nuclei (AGN) are considered. Therefore, samples of various AGN classes are selected with respect to their expected neutrino production according to phenomenological principles. The derived samples are analyzed for a high energy neutrino flux using data collected by AMANDA.

This thesis starts with a review of the basic concepts of Astroparticle Physics including an introduction to neutrino astronomy (Chapter 2). Then, a detailed discussion of AGN properties is given with emphasis on their possible neutrino emission (Chapter 3). A systematic classification identifies generic AGN samples of promising candidate sources. It is shown that source stacking can improve the sensitivity to generic AGN classes with respect to standard methods. In Chapter 4, a description of the AMANDA neutrino telescope and a review on its properties is given. Then, the generic AGN classes are analyzed using data collected by AMANDA (Chapter 5). Two data sets are considered for the analysis. In a first step, the source stacking analysis is established on data collected by AMANDA-II in the year 2000. Then, the method is applied to the currently most sensitive data set, which has been collected in the years 2000-2003. The analysis of galactic candidate sources is discussed (Chapter 6). In addition to the method of stacking of permanent sources, a time-dependent analysis of single sources is considered. An example for such an analysis is given by the analysis for periodic neutrino emission from the Crab Pulsar. Finally, the results of this thesis are summarized and a short outlook is given on possible extensions of the source stacking method and its application to the IceCube neutrino telescope currently under construction (Chapter 7).

2

Basic concepts of Astroparticle Physics

While the first observations of particles reaching the Earth from space were made in 1912, Astroparticle Physics has been established as an independent field of physics only recently.

The motivation for research in this field is bimodal. Firstly, the particles may be used as astronomical messengers to provide information about their production site. Secondly, the flux of high energy particles provides a natural laboratory to study the properties of these particles. The first is called the *astronomical motivation*, the latter the *particle physics motivation* of Astroparticle Physics.

2.1 Particle interactions in Astroparticle Physics

Before the central observations in Astroparticle Physics are reviewed, some interactions are briefly presented which are relevant for various topics in Astroparticle Physics.

2.1.1 Pion production and decay

The production of pions by the interaction of high energy protons with other particles, including photons, protons and heavier nuclei is important in Astroparticle Physics. Close to the threshold of pion production, the production and subsequent decay of the Δ^+ resonance is dominant:

$$p\gamma \rightarrow \Delta^+ \tag{2.1}$$

$$pp \rightarrow \Delta^+ p \tag{2.2}$$

$$\Delta^+ \rightarrow \begin{cases} \pi^+ n \\ \pi^0 p \end{cases} \tag{2.3}$$

At higher proton and photon energies, other processes including higher resonances and multi-pion production may contribute substantially to the total pion production.

Pion production is relevant for the propagation of charged Cosmic Rays (CRs), the production of neutrinos and gamma rays and for the development of hadronic air showers in the atmosphere. Charged pions decay as

$$\pi^\pm \rightarrow \mu^\pm \nu_\mu \rightarrow e^\pm \nu_e \nu_\mu \nu_\mu \,, \tag{2.4}$$

where the difference between particle and anti-particles has been neglected. This results in neutrino production with the flavor ratio $\nu_e : \nu_\mu : \nu_\tau = 1 : 2 : 0$. Neutral pions decay into photons via

$$\pi^0 \rightarrow 2\gamma \,, \tag{2.5}$$

resulting in the production of high energy photons. The described pion production and decay are believed to take place in many environments in Astroparticle Physics. Hence, correlations between the fluxes of different particle types are expected.

At very high particle energies, the production of heavier particles, mostly kaons, dominates over pion production in pp or $p\gamma$ interactions. Consequently, at these energies their decay is the dominant process for neutrino production.

2.1.2 The Cherenkov effect

The characteristic radiation of charged particles moving through a medium with a refraction index n faster than the speed of light in that medium, c/n, is called Cherenkov radiation. The charged particle polarizes atoms of the medium temporarily. This changing polarization results in the emission of electromagnetic radiation. If the particle moves slower than the speed of light, the dipoles are symmetric to the particle track such that no resulting radiation is emitted. If the particle moves faster than c/n, the symmetry is broken and Cherenkov radiation is emitted [Gru93]. The Cherenkov photons are emitted under a characteristic angle to the particle's track. This angle is called the Cherenkov angle Θ_c, which is given by

$$\cos\Theta_c = \frac{1}{n\beta} \,, \tag{2.6}$$

where $\beta = v/c$ is the particles' velocity, v, divided by the speed of light, c. Here, the momentum transfer of the particle with momentum p to the Cherenkov photons with wave number k has not been considered since it is a small correction of the

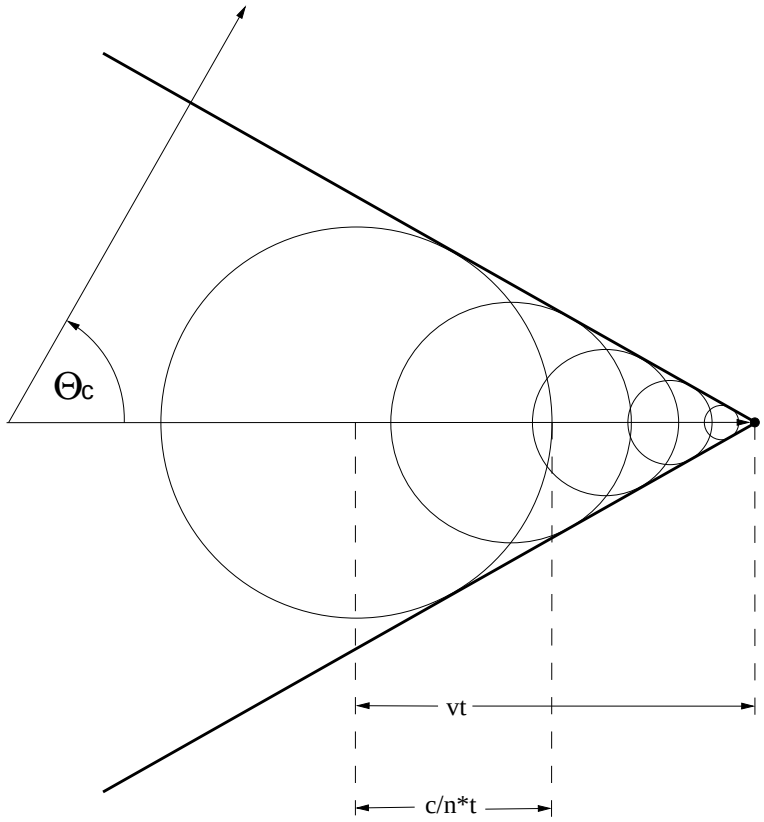

Figure 2.1: A charged particle moves through a medium faster than the speed of light in that medium. The wavefronts describing the propagation of light emitted due to changing polarization of the medium interfere constructively and form the Cherenkov cone. The light is emitted with the angle Θ_C with respect to the particle track [Jac62, Dre05].

order $\hbar k/p$ [Gru93]. With $n_{ice} \approx 1.33$ and $\beta \approx 1$, the Cherenkov angle in ice is given by $\Theta_c \approx 41.2°$. In air, $n = 1.00029$ results in $\Theta_c = 1.3°$ [Wee03b]. Since the charged particle moves faster than the photons in the medium, the Cherenkov photons propagate on the surface of a cone, the so-called Cherenkov cone as it is indicated in Fig. 2.1. Thus, a measurement of the arrival times of Cherenkov photons allows for the reconstruction of the particle track.

The minimum energy of a particle to emit Cherenkov light may be inferred from the condition that the particle is faster than c/n. For a muon in ice, this energy is given by

$$E_\mu^{min} = m_\mu \gamma c^2 \approx 160 \text{ MeV} \quad \text{with } m_\mu = 105.65\,\text{MeV}\,. \tag{2.7}$$

In air, the energy threshold of a muon to emit Cherenkov light is given by $E_\mu^{min} = 4$ GeV [Wee03b]. For electrons, the threshold is at $E_e^{min} = 21$ MeV [Wee03b].

The Cherenkov effect is important for the detection of particles in high energy Astroparticle Physics, since the emitted light may be detected in transparent media at a certain distance from the particle track. In this way, it allows detectors to cover large volumes.

2.2 The Cosmic Ray spectrum

The central observation in Astroparticle Physics concerns the flux of high energy charged particles, the Cosmic Rays (CRs). The CR flux turns out to be isotropic and reaches particle energies of at least up to 10^{20} eV. In total, 98% of the measured particles with $E > 1$ GeV are nuclei while about 2% are electrons. The largest contribution to the flux of nuclei is given by protons (87%) and helium (12%) [Lon92]. Due to the steeply falling energy spectrum, these numbers are dominated by the low energy component of CRs. At higher energies, the contribution of heavier nuclei increases. For example, at $E \approx 100$ TeV, the CRs consist of about $63 \pm 5\%$ light nuclei (protons and He nuclei) and $37 \pm 5\%$ heavy nuclei (C - Fe) [Wie98].

A direct measurement of the CR flux at sea level is not possible, since protons and heavier nuclei do not reach the Earth: traversing the atmosphere implies traversing more than ten interaction lengths for these particles [Sta04]. The influence of the atmosphere can be reduced to a minimum by the use of CR detectors on balloons reaching altitudes of up to 40 km. A generic CR detector on a balloon experiment is given by a magnetic spectrometer. Such a detector is shown schematically in Fig. 2.2. It consists of two layers measuring the time and position simultaneously at the top and the bottom of the detector, a powerful magnet in the middle and a layer for charge measurement. The bending by the magnetic field and the travel time from the top to the bottom layer allows to determine its energy and mass [Sta04].

Since the CR spectrum turns out to be steeply falling with energy, the limited size of detectors on balloon and satellite experiments restricts this class of experiments to energies up to about $5 \cdot 10^{14}$ eV. At higher energies, the atmosphere may be used as detector medium. The primary CR particle interacts with a nucleus in the upper atmosphere. In this interaction, several particles are produced. Among these, there are mesons, mostly pions, and electrons. The secondary particles interact again, and an *air shower* is formed. An electromagnetic cascade develops by subsequent energy losses of electrons via bremsstrahlung and pair production by the generated high energy photons. In addition to the electromagnetic cascade, a hadronic shower develops. The neutral pions in the hadronic shower decay into gamma rays, which again start electromagnetic cascades. This results in a characteristic structure of air showers initiated by a hadronic interaction of a nucleon or a heavier nucleus. The number of particles increases with the depth in the atmosphere until the energy of the secondaries drops below the threshold for generating further particles. After the air shower reaches its maximum, the number of particles falls due to absorption

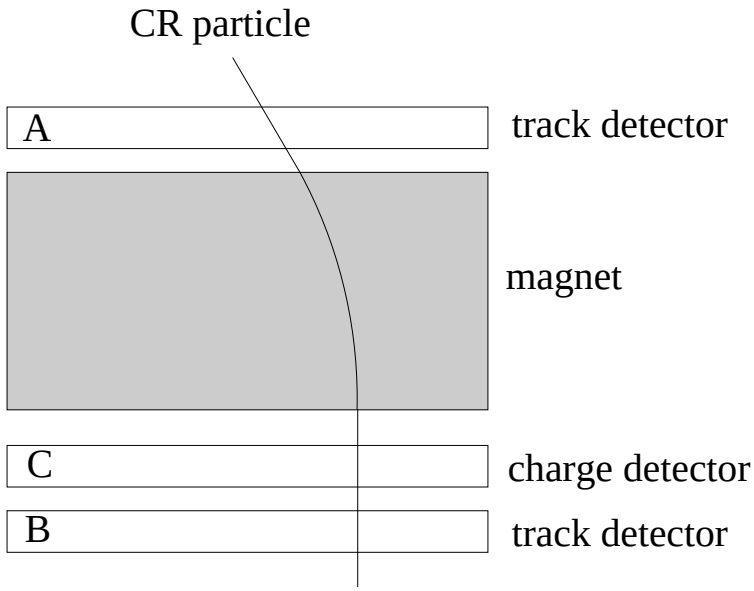

Figure 2.2: Magnetic spectrometer as a generic CR detector on a balloon experiment [Sta04]. Two layers of track detectors (A and B) determine position and time of the CR particle passing through the detector. A different detector C measures the particle charge. With the measured charge, the particle's energy may be determined from the bending of the particle by the magnet.

processes. The depth of the shower maximum in the atmosphere increases with the energy of the primary. Depending on the energy of the CR primary, the air shower reaches the surface of the Earth or all particles get absorbed before. A sketch of an CR induced air shower is given in Fig. 2.3.

If the energy of the air shower is sufficiently high, particles reach the Earth simultaneously within a large radius around the shower center. Thus, the air shower can be measured by particle detectors spread over a large area on the ground, yielding an image of the shower at the ground. A low energy threshold can be achieved by constructing the detector array at high altitudes, while for high energies low altitudes are preferred to ensure that the detector is located below the shower maximum. Alternatively, the shower development can be traced by telescopes. These telescopes detect the Cherenkov light emitted by charged particles passing through the atmosphere or the fluorescence light emitted by atmospheric nitrogen atoms ionized by the charged particles. Since the interactions are governed by quantum mechanical probabilities, there are large fluctuations in the shower characteristics. Hence, the reconstruction of individual shower parameters becomes inaccurate while with sufficiently high statistics, the spectrum can be measured accurately.

The area to be covered by detectors increases with the particle's energy. The HEGRA experiment [Kon99] covers an area of roughly 0.04 km^2 at an altitude of 2200 m and allows to measure the CR spectrum at energies from $5 \cdot 10^{11}$ eV to

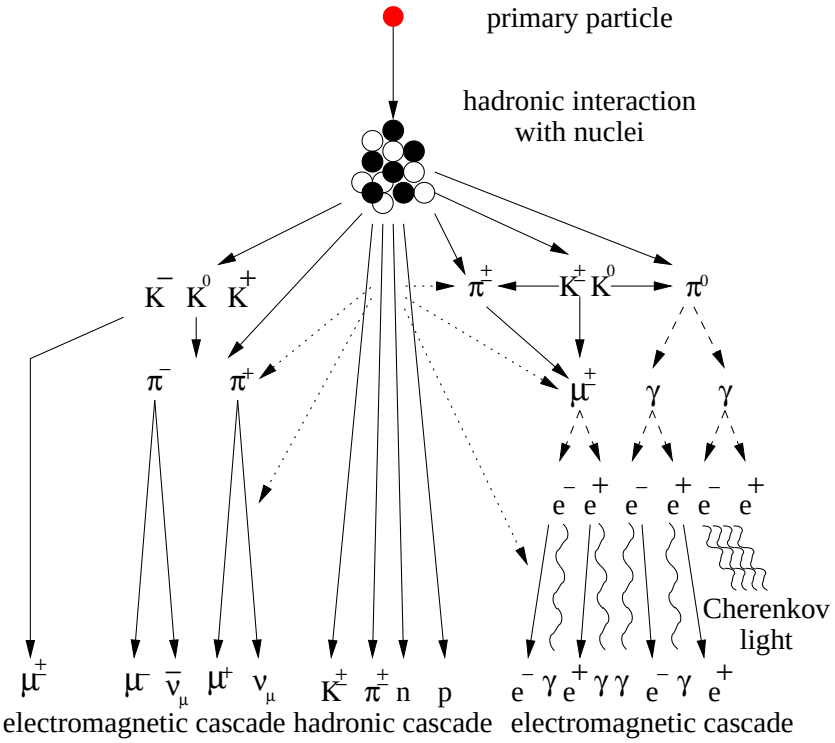

Figure 2.3: Sketch of an CR induced air shower: after a hadronic interaction of the CR primary with a nucleus in the upper atmosphere, an electromagnetic and a hadronic cascade develop [Wag04].

10^{16} eV. At energies between 10^{15} eV and 10^{17} eV, the KASCADE Grande [H$^+$05a] surface array with an area of 0.5 km^2 provides sufficiently high event rates. At higher energies above 10^{18} eV, an area on the scale above tens of km^2 has to be covered to provide sufficient event rates. This has been realized in the AGASA[1] surface array in Japan (100 km^2) [Y$^+$95] and in the HiRes fluorescence telescope in the USA [Cao03]. The Pierre Auger observatory [B$^+$02] currently under construction in Mendoza (Argentina) will cover an area of 3000 km^2 and will make use of both detection techniques. It will collect sufficiently high statistics to measure the CR spectrum above 10^{19} eV in detail. A second observatory on the Northern Hemisphere is planned in Colorado in order to allow for better anisotropy studies.

The observed CR flux as a function of energy is displayed in Fig. 2.4. It follows a broken power law, $\Phi_E \propto E^{-\gamma}$. At energies $E < 10^{15}$ eV, the spectral index is $\gamma \approx 2.67$ [Wie98]. Above this energy, the CR spectrum steepens to a spectral index of $\gamma \approx 3.10$ [Wie98]. The transition point to this steeper spectrum is called the *knee*. At energies above 10^{19} eV, where the so-called *ankle* is observed, the CR spectrum gets flatter again to a value of $\gamma \approx 2.75$ [Wie98].

[1] Akeno Giant Air Shower Array.

Energies of the order of GeV to several hundred TeV usually are called high energies (HE), energies in the range of PeV up to the ankle at 10^{18} eV are called very high energies (VHE). The highest energy range, where CRs have been detected, from 10^{18} to 10^{21} eV is called ultra high energy (UHE).

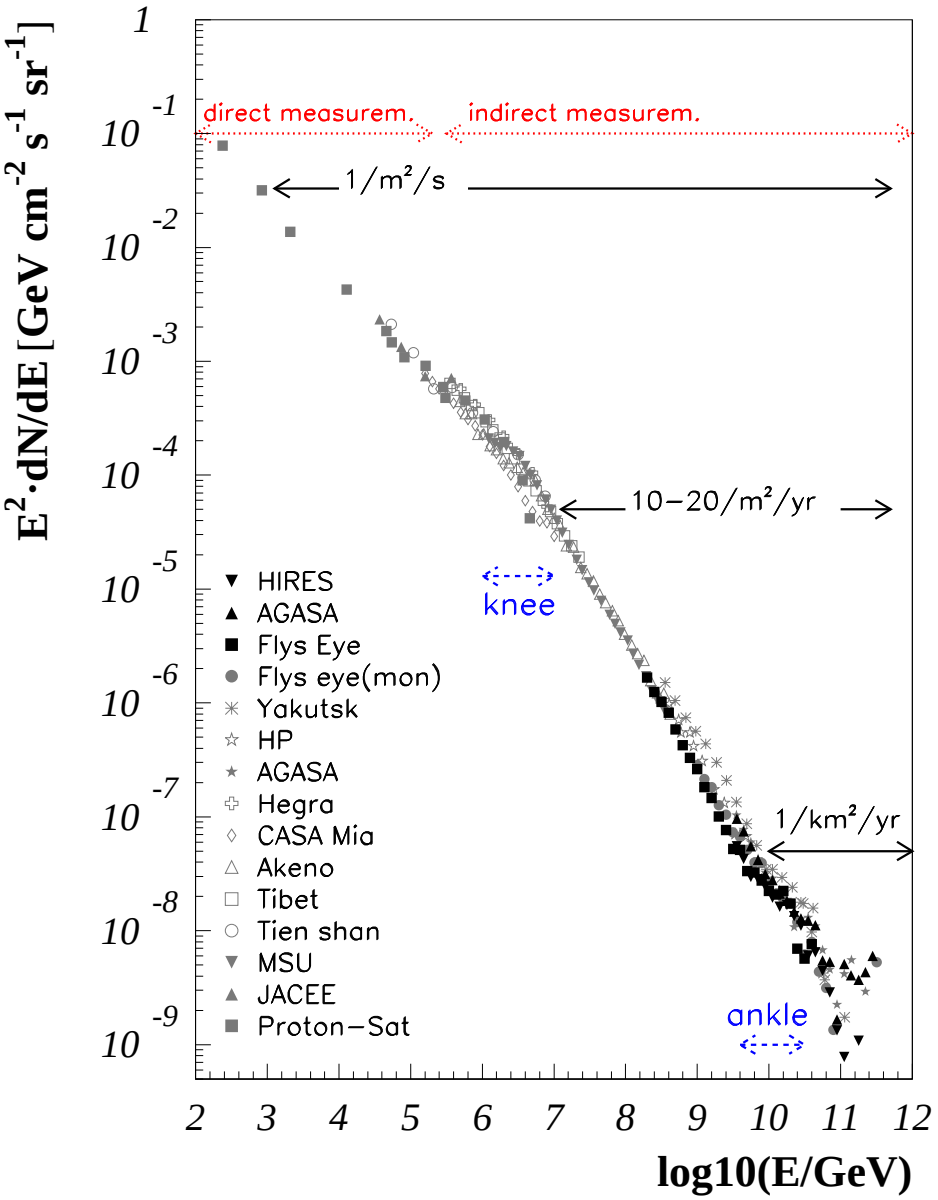

Figure 2.4: The Cosmic Ray Energy spectrum. The major breakpoints, the knee at $\sim 10^{15}$ eV and the ankle at $\sim 10^{19}$ eV, are indicated. The energy ranges for direct and indirect detection methods are marked [BS05].

As the CRs are charged particles, they get deflected in magnetic fields. Thus, the directional information gets lost and no sources of CRs can be identified. As a result, the origin of CRs is not directly observable. For very high energies, the deflection gets weaker, and, depending on the strength of the extragalactic magnetic fields, CR astronomy gets possible. The gyro-radius r_g of a CR particle with an electric charge $Z \cdot e$ is given by [Sta04]

$$r_g = 100 \left(\frac{E_{20}}{Z B_{-9}} \right) \text{ Mpc} , \tag{2.8}$$

where E_{20} is the particle's energy in units of 10^{20} eV and B_{-9} is the magnetic field strength in nG. For uniform magnetic fields of 1 nG, a particle with $E = 10^{20}$ eV emitted by a source at 20 Mpc gets deflected by 10°. Under the more realistic conditions of a random field, the average deflection angle is reduced to 0.35° [Sta04]. As the propagation of UHE CRs is restricted (see below), these particles should originate within this distance and thus point roughly to their sources. However, the value of the extragalactic magnetic fields can only be estimated and a higher value is not excluded. Up to now, no sources of UHE CRs could be identified.

2.2.1 Acceleration processes and candidate sources

The existence of high energy CRs can be explained by the acceleration of low energy particles to high energies or by the decay of heavy particles into the observed CRs. The first class of models is classified as *Bottom-Up*, the second class is labeled *Top-Down*.

The most powerful *Bottom-Up* model is given by the mechanism of Fermi acceleration. With help of a statistical energy gain of particles in a large number of acceleration cycles and with a certain escape probability after each cycle, the observed power law spectrum of CRs can be explained naturally.

The model originally proposed by Fermi [Fer49] considers particles being scattered in magnetized gas clouds moving with random velocities through the interstellar medium, see Fig. 2.5 (a). In the rest frame of the cloud, the energy of the particle remains unchanged since the scattering is collisionless [Pro98]. After a Lorentz transformation into the laboratory frame, this results in a relative energy gain of the particle in average, which is proportional to β^2, where $\beta = v/c$ is the cloud velocity. Since the energy gain is second order in β, this acceleration model is called 2^{nd} order Fermi acceleration.

A more efficient acceleration can be achieved if strong shock waves are present. Like in the original model, the considered particles get scattered in magnetized clouds. As it is indicated in Fig. 2.5, these clouds are situated on both sides of a shock front. The random scattering of the particles makes them cross the shock front several

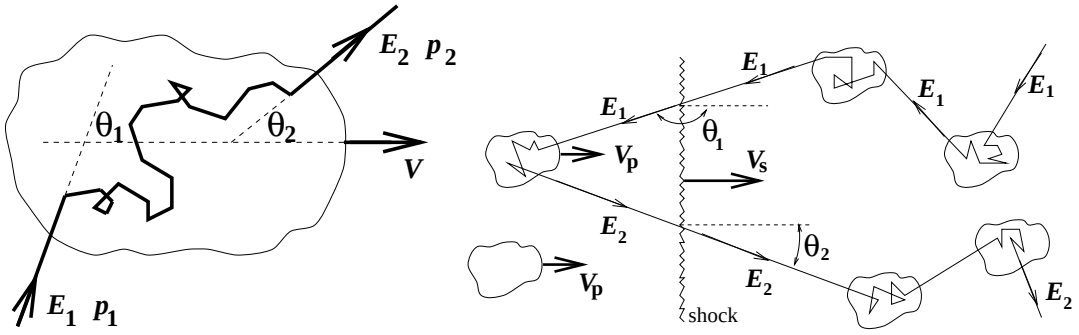

(a) (b)

Figure 2.5: On the left, the mechanism of second order Fermi acceleration is shown schematically. A scheme of the more efficient first order Fermi acceleration is displayed on the right [Pro98].

times. For each crossing of the shock front moving with v_s, the average energy gain of a particle is proportional to $\beta = v_s/c$ [Bel78a, Bel78b, Pro98]. Because it is proportional to β, this more efficient acceleration mechanism is called first order Fermi acceleration or *diffusive shock acceleration*. The energy spectrum of the resulting CRs may be derived by considering the probability for a particle to cross the shock front n times. This results in a power law spectrum with $N(E) \propto E^{-2}$, where $N(E)$ is the number density of particles at an energy E.

The energy which a particle can reach in any *Bottom-Up* model is restricted by the requirement that the magnetic field is high enough to confine the particle in the source region to allow for further acceleration of the particle. This results in

$$E_{max} = \beta \cdot Z \cdot B[\mu G] \cdot R[kpc]\,, \tag{2.9}$$

where Z is the charge of the particle in units of e, B is the magnetic field strength in the source region and R is the size of the acceleration region [Hil84]. Figure 2.6 shows the so-called *Hillas plot* in which the magnetic field strength is displayed versus the size of the acceleration region. Source classes providing sufficient size and magnetic fields for the acceleration of CRs to high energies can be identified.

In our galaxy, supernova remnants (SNRs) are prominent sources for CR acceleration. They can accelerate particles to energies of about 10^{15} eV and they are likely to contribute most of the observed CRs below that energy [BS01]. The origin of the steepening of the CR spectrum above that energy is not yet solved. One possibility is that the wind-SNRs contribute at these energies. Wind-SNRs are formed by the explosion of very heavy stars into their stellar wind. The geometrical structure of SNRs and wind-SNRs is displayed in Fig. 2.7. Wind-SNRs accelerate particles very

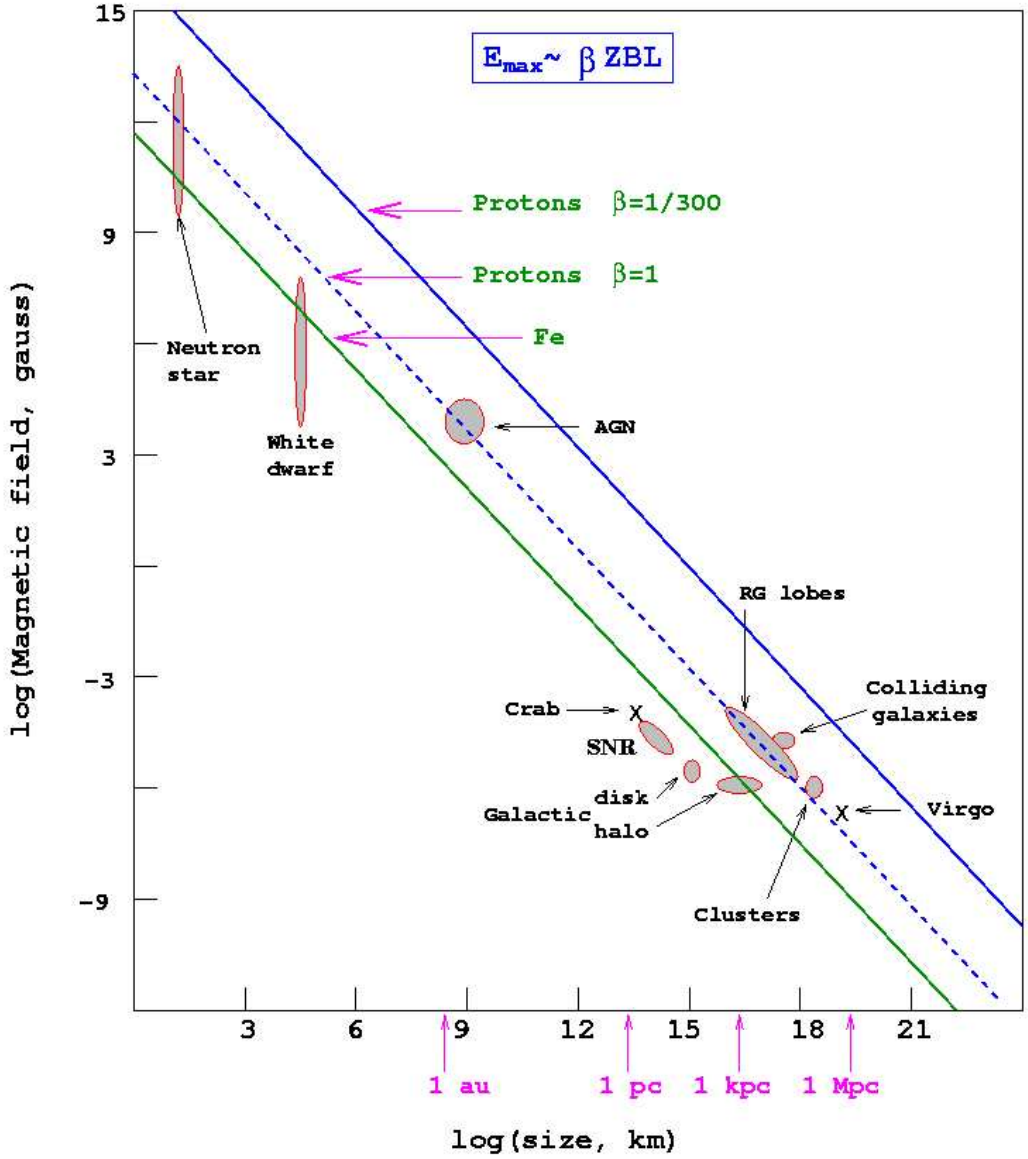

Figure 2.6: Hillas plot: various astrophysical objects are displayed on the magnetic field - source size plane. The maximum energy for stochastic particle acceleration is constant along diagonal lines [Arg00].

efficiently in oblique shocks, where the magnetic field is nearly perpendicular to the shock front normal [Bie93, Bie04, MB]. Another explanation is given by the *leaky box model*. Particles produced in local sources are confined by the average galactic magnetic field to the local galaxy, with a small probability they can escape from the galaxy. The mean time of residence until the particle escapes can be estimated as $\tau_{\mathrm{esc}} = 2 \cdot 10^7$ years [Gai90].

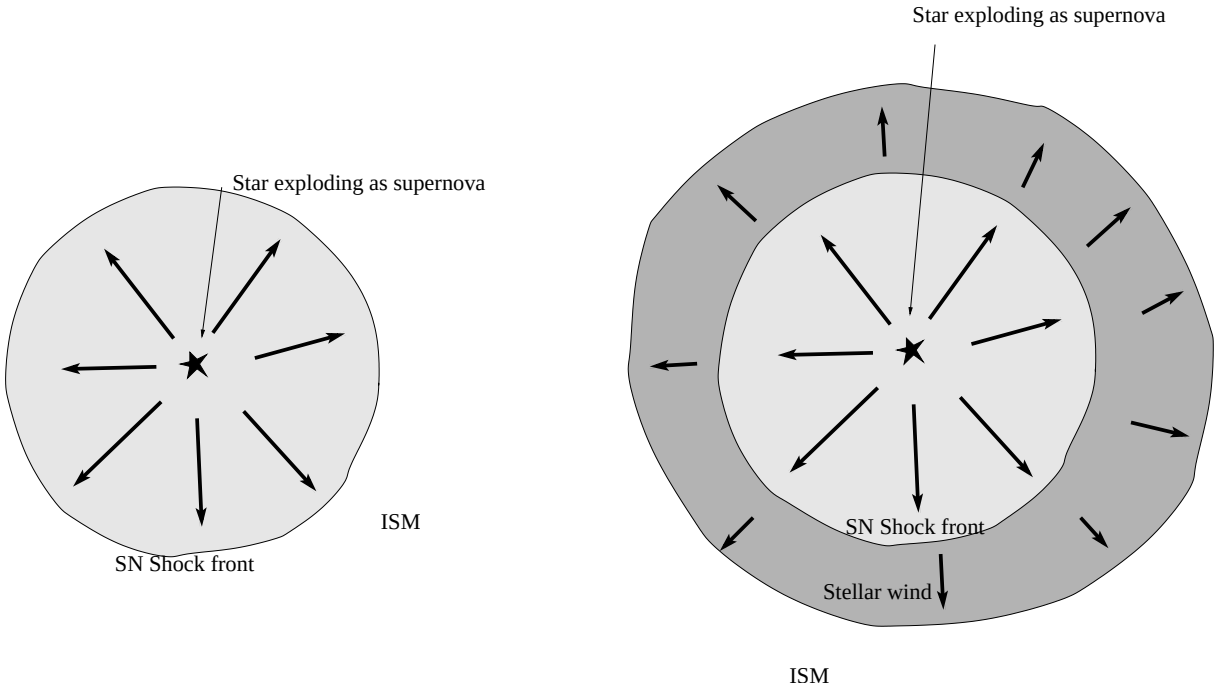

Figure 2.7: Supernova remnants as CR candidate source. On the left: a supernova explodes into the interstellar medium (ISM). On the right: a supernova explodes into the stellar wind of the heavy predecessor star, providing the possibility for more efficient particle acceleration.

Microquasars are a further class of galactic candidate sources of CRs. A microquasar is a jet-disk system with a rotating black hole of a few solar masses or a neutron star in the center. The structure of microquasars is displayed in Fig. 2.8 on the left. Two jets of matter outflow are formed parallel to the rotation axis of the black hole. An accretion disk perpendicular to the jets is fed by matter which is transfered form a companion star. Hence, microquasars are located in binary systems [Mir02]. From a theoretical point of view, it is likely that all X-ray binaries have a jet and thus they are microquasars [Mir01]. Due to the small number of observed microquasars, the expected CR flux from microquasars is not expected to be dominant in the CR spectrum, possibly except from a small energy window between 3 GeV and 10 GeV [HS02].

At the *ankle*, extragalactic sources become dominant over galactic sources. Above $E = 5 \cdot 10^{18}$ eV, CRs are not confined in our galaxy anymore so that galactic objects are unlikely to be the sources. Prominent extragalactic source candidates are Active Galactic Nuclei (AGN) and Gamma Ray Bursts (GRBs). Figure 2.6 shows that the size and the estimated magnetic field strength of AGN are sufficiently high for particle acceleration up to energies of 10^{20} eV. AGN will be discussed in detail in Chapter 3.

Gamma Ray Bursts (GRBs) are transient phenomena emitting a very high amount of γ radiation in a very short time. Under the assumption of isotropic radiation, their luminosity reaches 10^{51} erg/s. Typical burst durations vary between 0.1 s and 1000 s. The distribution of burst durations shows two maxima which are separated by two orders of magnitude. This suggests the classification into long duration GRBs and short duration GRBs. The fireball model [ZM04] recently turned out to describe the phenomenology successfully. According to the fireball picture, GRBs are formed by the collapse of a massive predecessor object or by the merger of two objects. Similar to microquasars and AGN, the collapse is not rotational symmetric and the conservation of angular momentum results in the occurrence of two jets along the rotation axis. In these jets, shock waves form and propagate outwards. In these shocks, Fermi acceleration of charged particles takes place. High energy photons are either produced by leptonic or hadronic mechanisms. These photons leave the source as soon as the shock environment becomes optically thin. In the case of a hadronic mechanism, GRBs are expected to emit neutrinos and charged CRs. The beaming effects reduce the necessary energy supply of the GRB.

A connection of long duration GRBs to supernovae of type Ic is confirmed by observations of GRB030329 and GRB980425 [ZM04]. Recently, observations of the short duration bursts GRB 050509 B, GRB 050709 and GRB 050724 supported the model that short duration GRBs are caused by the merger of a neutron star with a second neutron star or with a black hole [H^+05b, V^+05, G^+05a].

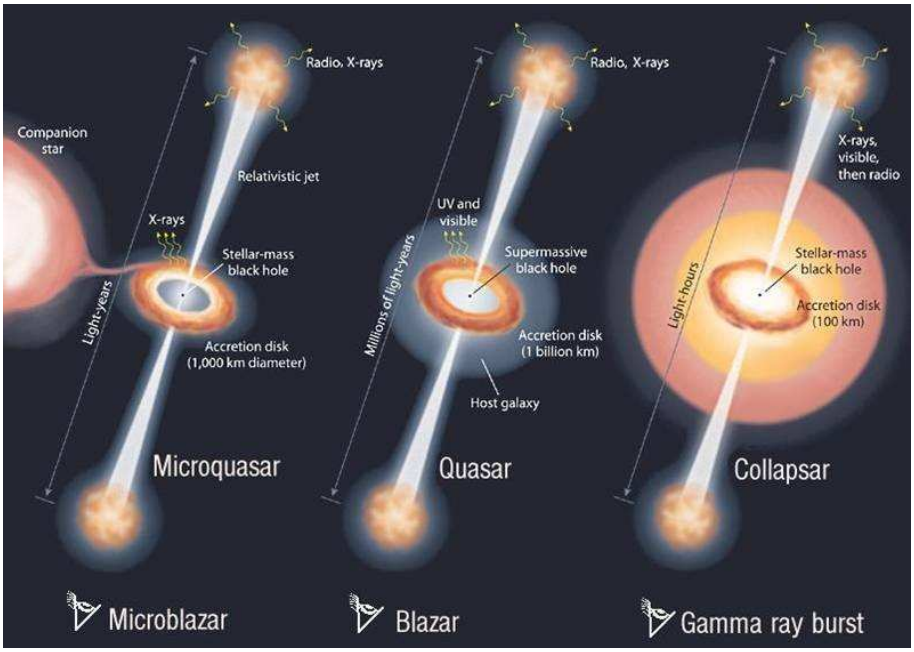

Figure 2.8: Jet-disk systems as CR candidate sources: Microquasar, AGN and GRB [Mir02].

The structure of the discussed CR source candidates can roughly be characterized by two different geometries. While SNRs are approximately spherical symmetric sources, microquasars, AGN and GRBs have a jet-disk structure. These structures are visualized by a sketch of SNRs in Fig. 2.7 and by a schematic comparison of microquasars, AGN and GRBs in Fig. 2.8.

A recent review on *Top-Down* models, including constraints from observations of CRs and γ rays and from the cosmological parameters can be found in [Dre03]. The consideration of Tow-Down models is motivated by the fact that in these models no GZK cut-off is expected (see below). *Top-Down* models explain parts of the CR spectrum like the highest energetic component, e.g., by the decay of a hypothetic heavy particle X with mass $m > 10^{12}$ GeV and lifetime $\tau_X > 10^{10}$ yr [Dre03]. All considered Top-Down models predict a higher production of photons than protons. These photons either propagate to the Earth or they get absorbed. Observations however indicate that the UHE CRs at Earth are dominated by protons [Dre03]. If the UHE photons get absorbed, the expected flux of UHE photons according to these models gets reduced, but in electromagnetic cascades photons are produced in the energy range of 100 GeV to 1 TeV. Thus, Top-Down models are constraint by the observed low fraction of UHE photons and by the EGRET limit on the diffuse gamma ray flux [Dre03]. This excludes Top-Down models to be dominant for energies below $5 \cdot 10^{19}$ eV. Consequently, Top-Down models in general are currently less favored by experimental data than Bottom-Up models.

2.2.2 The GZK cut-off

The propagation of high energy CRs is restricted by the following process: protons with an energy above the threshold for the photoproduction of the Δ resonance interact with ambient photons from the Cosmic Microwave Background (CMB). In the decay of the Δ, a proton or a neutron of lower energy is generated. Since a neutron decays into a proton, the total process is equivalent to an energy loss of the proton. In principle, this effect is present at all energies, but only the CMB provides a sufficiently high photon density for a measurable effect. Hence, the transparency of the universe for protons decreases dramatically at energies above $E_{GZK} = 5 \cdot 10^{19}$ eV. This results in the prediction of a strong suppression of the CR spectrum above this energy by Greisen [Gre66] and Zatsepin and Kuzmin [ZK66], the so-called GZK cut-off. Due to the steeply falling CR spectrum, the expected excess of the CR flux around $5 \cdot 10^{19}$ eV due to GZK energy losses is small in comparison with the background of lower energy CRs.

The mean free path of a particle with an energy above the GZK threshold is below 50 Mpc. The AGASA experiment observed several CR events above that threshold [Y$^+$95]. This indicates a continuation of the CR spectrum above the GZK energy. In contrast, according to data from the HiRes experiment, a cut-off at high energies is more likely [Cao03]. If there is a continuation of the spectrum over the GZK

threshold, as suggested by AGASA, the sources of the UHE protons must be closer than 50 Mpc. The nearby AGN M87, classified as a FR-I radio galaxy (see Chapter 3), is a plausible candidate source for these events. The magnetic field and size are sufficient to accelerate particles to UHE energies and the distance is small enough to avoid a substantial suppression of the UHE flux by the GZK effect. An estimation of the jet power using the jet-disk symbiosis model [FB95, FMB95] shows that a sufficiently high flux to explain measured data is plausible [Tas04]. Also according to the Synchrotron Proton Blazar model (see Chapter 3) high CR emission is expected from that source [PDR03]. However, the extragalactic magnetic fields must be higher than the usually assumed values to allow for the observed arrival directions not pointing directly to M87.

In contrast, no GZK cut-off is expected according to *Top-Down* models, since heavy particles may decay at smaller distances from Earth.

2.3 Gamma ray astronomy

Additionally to the observations of charged particles, high energy photons with energies up to tens of TeV have been observed from astrophysical sources. At energies up to 10 GeV, satellite experiments like EGRET [L$^+$99] on the CRGO observatory provide the sensitivity to detect more than 200 astronomical sources of high energy photons. The largest fraction of these sources have not yet identified with sources detected at other energies. A strong accumulation of these unidentified sources at low galactic latitudes shows a galactic origin for most of them. In addition, more than 60 AGN were identified[2] [H$^+$99]. In addition to point sources, EGRET has detected diffuse γ rays [CH05]. A band of strong diffuse emission was found along the galactic plane. The origin of this diffuse emission in our galaxy is believed to be the result of the interaction of CRs with interstellar matter and photons. The observed excess over the expected spectrum can be explained by local differences in the CR spectrum [SMR04] or by an additional component of different origin. In future, the GLAST[3] experiment will provide a higher sensitivity and it will be sensitive at energies up to more than 100 GeV [GM99].

At higher energies, the effective area of satellite experiments becomes too small and other techniques have to be used. Cherenkov telescopes like HEGRA [Kon99] and Whipple [Caw90] allow for a detection of TeV photons by the Cherenkov light of secondary particles in the electromagnetic cascade initialized by the photon. The threshold of these telescopes is typically at some 100 GeV. Second generation telescopes like H.E.S.S. [Ste00], MAGIC [PM99] and VERITAS [W$^+$02] reach thresholds at 100 GeV or below. They aim for an overlap in the energy band with satellite experiments. The photon induced showers in Cherenkov telescopes can be separated

[2] The exact number depends on the confidence level required for the identification.
[3] Gamma-ray Large-Area Space Telescope

from hadronic showers by a different shower profile. Thus, the 10^3 times more abundant hadronic showers can be suppressed [Wee03b].

Two different models may explain the production of high energy gamma rays. According to the *leptonic model*, only electrons are accelerated to high energies. These high energy electrons scatter low energy photons up to high energy via the inverse Compton effect. The *hadronic model* assumes that protons and electrons are accelerated to high energies. The protons may interact with each other or with photons resulting in pion production. Neutral pions decay into high energy photons. Current gamma ray observations do not allow for a strict statement on the dominant production mechanism of high energy photons for the various source classes.

Gamma rays have been detected from galactic and extragalactic sources. In our galaxy, supernova remnants have been found to emit gamma rays. Due to its steady strong emission, the Crab Nebula, which is the remnant of a supernova that erupted in 1054, is a unique source. For this reason, it became the standard candle of TeV astronomy. Observations of TeV photons from the supernova remnant RX J1713.7-3946 with the H.E.S.S. telescopes in combination with observations at lower energies favor hadronic models while a leptonic origin of the observations cannot be ruled out [A$^+$05e]. Many detected GeV sources in the galactic plane remain unidentified with any source detected at other energies until now. While it is possible, that some of them are microquasars [R$^+$04a], others may belong to different source classes. Extragalactic sources of gamma rays are AGN and GRBs, which have been listed above as candidate sources of charged CRs.

Similar to the GZK effect for charged CRs, the propagation of photos through the universe is restricted absorption on photons. The corresponding interaction is given by pair production with ambient photons,

$$\gamma\gamma_{bg} \rightarrow e^+e^- \,, \tag{2.10}$$

with a threshold at the center of mass energy of $2 \cdot 511$ keV. The diffuse photon flux as a function of energy is shown in Fig. 2.9. For photon energies above 10^{15} eV, the universe becomes opaque for photons because of pair production on photons of the Cosmic Microwave Background (CMB). However, also at higher energies of the ambient photons, the photon density is not negligible. The high background of infrared (IR) photons limits the propagation of TeV photons to our cosmological neighborhood. The maximum energy for gamma ray astronomy as a function of the redshift of the sources is shown in Fig. 2.10. The most distant source of TeV photons detected with the first generation telescopes is H1426+428 found at a redshift of $z = 0.129$ [H$^+$02a].

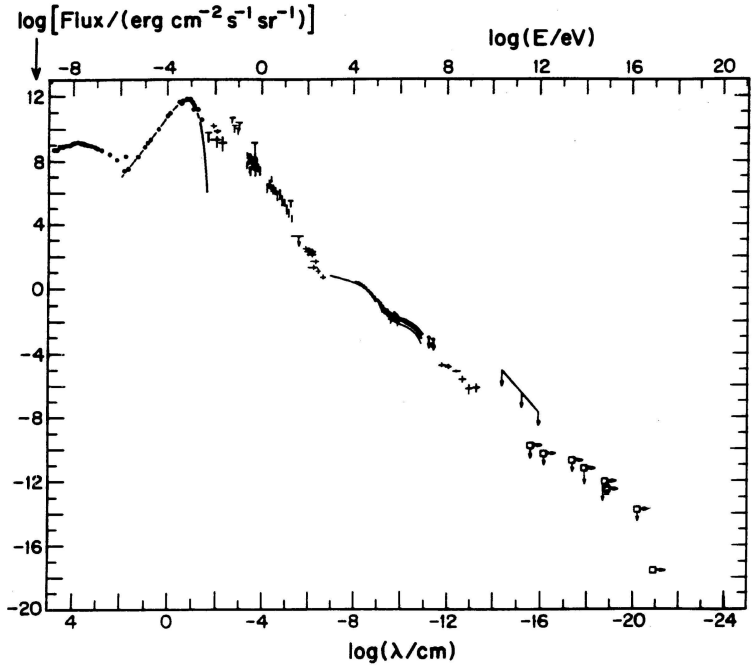

Figure 2.9: The diffuse photon flux as a function of the wavelength. The largest flux is given by the CMB [RT90].

2.4 High-energy neutrino astronomy

The concept of neutrino astronomy is motivated by the fact that neutrinos are almost ideal astronomical messenger particles. In contrast to photons and protons, neutrinos hardly suffer any absorption or deflection while propagating through space. Their lack of electric charge decouples neutrinos from magnetic fields and their cross sections for interaction with matter are small.

Theoretical models of the production of CRs and gamma rays predict correlated production of neutrinos and thus the presence of a high energy neutrino flux. The neutrinos are assumed to be the result of the decay of mesons, mostly pions and kaons, produced in pp or $p\gamma$ interactions in the source, see above. This production scenario requires the acceleration of protons to high energies. Furthermore, the production of charged pions is correlated with the production of neutral pions, resulting in gamma rays. The Clebsch-Gordon coefficients of the decay of the intermediately produced resonances determine the fraction of neutral and charged pions. Thus, neutrino astronomy has the potential to solve both the question of the origin of CRs and the question of the production mechanism of gamma rays. The correlated production of CRs, γs and νs, the propagation of these particles to the Earth and their detection is sketched schematically in Fig 2.11.

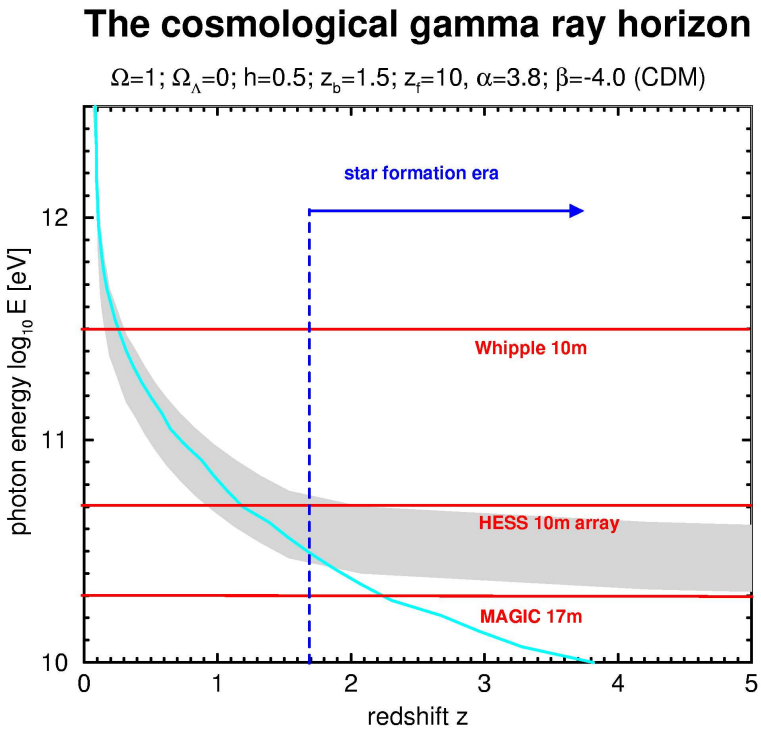

Figure 2.10: The maximum photon energy for gamma ray astronomy as a function of redshift. The energy thresholds of several TeV telescopes are indicated with horizontal lines [Man99].

The most promising candidates for neutrino sources are given by supernova remnants (see Fig. 2.7) and by jet-disk systems around massive compact objects (see Fig. 2.8). The neutrino production by pion decay in these sources results in the flavor ratio $\nu_e : \nu_\mu : \nu_\tau = 1 : 2 : 0$ in the source region. Due to neutrino oscillations, this flavor ratio changes to $1 : 1 : 1$ to be observed at Earth, since the distance to the closest candidate sources is larger than the oscillation lengths [Sta04].

In addition to these extraterrestrial neutrino signals, there are neutrinos produced by CR interactions in the atmosphere of the Earth. These neutrinos are called atmospheric neutrinos and they form an unavoidable experimental background for the detection of extraterrestrial neutrinos. The primary CR particles interact with nuclei in the upper atmosphere and generate pions and kaons. The subsequent decay of these particles results in the production of atmospheric neutrinos. However, neutrinos are produced only if the generated pions and kaons do not interact before their possible decay. Since the decay length of these particles increases with energy, high energy particles are more likely to interact. This results in a steepening of

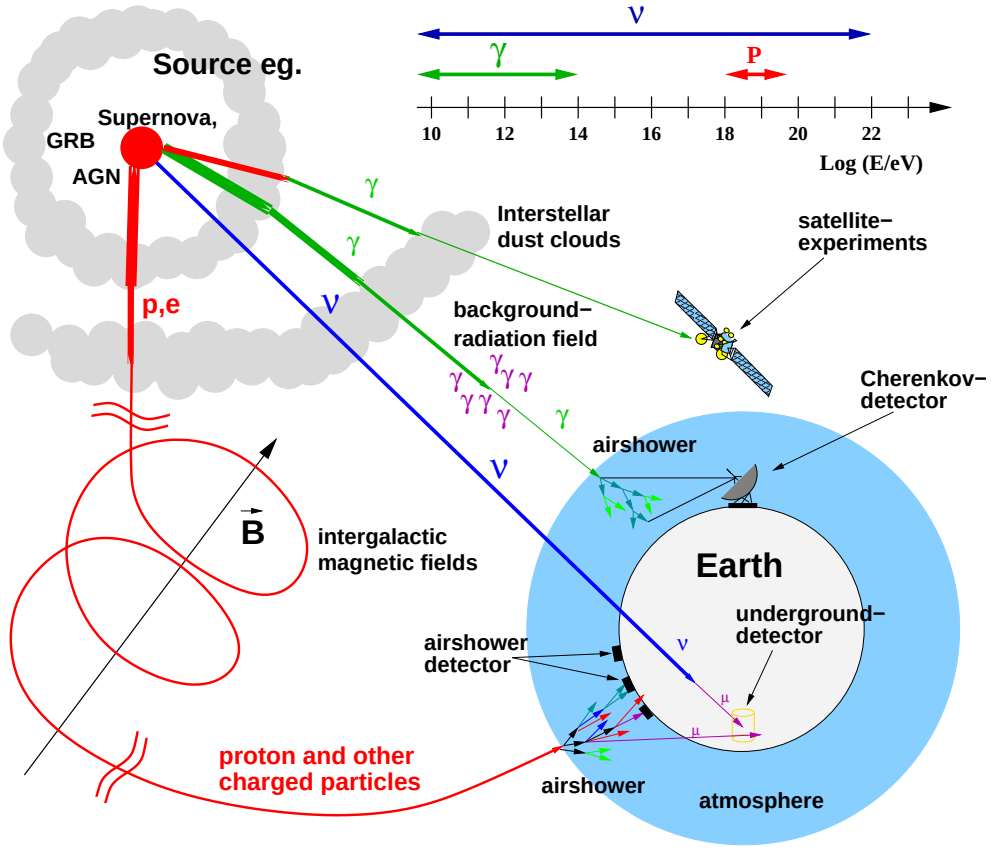

Figure 2.11: Survey of astronomical messenger physics. Only neutrinos can traverse through dust clouds and are not affected by magnetic fields [Wag04].

the spectrum of the atmospheric neutrinos with respect to the charged CRs [Sta04]. The spectral index of the atmospheric neutrino spectrum, $\gamma_{\nu_{atm}}$, is approximately given by $\gamma_{\nu_{atm}} = \gamma_{CR} + 1$, if the CR spectrum follows a power law with spectral index γ_{CR}. The increasing density of the atmosphere when approaching the Earth causes a zenith dependence of atmospheric neutrino flux. In horizontal air showers, the secondary mesons travel through a thinner atmosphere than in vertical showers. Thus, mesons in horizontal air showers are less likely to interact. Consequently, the decay probability and the neutrino production are higher in vertical showers. The atmospheric neutrinos which originate in the decay of pions or kaons will be called *conventional* atmospheric neutrinos throughout this thesis.

In addition to kaons and pions, charmed hadrons contribute to the atmospheric neutrino spectrum. Referring to the very small decay time of charmed hadrons, the neutrinos produced by their decay are called *prompt* neutrinos. Since the probability of charmed hadrons to interact before their decay is very small, the prompt atmospheric neutrino spectrum follows the CR primary spectrum. Above a certain energy it will dominate over the steeper conventional atmospheric neutrino

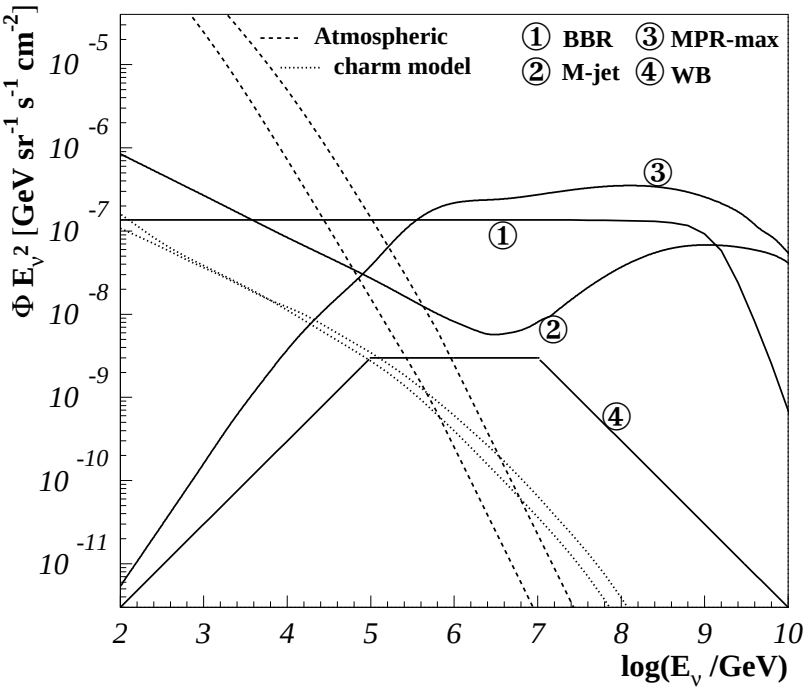

Figure 2.12: Predictions of diffuse spectra of high energy muon neutrinos: the conventional atmospheric neutrino spectrum [VZ80] is indicated by dashed lines. The upper line is the calculated horizontal flux, the lower line corresponds to the vertical flux. The prompt atmospheric neutrino spectrum according to [MRS03] is indicated by dotted lines. Predictions of the diffuse flux from various AGN types [MPR01, Man95, BBR05] are represented by the solid lines 1-3. The predicted diffuse neutrino spectrum from GRBs [WB97] is given by the solid line 4.

spectrum [Cos01]. Due to uncertainties in the charm inclusive cross sections, the predictions on the flux of prompt atmospheric neutrinos are still uncertain. A detection of prompt atmospheric neutrinos would allow to measure the inclusive cross section for charm production and thus it would be relevant for particle physics.

The flux of conventional atmospheric neutrinos above 1 TeV has been calculated in [VZ80], for lower energies the flux is calculated in [H$^+$95]. A prediction of the prompt atmospheric neutrino spectrum is given by [MRS03]. The flux of extraterrestrial neutrinos from various AGN classes has been predicted in [MPR01, Man95, BBR05]. The diffuse spectrum of neutrinos from GRBs has been calculated in [WB97]. These spectra are plotted in Fig. 2.12. According to all these models, the conventional atmospheric neutrino spectrum is predicted to be dominant for energies below 100 TeV.

In the Fréjus experiment, it was proven that the neutrino spectrum up to an energy of 2 TeV is dominated by conventional atmospheric neutrinos [DR$^+$95,RD$^+$96]. With the AMANDA experiment, this can be shown also for higher energies, see Chapter 4.

Another type of background events is caused by the large flux of atmospheric muons produced in CR induced air showers. The flux of atmospheric muons exceeds the neutrino induced muon flux by orders of magnitude. Since the neutrino detection is done by secondary leptons, the background of atmospheric muons has to be reduced to allow for neutrino astronomy. A sufficient background reduction can be achieved by neutrino telescopes situated deep underground. Only events from directions, from which the atmospheric muon flux is shielded by the Earth are considered as neutrino induced events.

For the detection of extraterrestrial neutrinos, the background of atmospheric neutrinos and from misreconstructed atmospheric muons can be reduced by a good angular resolution of the neutrino telescope. Additionally, the signal to background ratio is predicted to increase with energy, since Fermi acceleration predicts a spectral index of 2 which is flat compared with the steep conventional atmospheric neutrino spectrum.

A further challenge for neutrino astronomy is the fact that the cross sections of neutrinos for interactions with nuclei are very small. For a neutrino with energy between 10 GeV and 10^{12} GeV, the cross section for a charged current interaction and for a neutral current interaction with a nucleus are only in the range of 10^{-38} cm^2 and 10^{-30} cm^2 [Gan98]. As indicated in Fig. 2.13, the cross section increases with energy. Below 1 TeV, the increase is linear in E, above 10 TeV, it is proportional to $E^{0.36}$ [Gan98].

The very small cross sections for any interaction at the Earth require large instrumented volumes to provide sufficiently high event rates to allow for neutrino astronomy. As a consequence, no extraterrestrial sources of neutrinos in the energy interval of GeV to PeV could be identified up to now. Currently, the most sensitive high energy neutrino detector is the AMANDA[4] neutrino telescope [AMA], located at the geographic South Pole. The application of analysis techniques which increase the sensitivity could be the only way to allow for a detection of extraterrestrial neutrinos with currently operating neutrino telescopes. Examples for these techniques are given by the analysis of the cumulative signal of several sources, so-called source stacking, and by the selection of active periods of variable sources. This thesis is focused on the development of a source stacking analysis of AGN and its application to data collected by AMANDA.

[4] Antarctic Muon And Neutrino Detector Array

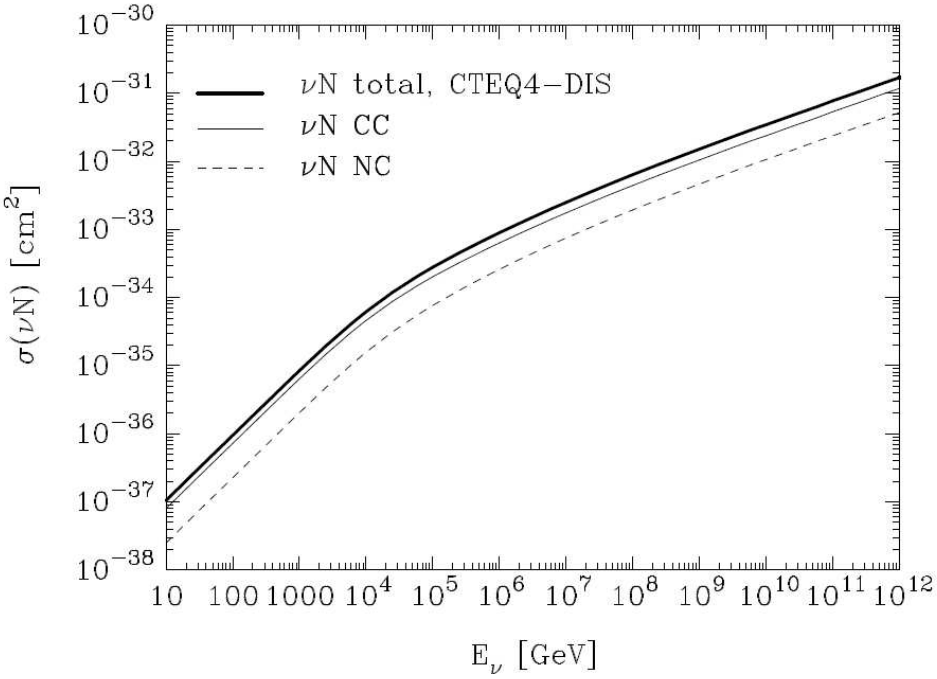

Figure 2.13: Energy dependence of the cross sections for the charged current (CC) reaction $\nu + N \rightarrow l + X$ (where l is the lepton of the same flavor as the neutrino), the neutral current (NC) reaction $\nu + N \rightarrow \nu + X$ and the sum of both cross sections [Gan98]. The CC and NC anti-neutrino nucleon cross sections are smaller by a factor of about 2 at low energies ($E \approx 10$ GeV). At large neutrino energies, $E > 10^6$ GeV, the cross sections are approximately equal.

3

Definition of AGN classes as candidates for high energy neutrino point sources

Active Galactic Nuclei (AGN) are the most luminous permanent objects in the Universe. An active galaxy is an object where a supermassive black hole of $10^6 - 10^{10} M_\odot$ [K$^+$05] in the center of a galaxy is accreting matter at a high rate. The accretion rate is believed to be the result of a recent galaxy merger. In AGN, a part of the gravitational energy of the accreted matter is converted into γ radiation. AGN are candidates for the emission of charged CRs and neutrinos. In this chapter, the production of high energy neutrinos is discussed in detail in order to compose samples of AGN classes.

The selection of samples of AGN classes with respect to their possible neutrino emission is a central contribution of this thesis. The theoretical and phenomenological basis of this selection is presented in Sec. 3.1 with the introduction of an AGN classification based on a geometrically axisymmetric model [UP95] and in Sec. 3.2 with a review of neutrino production models. In Sec. 3.3, catalogs of different types of AGN are selected. These catalogs are ordered with respect to their photon flux in Sec. 3.4, which is assumed to be proportional to the neutrino flux.

The definition of the samples of generic AGN is done in order to get suitable samples for source stacking. Source stacking is a technique to improve the sensitivity of telescopes to generic sources by the evaluation of the cumulative signal of several sources. The application of source stacking in neutrino astronomy is motivated by the limited sensitivity of currently operating neutrino telescopes. Source stacking analyses have been applied in optical astronomy and in gamma astronomy, e.g., in [CHB04, CTR05, MWMF96]. An improvement in sensitivity can only be achieved by source stacking, if there are several sources contributing similar neutrino fluxes. In Sec. 3.5, this condition on the source flux distribution is analyzed quantitatively.

3.1 AGN classification

Historically, a large variety of AGN have been named due to their appearance from an Earth-based telescope. Here, examples are Seyfert galaxies, radio galaxies and quasars.

In contrast to this observational classification, most of the differences among the various AGN types can be explained with a geometrically axisymmetric model, in which different appearances of AGN are the result of different inclination angles of the observers line of sight to the AGN rotation axis [UP95]. The definition of this inclination angle α is visualized in Fig. 3.1. A pictorial scheme of an AGN showing the basic ingredients of the axisymmetric model is given in Fig. 3.2. The AGN consists of a rotating supermassive black hole, two jets along the rotation axis with matter outflowing from the AGN along the rotation axis and, perpendicular to the rotation axis, an accretion disk of matter spiraling into the black hole. Further away from the black hole there is a dust torus. Aside from the effect of viewing this geometry from different inclination angles, there are intrinsically different types of AGN.

Typically, AGN spectra are composed of a thermal part, the so-called blue bump with the maximum at optical-UV frequencies, and a non-thermal part extending over up to 20 orders of magnitude in frequency. Generic photon spectra for AGN including the thermal and the non-thermal component are presented in Fig. 3.3. Within the thermal spectrum, some emission lines are found, which are classified according to their width as broad lines and as narrow lines. It is assumed that the broad lines originate in fast moving dust clouds ($v \approx 1000$ km/s-5000 km/s) near the accretion disk. According to this picture, the narrow lines originate in slowly moving dust clouds ($v \approx 500$ km/s) outside the torus [CO96]. Depending on α, the broad line emission from the clouds at the center may or may not be hidden by the torus. This model is confirmed by the observation of broad lines in the scattered light of AGN [AM85], which show only narrow lines in direct light. The blue bump is interpreted as thermal radiation of the warm inner accretion disk. The low energy component of the non-thermal spectrum in the radio to soft X-ray regime is assumed to be due to synchrotron radiation of electrons gyrating in a magnetic field. The origin of the higher energy component can be explained by hadronic or leptonic models, see Sec. 3.2. The non-thermal γ emission from AGN is known to be highly variable on a wide range of time scales from less than one hour to months [B$^+$05].

The luminosity of the disk and the jets is correlated within the same general AGN class. This motivates the framework of jet-disk symbiosis, where jet and disk are considered as symbiotic features [FB95, FMB95]. The luminosity of the jet and the disk are both fractions of the total energy available, which is given by the mass accretion rate $Q_{accr} = \dot{M}_{disk} \cdot c^2$. The disk luminosity, which is dominated by the blue bump, is parameterized by $L_{disk} = q_l \cdot Q_{accr}$. The total power in the jets is given by $Q_{jet} = q_j \cdot Q_{accr}$. In this way, the dimensionless parameters q_l and q_j parameterize

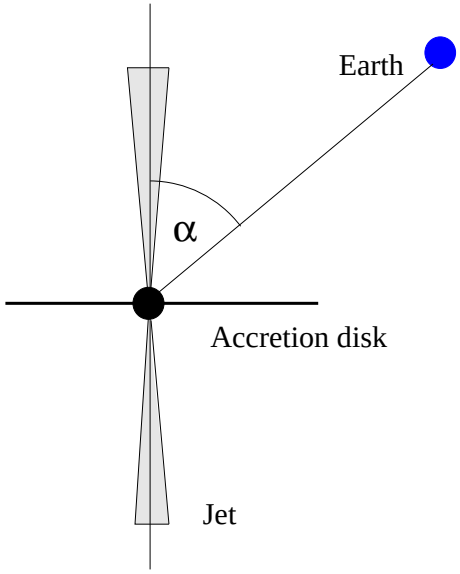

Figure 3.1: The inclination angle of an AGN is defined as the angle α between the line of sight of the observer and the AGN symmetry axis.

the relative weight of disk and jets in the energy balance of the AGN. The observed correlations between q_l and q_j justify the concept that AGN are coupled jet-disk systems [FMB95].

3.1.1 Intrinsically different AGN types - Radio loudness, luminosity and jet size

The radio emission of AGN is assumed to originate mostly in relativistic jets where it is caused by synchrotron radiation of electrons gyrating along the jet. AGN are called radio-loud if the ratio of the radio flux at 5 GHz to the optical flux is larger than 10 [UP95]. In contrast, AGN with a smaller value of this ratio are classified as radio-weak[1]. This classification is motivated by the bimodal distribution of the radio-to-optical ratio. For typical radio-loud AGN, it is several orders of magnitude larger than for typical radio-weak AGN. The different strength of the radio emission of radio-weak and radio-loud AGN is indicated by the solid and the dashed line in the AGN photon spectrum (Fig. 3.3). According to this classification, 10% of the observed AGN are radio-loud, while 90% are radio-weak. Radio-loud AGN are located in elliptical galaxies, radio-weak ones mostly in spiral galaxies [OUS02], but sometimes also in ellipticals.

[1] The term "radio-quiet AGN", which is sometimes also used, is misleading as even radio-weak AGN might have stronger radio emission than galaxies without activity. For this reason, the term "radio-weak" is used in this thesis.

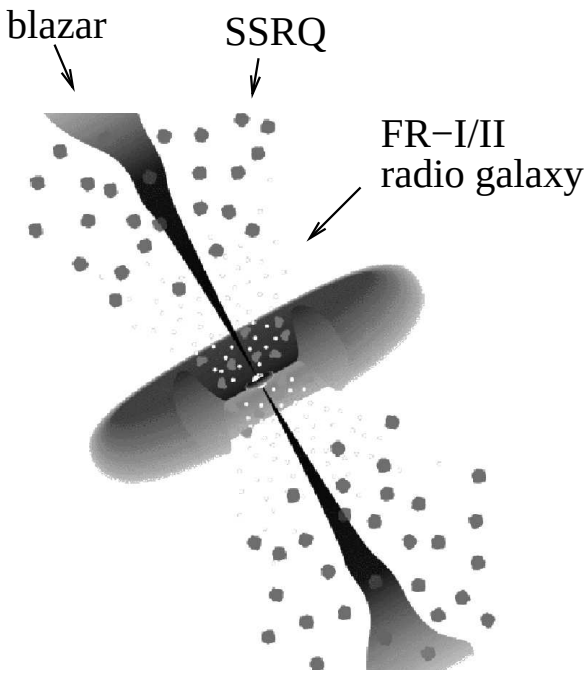

Figure 3.2: Scheme of an AGN with a black hole in the center and an accretion disk perpendicular to the direction of two jets along its rotation axis. The arrows show the directions of the line of sight from the observer to the AGN, which result in the appearance of the AGN as a blazar, a Steep Spectrum Radio Quasar (SSRQ) or a radio galaxy. The gray dots around the jets indicates slowly moving dust clouds, in which the narrow line emission presumably takes place. The smaller dots within the torus symbolize faster moving dust clouds close to the center, where broad line emission takes place. Image adapted from [UP95].

Observations and jet models [FB95] show a flat radio spectrum for the inner part of the jet, i.e., for the radio core. The radio spectrum is called flat, if the flux density F as a function of the frequency ν is described by a power law $F \propto \nu^{\alpha}$ with a spectral index[2] of $\alpha > -0.5$. In contrast, radio lobes and hot spots located at the outer end of the jet typically show a steeper spectrum with spectral indices from -0.5 to -0.6 in hot spots and from -0.8 to -1.0 in lobes.

Two different jet morphologies have been observed for radio-loud AGN, correlated with the radio luminosity at low frequencies. Historically, this correlation was found by Fanaroff and Riley [FR74] for sources observed under a large inclination angle (see below). The luminosity classification is usually done according to L_{178}, the luminosity at 178 MHz [FR74]. AGN with high luminosity are characterized by powerful jets extending far outside the host galaxy. The increasing jet luminosity at the outer end produces extended radio lobes and the so-called hot spots. Less powerful AGN have fainter jets. They show decreasing radio emission with growing

[2]The spectral index α in radio wavelengths is usually determined between 2.7 GHz and 5 GHz.

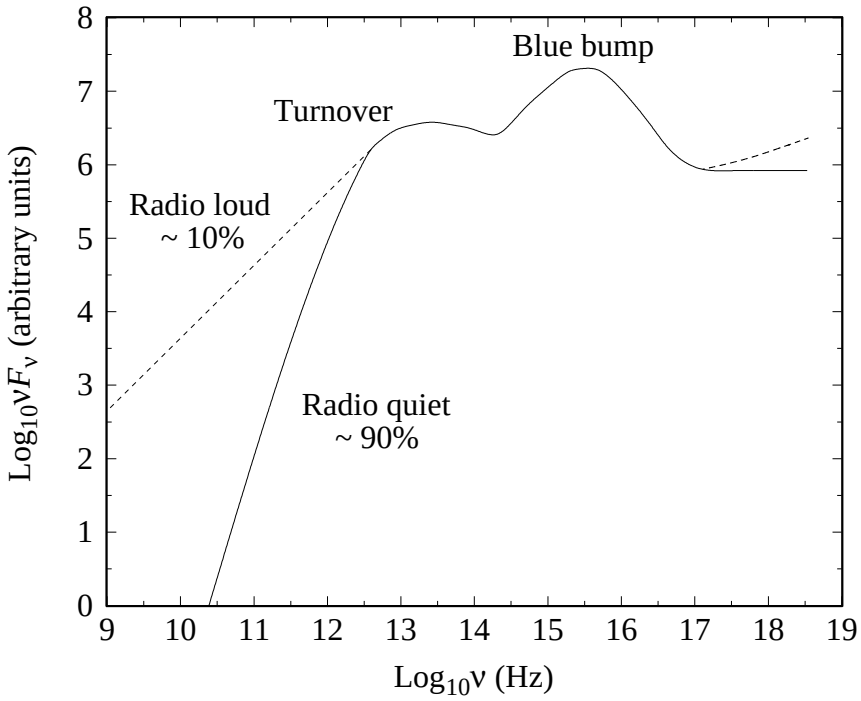

Figure 3.3: Typical photon spectrum of radio-weak and radio-loud AGN. The thermal emission results in a maximum of νF_ν around $\nu = 10^{15.5}$ Hz which is called the blue bump. Below and above this frequency, non-thermal radiation with few features dominates [CO96].

distance from the central black hole, they have no hot spots and seem to be fading out. The critical value was found at $L_{178} = 2.5 \cdot 10^{26}$ W/Hz. In contrast to the jet morphology, the radio luminosity can be observed under a large range of the inclination angles. It is preferred as criterion because it provides a more general classification of AGN based on their intrinsic properties.

According to the model of jet-disk symbiosis, jet and disk luminosity are correlated (see above). This implies automatically correlations between the observed jet luminosity and the bolometric luminosity[3] of the sources. The critical value of L_{178} corresponds to the bolometric luminosity of $L_{bol} = 10^{46}$ erg/s [FMB95, FGKB95].

In addition to the sources following the scheme outlined above, there is a substantial fraction ($\approx 1/3$ when selecting the strongest sources at 5 GHz) of sources showing a steep radio spectrum from the compact radio core for frequencies above a certain turnover frequency[4]. If the turnover is in the range of MHz, the object is classified

[3]The bolometric luminosity L_{bol} is defined as the integrated luminosity over all frequencies: $L_{bol} = \int_{-\infty}^{\infty} L_\nu d\nu$

[4]The emission in the steep spectrum sources discussed above comes from the radio lobes far outside the core.

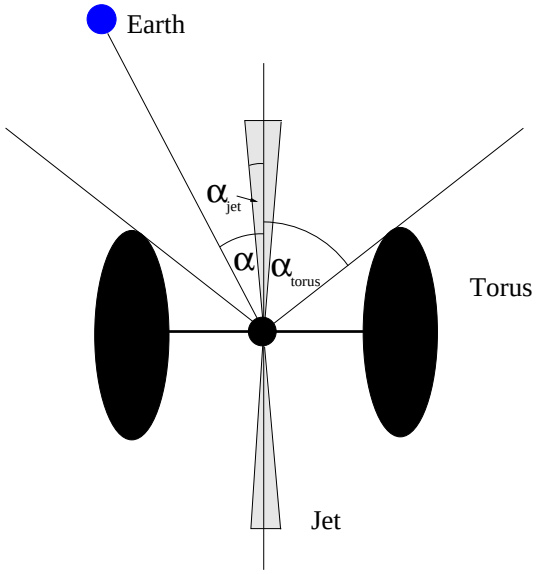

Figure 3.4: The opening angle of the torus is defined as the maximum inclination angle α_{torus} for which the AGN core is not obscured by the torus. The maximum angle, for which the relativistic beaming factor is large than 1 is called α_{jet}.

as *Compact Steep Spectrum* source (CSS), if it is in the range of GHz, the object is a *GHz Peaked Source* (GPS). These sources are significantly smaller than usual AGN. The linear size of GPS is below 1 kpc, the size of CSS is usually in the range of 1 kpc -15 kpc. For comparison, the size of radio-loud AGN is typically in the range of several hundred kpc, while the largest AGN jets reach several Mpc.

GPS and CSS are not distinct source classes. In contrast, there is a continuous transition from the compact GPS to the slightly larger CSS. As pointed out in [O'D98], the turnover frequency ν_m decreases with growing source size l as

$$\nu_m \propto l^{-0.65} . \tag{3.1}$$

The extremely high power of the GPS/CSS suggests a central engine similar to those of other AGN to provide sufficient energy.

The compactness of the sources can be explained by the assumption that the jets get stopped by the interaction with dense matter. The most common interpretation of the turnover observed for this source class is the model of synchrotron self-absorption. However free-free absorption is not excluded, where the photon gets absorbed by a free electron in the electromagnetic field of a second free electron or nucleus in a plasma. The sharpness of the observed maxima implies that the zone of the bulk radio emission is very small [OB97] and located at the outer end of the jet. One idea in this context is that GPS/CSS are just the young states of radio-loud AGN evolving into the larger radio sources. The population statistics of GPS/CSS

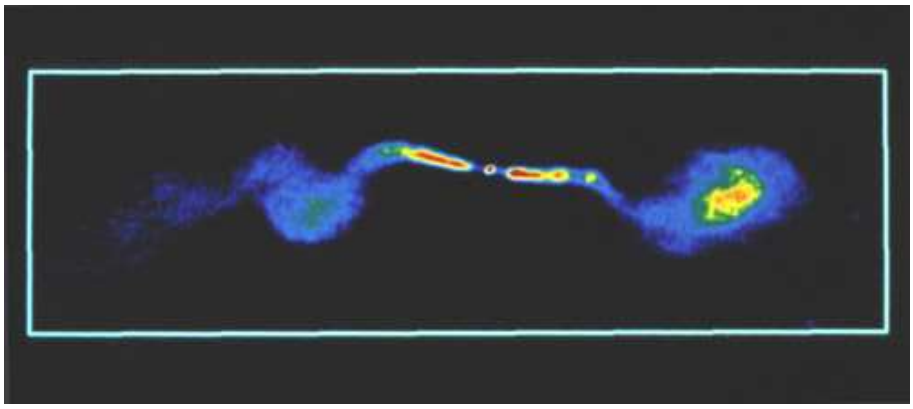

(a)

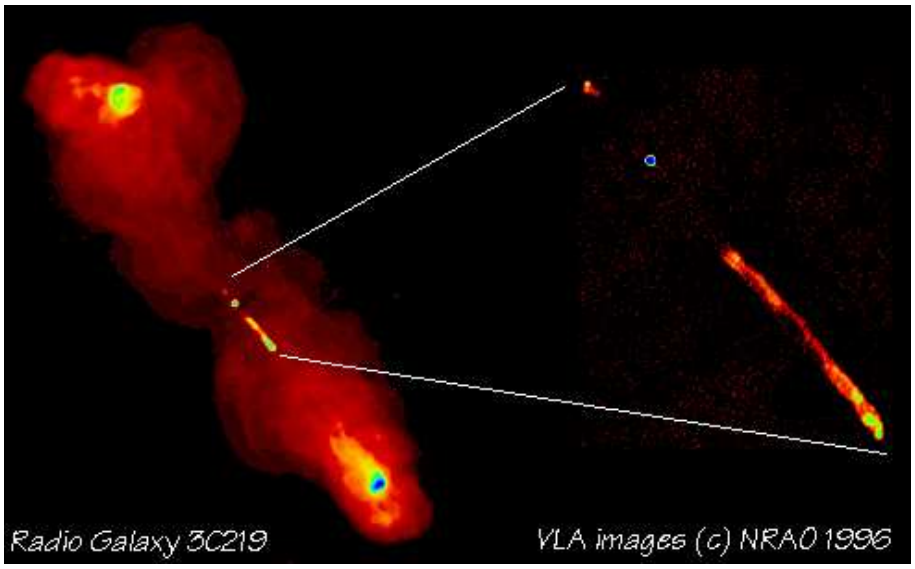

(b)

Figure 3.5: Radio image of the FR-I galaxy 3C 449 (a) and of the FR-II galaxy 3C 219 (b). The FR-II jets end in strong, extended radio lobes with hot spots showing the maximum emission. In contrast the FR-I jets show the most intense emission in the central part of the jets and fades out into lobes with weaker emission. The linear size of 3C 449 is about 200 kpc, the size of 3C 219 is some hundred kpc. Images courtesy of NRAO/AUI.

and extended radio-loud AGN are in agreement with this picture, provided they stay in the compact state for a significant part of their lifetime.

For neutrino production, this class becomes of particular interest assuming proton acceleration within the central part of the jet. The dense matter surrounding the

source provides an ideal target for pion production. As the jets get stopped in the interaction zone, the predicted neutrino production is isotropic or only slightly beamed. Thus, the inclination angle is believed to have only small effects on the expected neutrino flux from this source class.

3.1.2 The influence of the viewing angle: Doppler boost and obscuration effects

The observation of extended radio-loud AGN under different inclination angles α results in different appearances of the same source type due to the relativistic Doppler boost of the emission from the jet and the possibility of the obscuration of the inner core by the torus. In Fig. 3.2, different inclination angles are indicated by arrows and the names of the corresponding AGN class are listed. It is helpful for this classification to define the opening angle of the torus as the maximum inclination angle α_{torus} at which the AGN core is directly visible. Also, α_{jet} is defined as the maximum inclination angle, for which the relativistic beaming factor of emission from the jet is larger than 1. An illustration of α_{jet} and α_{torus} is shown in Fig. 3.4. There are three characteristic ranges of the inclination angle α:

- $\alpha > \alpha_{torus}$: the inclination angle is larger than the opening angle of the torus. The inner core of the AGN is obscured.
- $\alpha_{jet} < \alpha < \alpha_{torus}$: the inclination angle is large enough that emissions from the jet are not enhanced, but smaller than the opening angle of the torus.
- $\alpha < \alpha_{jet}$: the inclination angle of is so small that the observer looks directly into the jet. Any emission from the jet is relativistically boosted towards the observer.

In the case of $\alpha > \alpha_{torus}$, the broad line region and the thermal continuum radiation of the accretion disk cannot be seen and the AGN is called a *radio galaxy*. Low luminosity objects with weaker jets, as defined in Sec. 3.1.1, are classified as FR-I radio galaxies[5]. High luminosity objects are called FR-II radio galaxies [FR74]. Figure 3.5 shows the radio images of a FR-I radio galaxy, 3C 449, and of a FR-II galaxy, 3C 219. The different jet morphologies are clearly visible in the radio images. For 3C 449, the strongest radio emission is close to the center, while 3C 219 shows hot spots with the most intense emission at the outer end of the jets.

The case $\alpha_{jet} < \alpha < \alpha_{torus}$ is only present if the opening angle of the torus is larger than the opening angle of the jet, $\alpha_{torus} > \alpha_{jet}$. In this case the AGN spectrum is dominated by the blue bump from the inner accretion disk and broad emission lines from fast moving dust clouds. The radio spectrum of these objects is still steep and

[5]Here, FR stands for Fanaroff and Riley.

lobe-dominated. Only high luminosity objects show this morphology, referred to as *Steep Spectrum Radio Quasars* (SSRQ) with a bright optical core and strong broad emission lines. The lack of similar low luminosity objects is still a matter of debate. Possibly, the inner core is obscured by the torus until the inclination angle is small enough that the observed emission becomes Doppler boosted [FGKB95].

In the third case, $\alpha < \alpha_{jet} \approx 12°$, the observer is looking into the jet under a very small inclination angle so that the radiation from the jet is Doppler boosted due to relativistic motion of the bulk outflow towards the observer. These objects are characterized by a flat radio spectrum, strong variability and polarization. The dominance of the beaming effects is taken into account by the combination of *Flat Spectrum Radio Quasars* (FSRQ) and BL Lac objects into the blazar class. BL Lac objects are interpreted as low-luminosity objects with a FR-I type jet seen from small inclination angles, while FSRQ are considered as the high luminosity objects (FR-II jet). The flat radio spectra of blazars can be explained by the dominance of the boosted flat-spectrum core over the non-boosted steep-spectrum radio lobes and will be used as a selection criterion for blazars. A flat spectral index itself is an indicator of an optically thick source, while the optically thin synchrotron spectrum is steep. If the size of the visible region increases with energy, the spectrum gets flattened. This mechanism results in a prediction of a flat radio spectrum for the inner most part of the jets.

The BL Lac objects are commonly divided into high energy cutoff BL Lac (HBL) and low energy cutoff BL Lac (LBL) referring to the maximum energy of the electron synchrotron spectrum. The radio emission of HBL is relatively weak, while they are strong X-ray emitters. The bolometric luminosity of HBL is significantly smaller than of LBL. A distinction between these classes is usually made by taking into account whether the radio-to-X-ray spectral index α_{rx} (with $F(\nu) \propto \nu^{\alpha_{rx}}$) is greater (LBL) or less (HBL) than -0.75 [UP95].

The high energy γ emission of HBL and LBL differs in the photon energy, where high emission has been observed. Many LBL have been detected by EGRET at GeV energies [H$^+$99], while some HBL turned out to be emitters of TeV photons. In fact, all confirmed TeV blazars are HBL[6] [Wee03a]. Furthermore, only 2 of the 6 confirmed TeV blazars have been detected by EGRET, but the flux is only moderate [H$^+$99]. In this way, the high energy emission of LBL is similar to FSRQ, which turned out to be the strongest GeV emitters.

The observed numbers of the various subtypes of radio-loud AGN are in agreement with this interpretation of the empirically defined classes, when assuming a typical value of the Lorentz factor $\gamma \approx 10$ for the bulk motion in the jet [UP95]. This value is also supported by the observed apparently superluminal motion of radio knots in blazar jets [Man97], which is consistent with this value of γ.

[6]However, there are indications of TeV radiation from BL Lacertae (LBL) and M87 (misaligned BL Lac or FR-I) weakening the association.

Radio-weak AGN are classified analogously according to luminosity and the inclination angle. The luminosity at optical wavelengths is used for the classification. Intrinsically stronger objects are called radio-weak quasars[7] and Radio Intermediate Quasars (RIQ). Intrinsically weaker objects are named Seyfert galaxies. As for the radio-loud AGN, the inclination angle determines the relativistic beaming of emission from the jet and the obscuration of central emission by the torus. Radio-weak quasars are optically strong objects seen from moderate inclination angles ($20°-60°$), RIQ are interpreted to be the same objects, but seen from small angles. The radio emission of RIQ is relativistically beamed analogously to blazars [FSP96]. Seyfert galaxies are classified as Seyfert 1 galaxies, if the core including the broad line region are visible, or as Seyfert 2 galaxies, if the core is obscured by the torus [C+00]. Up to now, no Seyfert-like objects with beamed emission have been observed.

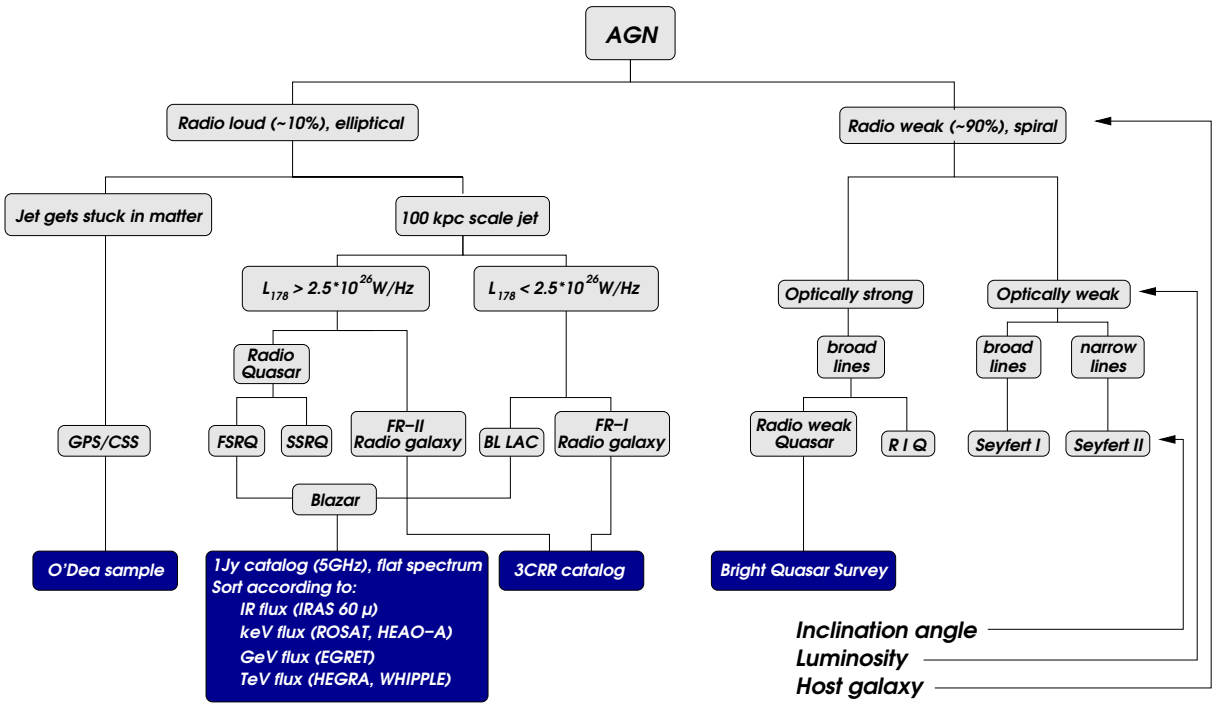

Figure 3.6: AGN classification according to host galaxy, luminosity and inclination angle. In the scheme, SSRQ and FSRQ stand for Steep Spectrum Radio Quasar and for Flat Spectrum Radio Quasar. Radio Intermediate Quasars are labeled RIQ. The GHz Peaked Sources and the Compact Steep Spectrum sources are represented by GPS/CSS. The boxes on the bottom indicate catalogs used for the selection of the corresponding AGN classes (see below).

[7] Sometimes called QSO for quasi-stellar objects. In that terminology, the term "quasar" is restricted to radio-loud sources.

3.1.3 Overview of the AGN classification scheme

The derived classification of AGN depends on the morphology of the host galaxy, on the luminosity and on the angle of observation. It is summarized in a tree scheme of AGN, which is displayed in Fig. 3.6. The division of AGN into radio-loud and radio-weak sources is indicated by the first branching of the classification scheme. The classification of radio-loud AGN, which form the left branch of the tree, is summarized first. Then, the classification of radio-weak AGN is reviewed according to the right branch of Fig. 3.6.

Different lengths of the radio jets of radio-loud AGN yield a separation into compact objects and AGN with fully evolved jets of a length above 100 kpc [O'D98]. The large scale radio-loud AGN branch into two classes defined according to the luminosity at 178 MHz, L_{178}. This luminosity is correlated with two different jet morphologies (FR-I and FR-II type): objects with $L_{178} > 2.5 \cdot 10^{26}$ have FR-II type jets, the other have FR-I type jets. If seen under an increasing inclination angle[8], the low luminosity objects appear as BL Lac or as FR-I radio galaxies. The high luminosity objects appear as Flat Spectrum Radio Quasars (FSRQ), as Steep Spectrum Radio Quasars or as FR-II radio galaxies.

For the radio-weak AGN, forming the right branch of Fig. 3.6, a luminosity dependent classification in optical wavelengths yields the division into Seyfert galaxies and quasars. Different inclination angles yield the appearance as radio-weak quasars or Radio Intermediate Quasars (RIQs) [FSP96], respectively as Seyfert I or Seyfert II galaxies.

3.2 Motivation for a selection scheme of neutrino source candidates

Neutrino production from relativistic hadrons requires the interaction of hadrons with ambient photons or other hadrons. In these interactions, neutral and charged pions are produced in the same order of magnitude as discussed in Sec. 2.1.1. Since neutral pions decay into gamma rays, while charged pions decay into neutrinos, photon and neutrino production are correlated. In most scenarios, if photon and proton spectra fall steeply with energy, the production and subsequent decay of the Δ resonance dominates the pion production. Then, the contribution of higher resonances and multi-pion production is only a small correction to the pion production rate. The acceleration of the protons is assumed to be due to shock acceleration which may take place in the relativistic jet [Man97, BS87] or in the accretion disk [S$^+$91, NMB93]. Due to the low plasma density in the AGN jets the *pp* processes are less likely to be the dominant process [Man97]. If the acceleration takes place

[8] The inclination angle is defined as the angle between the line of sight and the AGN axis.

in the disk, the electromagnetic cascades initiated by the photons produced in the decay of neutral pions would lead to a non-thermal X-ray spectrum from the disk. However, observations of AGN X-ray spectra and the diffuse X-ray flux show the dominance of the thermal flux, which is peaked around 100 keV [LM00]. A possible way out would be down-scaling the non-thermal X-ray spectrum to a value of 30% (or less) of the measured X-ray flux [SS96], so that the non-thermal X-ray spectrum from the hadronic interactions is not dominant. This implies a down-scaling of the predicted neutrino spectrum by the same factor. The lack of absorption lines in the X-ray spectra of AGN constraints *pp* interactions. Thus, $p\gamma$ interactions dominate over *pp* interactions in neutrino production in the disk [SS96]. An exception may be given, if *pp* interactions take place at the inner edge of the accretion disk [NMB93].

For the jet as well as for the disk, the theory of diffusive shock acceleration suggests a power law spectrum with a differential spectral index $\alpha \approx 2$ for protons [Bel78a, Bel78b, Pro98]. Neutrinos and photons are produced with the same index if multi-pion production is not dominant. However, the correlation between neutrino and photon spectra is not necessarily conserved for an observer at Earth. The energy of the photons may be redistributed by synchrotron pair cascades to photons of lower energy. The escape energy of the photons depends on the optical depth and an accumulation of photons at the escape energy is expected. Though the spectral index may be distorted by these processes, the bolometric luminosity remains constant [MPR01].

Hadronic jet models have been proposed to explain the origin of highly energetic γ emission from the jet. In [Man97], they are compared with purely leptonic models, where the highly energetic (TeV) radiation is explained by Inverse Compton Scattering (ICS) of photons. Models in which the photons originate as synchrotron radiation are classified as Synchrotron Self Compton (SSC); those in which the photons are ambient are classified as External Compton (EC). In the SSC models, the ratio between GeV and radio luminosity is restricted, predicting a larger number of GeV blazars than observed by EGRET. Additionally, it implies necessarily that keV and TeV fluxes are correlated. Observations indicate that these correlations are not always present [H$^+$02b]. Especially the existence of orphan flares, where the TeV flux flares but not the X-ray flux, supports hadronic models. Orphan flares have been observed for 1ES 1950+650 [K$^+$04] and for Mrk 421 [B$^+$05, C$^+$05].

The EC model requires high densities of external photons to be Compton up-scattered to higher energies. These photon densities then restrict the energy of escaping photons to O(1 TeV). Thus, the leptonic External Compton model cannot explain the observed sources reaching photon energies above 10 TeV [Man97].

Given these arguments, there are reasons to consider hadronic models. In most hadronic models, the emission of high energy photons in the jet is not assumed to be directly from photohadronic processes. A non-negligible optical depth makes TeV photons cascade to lower energies. Thus, an additional mechanism for the produc-

tion of the high energy γ radiation is necessary. In proton initiated cascade models (PIC), it is assumed that electrons scatter up some target photons to higher energies. In the SS-PIC (self synchrotron PIC) model, the target photons are those emitted in the cascades. The EC-PIC (external Compton PIC) assumes external photons to be scattered up to higher energies by the inverse-Compton process [Man97].

Another possibility to explain the high energy γ emission is given by the Synchrotron-Proton Blazar model proposed by Mücke and Protheroe [MP01a] assuming relativistic protons to emit synchrotron radiation at higher energies than the synchrotron radiation from gyrating electrons. The observed double hump photon energy spectrum can be explained by this model and the calculated neutrino emission spectra for HBL and LBL have been [MP01b]. The emission of TeV γ-rays via synchrotron radiation requires protons to reach extreme high energies. This is only possible if the interaction rate is sufficiently low. Hence, in the TeV emitters $p\gamma$ and pp interactions must be less frequent than in blazars without intense TeV photon emission. This results in predictions of neutrino fluxes for LBL being 6 orders of magnitude larger than for HBL.

3.3 Catalogs of AGN classes

In this section, the AGN classification presented in Sec. 3.1 is used to define catalogs of AGN classes by a set of selection rules from existing astronomic catalogs. These catalogs will be used below as the basis of the selection of candidates for a high neutrino emission.

The applied selection criteria are motivated by the properties of the corresponding AGN class. The choice of the astronomical catalogs is restricted to those which cover all sources in well-defined parts of the sky above a well-defined threshold, i.e. it is restricted to statistically complete catalogs. This ensures properly defined source classes. Due to limitations on the availability of data, the photon data are in general not taken simultaneously with the considered data set collected by AMANDA or, generally speaking, with the operation of modern neutrino telescopes. Thus, long time variations of the considered sources could not enter the selection.

Sources in the galactic plane are excluded from the selection in order to avoid the inclusion of galactic sources in the samples of extragalactic AGN. The cut value on the galactic latitude b is set to be $|b| > 10^\circ$, except for the radio-weak quasars, where the selection of the used catalog requires $|b| > 30^\circ$. Only sources above a minimum declination $\delta > 10^\circ$ are selected.

For most catalogs, a cut on the distance corrected flux is applied in order to exclude intrinsically weak, though appearing bright, nearby sources which might otherwise migrate into the catalog. Although these nearby sources differ in many aspects from the more distant sources, they may also be good candidates for high neutrino

emission. Due to their individuality, they should be considered separately as single candidate sources in a point source analysis. For the formula used for the correction see appendix B.

The detailed selection rules for the individual samples are listed in Tab. 3.1. In the following, the selection rules for the individual samples are briefly discussed.

Sample	Flux /luminosity cuts	Coordinate cuts	Further cuts
Blazars	$F_{5GHz} > 0.8$ Jy, $F_{5GHz}^{z=0.1} > 1.5$ Jy	$\delta > 10°, \lvert b\rvert > 10°$	$\alpha > -0.5$ with $F_\nu \propto \nu^\alpha$
CSS	$F_{178MHz} > 10$ Jy, $\log P_{178MHz} > 26.5$	$\delta > 10°, \lvert b\rvert > 10°$	Lin. size < 20 kpc
GPS	$F_{5GHz} > 1$ Jy, $\log P_{5GHz} > 26.5$	$\delta > 10°, \lvert b\rvert > 10°$	0.4 GHz$< F_{max} <$ 6 GHz
FR-I	$F_{178Mhz} > 10$ Jy, $L_{178MHz} < 2.5 \cdot 10^{25}$ W/Hz	$\delta > 10°, \lvert b\rvert > 10°$	
FR-II	$F_{178Mhz} > 10$ Jy, $L_{178MHz} > 2.5 \cdot 10^{25}$ W/Hz	$\delta > 10°, \lvert b\rvert > 10°$	
QSO	$B < 16.16$, $U - B < -0.44$	$\delta > 10°, \lvert b\rvert > 30°$	

Table 3.1: The selection criteria defining catalogs of the different source classes. F_ν stands for the photon flux at a certain frequency ν in Jy, $\log P_\nu$ is the logarithmic power in W/Hz at a certain frequency ν and L is the luminosity. The declination is labeled as δ while b stands for the galactic latitude. For the blazars, the spectral index α is determined between 2.7 GHz and 5 GHz. For CSS selected at 2.7 GHz, a back-extrapolation of a steep spectrum component to 178 MHz was used instead of the measured 178 MHz flux. U is the magnitude of the UV flux ($\lambda = 300$ nm-400 nm), B the magnitude of the blue flux($\lambda = 400$ nm-550 nm).

Blazars As explained in Section 3.1, blazars are characterized by a flat radio spectrum, which is used as the selection rule in this thesis. For radio sources with high fluxes at 5 GHz, Kühr et al. [K$^+$81b] worked out a critical and cross-calibrated complete catalog for sources up to a flux level of 1 Jy[9] for galactic latitudes $|b| > 10°$. A second version also covers sources below this threshold, using data available up to 1981 [K$^+$81a]. In the Northern Sky, this catalog contains the "strong surveys" S1$-$S5 [P$^+$72,PK72,P$^+$78,K$^+$81c]. For the corresponding areas of the sky examined, they are complete at least up to 0.8 Jy and they cover nearly the complete Northern Sky with $|b| > 10°$.

The selection rules result in the blazar catalog consisting of about 150 sources.

[9] $1\text{Jy} = 10^{-26}\text{Ws}^{-1}\text{m}^{-2}$, sometimes also called f.u. for flux unit.

GPS and CSS The catalog of compact sources is defined according to the selection of O'Dea [O'D98]. The sample defined there contains former selections of CSS by Fanti et al. [F+90] and of GPS by Stanghellini et al. [S+98].

Since CSS and GPS are characterized by a maximum in the radio flux at a size-dependent frequency, the selection of these sources is done at several frequencies, 178 MHz, 2.7 GHz and 5 GHz, tracing the peak location.

From the original CSS samples, all sources have been removed which are marked in the original paper not to fulfill all selection rules [F+90]. The same has been done with CSS and GPS sources where newer data do not fulfill the criteria anymore [O'D98]. Additionally, a cut on the absolute power at 5 GHz is put, similar to the luminosity cut for the CSS sources. The generic spectra of sources are plotted in Fig. 3.7.

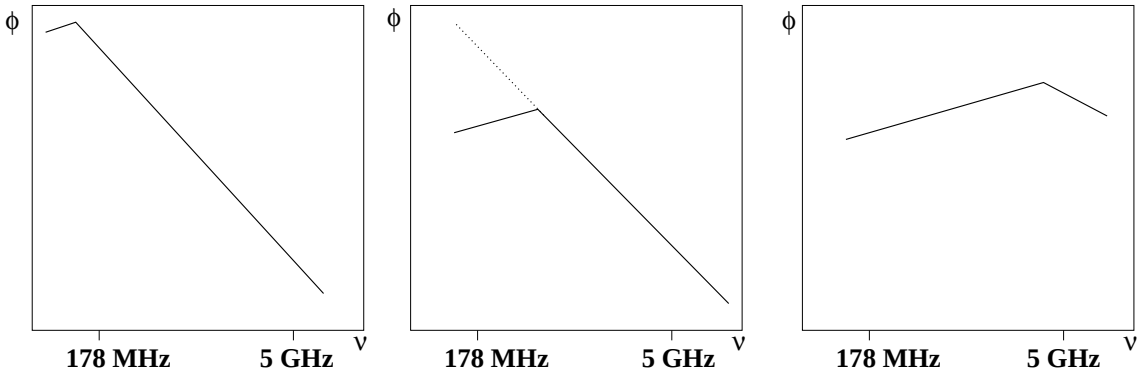

Figure 3.7: Schematic double logarithmic plot of radio spectra of sources fulfilling the different selection rules for CSS and GPS: on the left, a typical spectrum of a CSS selected at 178 MHz is displayed. In the middle, the spectrum of a CSS source with the maximum near 2.7 GHz is plotted and on the right the spectrum of a GPS selected at 5 GHz is displayed. Note, for the sources selected at 2.7 GHz, the back-extrapolation of the steep spectrum component to 178 MHz is relevant for the selection.

In total, 40 sources are selected of which 9 are exclusively GPS and 23 are exclusively CSS. 8 sources fulfill both, the GPS and the CSS selection rules.

FR-I and FR-II-radio galaxies As the distinction between FR type I and type II radio galaxies is made at 178 MHz, it is adequate to select radio galaxies from observations at this frequency. Data at this frequency are available from the 3C catalog in its revised version (3CRR) [S+85]. The possibility of a classification into FR-I and FR-II galaxies depends on the availability of the redshift for the source, since the distance information is necessary to calculate the luminosity from the observed flux. For all considered sources, the redshift and the classification into FR-I and FR-II is available from [L+83]. The selection results in a catalog of 24

FR-I and 122 FR-II galaxies. Additionally, 16 compact sources fulfill the selection. They belong to the CSS source class as discussed above and consequently, they are removed from the FR-I and FR-II samples.

Radio-weak Quasars A complete catalog of quasars selected at optical to UV wavelengths is given by the *Bright Quasar Survey* (BQS) covering the sky with $\delta > -10^\circ$ and $|b| > 30^\circ$ [SG83]. A quasar is identified by an excess of UV flux. The catalog (in its variety presented by Sanders et al. [S$^+$89]) contains in total 109 sources, of which 59 sources are radio-weak quasars in the sky viewable by AMANDA.

3.4 Selection of neutrino source candidate lists

In this section, the catalogs of AGN classes defined in Sec. 3.3 are ordered with respect to their possible neutrino production according to phenomenological criteria. The ordering scheme is motivated by the correlations between between photons and neutrinos produced in pion decay discussed in Sec 3.2. It is independent of detailed AGN models making predictions on the absolute neutrino flux for individual AGN.

The assumed neutrino production from pion decay results in correlations between the production rate of neutrinos and of photons. Since the optical depths of AGN remain unknown, the escaping photons can be of significantly lower energy than the neutrinos. This is taken into account by the selection of source candidates at various energies into different candidate samples. Samples at different energy bands (radio, IR, optical, keV, GeV, TeV) are defined, always assuming that the observed photon flux is proportional to the TeV ν signal. The values for the selection frequency are restricted by the availability of suitable data.

3.4.1 Blazars

Since the observer is looking into the jet, blazars are candidate sources to test for beamed neutrino production in the jet. Corresponding to different assumptions on the optical depth of blazar jets, the neutrino flux of blazars is assumed to be proportional to the photon flux at energies of TeV (HEGRA, Whipple), GeV (EGRET), keV (HEAO-A, ROSAT) or infrared (IRAS 60 μm).

The ordering of the sources is done according to the flux in the relevant energy range. For the resulting samples, the relative strengths of the sources at the selection energies are displayed in Fig. 3.8. The strongest source strength of each sample is normalized to one.

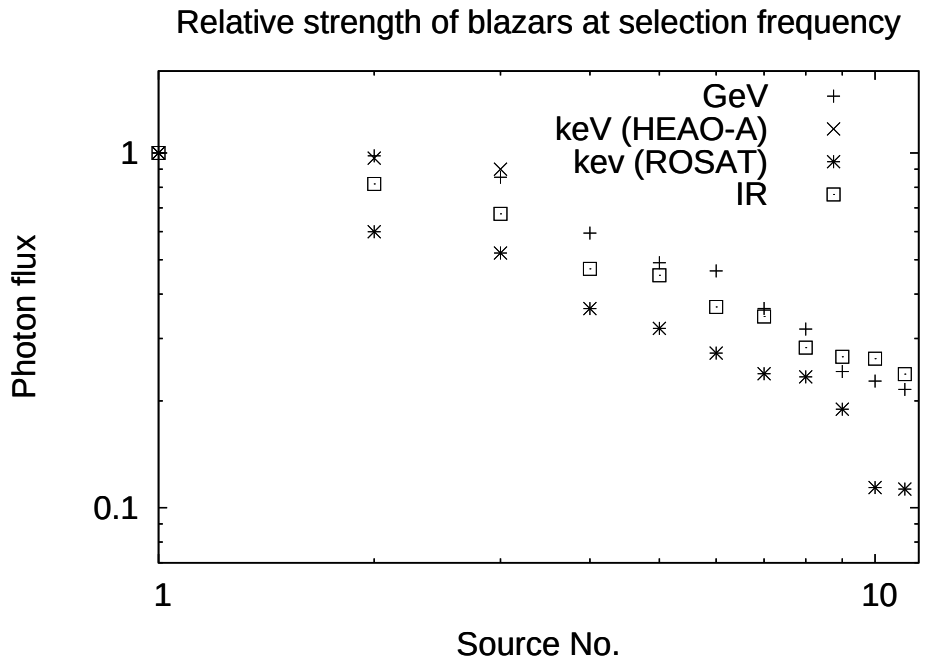

(a)

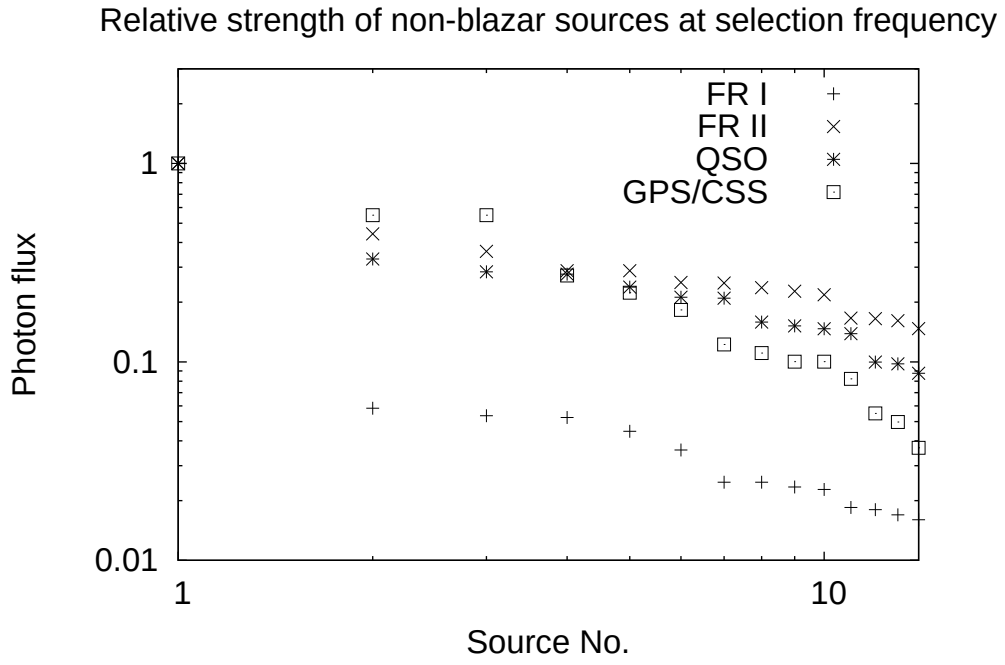

(b)

Figure 3.8: Relative strength at selection energy of strongest sources in blazar samples (a) and in non-blazar samples (b).

IR loud blazars The Infrared Astronomical Satellite (IRAS) provides a survey at the wavelengths of 12μm, 25μm, 60μm and 100μm. The Faint Source catalog IRAS F, covering most parts of the sky outside the galactic plane, includes 173,044 sources [M$^+$90]. From the defined blazar sample, in total 12 sources are found in the IRAS F catalog. The IR selected sample is displayed in Table C.1. The flux at 60 μm is considered for the ordering of the sources.

X-ray blazars (HEAO-A and ROSAT sources) In the X-ray regime, there are only a few all-sky surveys. For hard X-rays ($0.25 - 25$ keV), there exist only the HEAO-A measurements performed in the 1970s with low sensitivity and poor angular resolution. The results are listed in the 1H catalog [W$^+$84], containing 842 sources.

The X-ray satellite ROSAT performed an all-sky survey in the $0.2 - 2.4$ keV energy band with high sensitivity and good angular resolution in the range of a few tens of arc-seconds. The strongest sources found in the all-sky survey are listed in the 1RXS catalog [V$^+$99], which contains in total 18,811 sources.

For these antipodal experiments, two separate candidate lists are constructed from 1RXS and 1H sources identified with blazars corresponding to the hypotheses that soft and hard X-ray emission, respectively, is positively correlated with TeV neutrino production. This resulting selections are listed in Table C.3 for HEAO-A and in Table C.2 for ROSAT.

GeV blazars (EGRET sources) In the GeV energy range, the most sensitive data are those collected by the EGRET experiment on board the CGRO satellite [CGR]. The third EGRET catalog (3EG) [H$^+$99] contains 271 sources in total of which 66 have been identified with blazars. Additionally, for 27 sources associations with blazars exist with lower confidence.

EGRET sources are selected by the requirement of a reliable identification with a source of the blazar sample (class 'A' in the 3EG catalog). Weakly identified EGRET sources (class 'a' in the 3EG catalog) are accepted only if an independent analysis confirms this identification [SERM03]. The sources are sorted according to the maximum flux detected by EGRET. This yields the source sample in the sky viewable by AMANDA presented in Table C.4.

The largest fraction of EGRET sources has not been identified with sources detected at other wavelengths up to now. Although a large fraction of these sources is likely to be galactic, some are probably extragalactic. Three different types of presumably galactic sources have been discussed, two are concentrated on the galactic plane with $|b| < 5^\circ$, while the third is associated with the Gould belt [G$^+$00]. The latter form the so-called Local Gamma-Ray Population characterized by weak, but constant fluxes below $2.4 \cdot 10^{-7}\mathrm{s}^{-1}\mathrm{cm}^{-2}$ and a soft spectrum (photon spectral index $\gamma \approx 2.45$); they reach galactic latitudes up to 30°. Sources outside the galactic plane which do not

show these characteristics are most likely extragalactic. These sources show a high variability, even higher than the identified AGN. However, the assumption that they may also be powered by an AGN can explain their energy supply even if they are located at large distances. Together with the non-confirmed 3 EG-'a' identifications, they are included in the analysis as a further sample.

The sources with $\delta > 10^\circ$ and $|b| > 10^\circ$ not showing the characteristics of the Local Gamma-Ray Population are listed in Table C.5. The selection is taken according to the maximum GeV flux detected.

TeV blazars Up to now, only 6 blazars have firmly been detected emitting TeV photons, of which 5 are located in the sky viewable by AMANDA [Wee03a, Boj03]. All TeV blazars show extreme variability in flux, such that a flux ranking becomes impossible. The radio flux of all TeV blazars is weak and it does not fulfill the presented radio selection rules for blazars. Furthermore, due to absorption by the IR background, only nearby sources can contribute to the TeV photon flux.

These conditions prevent the use of the presented selection scheme for TeV blazars. But since TeV photons are the most relevant for TeV neutrinos in the optically thin case, the radio requirements are skipped for TeV blazars and all TeV blazars are selected for the source stacking analysis. The sources are listed in Table C.6.

3.4.2 GPS and CSS

As the CSS and GPS catalog has been selected at three different frequencies, each selection criterion at radio wavelengths would bias the selection either towards CSS or GPS. Since there are only few X-ray or IR data for these sources, the only possibility to get a suitable source ranking is to select according to the optical strength of these sources. Here, the hypothesis that the TeV neutrino flux is proportional to the optical flux is used. The optical magnitudes for CSS and GPS are taken from [O'D98], the resulting source catalog is displayed in Table C.7.

3.4.3 FR-I/II radio galaxies

As the jets of FR-I/II radio galaxies do not point towards the observer, a neutrino flux produced in the jets is expected to be weaker for these sources than for blazars. However, neutrino production in the disk is expected to be less anisotropic than is the radio emission at low frequencies. Thus, a sample of these sources may test for neutrino production there. For the selection, the radio flux at 178 MHz is assumed to be proportional to the TeV neutrino flux. Hence, these fluxes are used as criterion to sort the samples of radio galaxies. The sources are listed in Table C.8 for FR-I and in Table C.9 for FR-II galaxies.

3.4.4 Radio-weak quasars

Multi-wavelength investigations of the BQS quasar sample show a second maximum in the photon spectrum in IR wavelengths for some quasars [S$^+$89]. Assuming that an excess in the infrared indicates neutrino production at the source, radio-weak quasars are selected according to their photon flux at 60μm. The quasar catalog is listed in Table C.10.

3.4.5 Nearby sources

Some blazar sources have been removed from the catalogs by a cut on the distance corrected flux. If that cut was the only reason to remove them, these sources are listed in Table C.11.

Some well-known nearby AGN satisfy several selection rules, when skipping the cut on the distance corrected flux. NGC 1275 would be in the IR-blazar and in both keV-blazar samples and Mrk 501 would be in both keV samples. The occurrence of these sources in various samples confirms our assumption that these sources migrate into the samples due to their proximity and should not be considered as generic sources. Anyhow, they may be relevant neutrino sources. Therefore, it is useful to analyze them as individual candidate sources. All of these nearby candidate sources are included in the standard set of AMANDA preselected candidate sources [A$^+$04c, A$^+$05c, A$^+$05d].

3.5 Analysis of the flux from source classes: Source stacking versus standard techniques

The samples of generic AGN classes are defined in order to analyze the underlying hypotheses on the neutrino flux. Source stacking aims for an improvement of the sensitivity to these hypotheses by the evaluation of the cumulative signal of several generic sources. This method is compared with standard analysis techniques, the analysis for the flux from single candidate sources and the analysis of the diffuse extraterrestrial flux. An improvement with respect to the point source analysis can only be achieved, it there are several sources contributing similar fluxes. In contrast, the diffuse analysis is more sensitive if there is a very large number of sources with nearly the same flux. In this section, this qualitative expectation is analyzed quantitatively by considering a parameterization of the flux from each source as a function of the ordered source number.

The relative flux of the n^{th} source, $F(n)$, is parameterized by a power law,

$$F(n) \propto n^{\alpha} \,. \tag{3.2}$$

This parameterization is motivated by the nearly linear decrease of $F(n)$ in the double logarithmic plots in Fig. 3.8. A fit of α on the flux distributions of the AGN samples results in $\alpha = -0.6$ for FR-II radio galaxies and for IRAS blazars, a 2-point index $\alpha = -4.1$ for the two strongest FR-I radio galaxies and $-0.7 \geq \alpha \geq -1.1$ for the other samples.

If the number of observed events is sufficiently high so that Gaussian statistics can be applied, the significance of an observation is given by $S/\sqrt{BG}$, where S is the number of signal events and BG is the number of background events. The number of signal events from each source, S_n, is proportional to the flux of the source, $F(n)$ and BG is a constant. Then, the cumulative signal of n sources is given by $S(n) = \sum_{i=1}^{n} S_i$ and the background is $BG(n) = n \cdot BG$. In this case, the significances for all values of n scale linear with the signal normalization and thus the optimum configuration is independent of the normalization.

In the optimization of the number of sources to include, three different cases can occur:

- The expected significance always decreases, if further sources are included. The point source analysis of the strongest source is most sensitive.
- The expected significance increases as a function of the number of sources until a certain maximum at n sources and decreases again for more sources. The source stacking analysis of the n strongest sources is most sensitive to the considered hypothesis.
- The expected significance always increases, if further sources are included. The diffuse analysis is more sensitive to the considered hypothesis. In case of a signal detection in that analysis, source stacking of a limited number of sources could be used to identify the source class responsible for the observed flux.

The first case is given, if $S_2/\sqrt{2BG} < S_1/\sqrt{BG}$, i.e., if $\alpha < -1.27$, the third case occurs if $\alpha > -0.5$. For $-1.27 < \alpha < -0.5$, a gain in sensitivity is obtained by source stacking. For almost all considered samples, the fitted value of α is within this range and thus, source stacking is more sensitive than standard methods. Only for FR-I radio galaxies the point source analysis of the strongest source only is more sensitive due to the dominance of this source, M87. The index for FR-II radio galaxies is close to the critical value of -0.5, above which the diffuse analysis is more sensitive.

The properties of the neutrino telescope used for the analysis can modify the results for two reasons. If the event rates are small, Poisson statistics have to be applied and the critical values of α get slightly dependent on the signal normalization. Furthermore, the finite size of the search bins limits the number of sources to be considered by the condition not to cover a significant fraction of the sky (e.g. 10%) with search bins. The latter effect may decline the range where stacking is more sensitive than

the diffuse analysis, depending on the angular resolution of the detector. For the AMANDA neutrino telescope, these influences are discussed in Chapter 5, where the derived AGN selections are analyzed for a neutrino flux using data from AMANDA.

3.6 Discussion

In this chapter, samples of AGN classes have been defined and sorted with respect to their expected neutrino flux according to phenomenological principles. The measured photon flux is used as an estimate of the neutrino flux, based on the model-independent assumption that the neutrino flux is correlated with the photon flux. The variation of the energy where the photon flux is considered is motivated by the unknown optical depth of AGN for high energy photons.

Given these sorted lists of candidate sources, different methods for an analysis of these source classes for a neutrino flux have been discussed. The source stacking method has been compared with with the analysis of single candidate sources and with the diffuse analysis. For most samples, source stacking is more sensitive to the hypothetical neutrino fluxes than the other methods.

In contrast to to the model-independent source selection scheme presented in this thesis, it is possible to follow an explicitely model-dependent ansatz. For example, calculations using the framework of the jet-disk symbiosis [FB95, FMB95] have been used for predictions of the diffuse neutrino flux from AGN [BBR05]. Within this model, predictions on the flux of individual sources can be derived, if parameters of individual sources are considered instead of average parameters.

However, many parameters of the currently considered theoretical AGN models are not known in detail for the actually observed AGN. These uncertainties result in most models in very large uncertainties of the predicted neutrino flux. A model-independent ansatz avoids these uncertainties and thus it is applied in this thesis.

4

The AMANDA neutrino telescope

4.1 High energy neutrino telescopes

The small cross sections of neutrinos for any interaction with matter make neutrino astronomy a technical challenge. A neutrino detector has to cover a large volume in order to provide the observer with sufficiently high neutrino induced event rates.

A neutrino detection is possible, if it undergoes a charged current or a neutral current interaction with a nucleus within or close to the detector. In a charged current interaction, a lepton l of the same flavor as the original neutrino is generated,

$$\nu_l + \text{nucleon} \rightarrow l + \text{hadronic / electromagnetic cascade}\,. \tag{4.1}$$

A hadronic and an electromagnetic cascade develop from the interaction vertex. The lepton and the cascade particles emit Cherenkov light. Thus, large neutrino detectors can be constructed, where the particle detection is based on the Cherenkov effect (see 2.1.2). If transparent media like water or ice are instrumented with photomultiplier tubes (PMTs), the Cherenkov photons may be detected at some tens of meters from their emission. The absorption length of the detection medium determines the distance from the particle track, in which a detection is possible.

While electrons lose their energy rapidly and taus decay very close to their production vertex, muons travel long distances through the medium. Thus, muons generated far outside the detector can be detected and the effective interaction volume for muon neutrinos is larger than for other flavors. This makes Cherenkov detectors most sensitive to muon neutrinos. At the vertex, most of the momentum of the high energy muon neutrino is transfered to the muon. Therefore, the angle Ψ between neutrino and muon is small. It is parameterized by

$$\Psi = 0.7^\circ \cdot \left(\frac{E_\nu}{\text{TeV}}\right)^{-0.7} \text{[LM00]}\,. \tag{4.2}$$

Medium	Absorption length	Scattering length
ice	110 m	20 m
water	50 – 60 m	2000 m

Table 4.1: Average absorption length and scattering length in water [LM00] and in ice [A+04b].

The measurement of the arrival time of Cherenkov photons at several positions allows for a reconstruction of the Cherenkov cone. The muon track can be determined from the Cherenkov cone. The reconstructed muon track serves as a good approximation of the neutrino track. The reconstruction of the arrival direction of neutrinos detected by hadronic and electromagnetic cascades in the detector is also possible, because the cascades do not develop spherically symmetric. However, the lack of a long lever arm in practice results in larger uncertainties.

The reconstruction quality of events in Cherenkov detectors strongly depends on an accurate measurement of the arrival times of the photons. If photons get scattered in the detector medium, the Cherenkov cone gets fuzzier with a growing distance from the particle track and the track reconstruction gets unsharp. Thus, in addition to the absorption length, the scattering length is an important parameter to describe the quality of the detector medium.

Both water and ice are used to construct neutrino telescopes based on the Cherenkov effect. Average parameters for these media are listed in Table 4.1. The advantage of ice is the larger absorption length. The smaller scattering length, however, results in a smaller fraction of photons reaching the PMTs unscattered. For experiments in water, there are two further challenges. In salt water the noise rate of the PMTs gets enhanced by the emission of light in the decay of ^{40}K. Also, the bioluminescence of microorganisms approaching the OMs increases the noise rate in water [M+03].

In water, there are several experiments running [DB02], under construction [ANT97] and under study [NEM, BTV95, KM3]. In ice, the Antarctic Muon And Neutrino Detector Array (AMANDA) [G+05b, AMA] located at the geographic South Pole has been operating for several years. It provides the greatest sensitivity of all operating neutrino telescopes. The IceCube [A+04d] telescope is currently under construction at the same place as AMANDA. It will fill a cubic kilometer scale and AMANDA will be integrated into IceCube as a more densely instrumented volume.

AMANDA was built in the years 1995 - 2000 in the Antarctic ice sheet. The final detector configuration is called AMANDA-II. It consists of 677 optical modules (OMs) containing PMTs on 19 strings. Figure 4.1 shows the scheme of the AMANDA-II detector, which has been operating since the year 2000. The geometrical shape of the detector roughly follows a cylinder with a diameter of 200 m. Most modules are concentrated at depths between 1500 m and 2000 m.

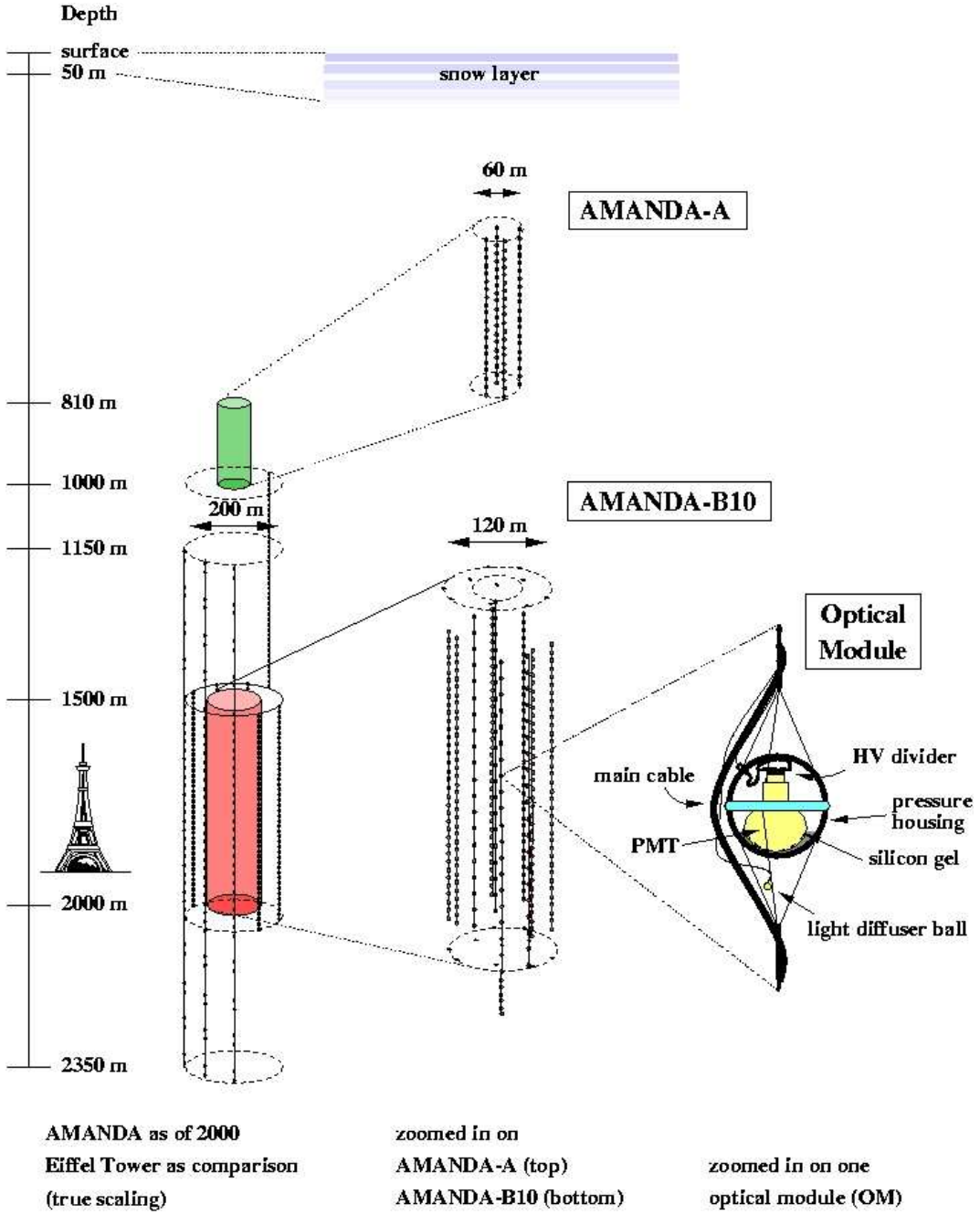

Figure 4.1: On the left: the AMANDA detector since 2000. On the right, a scheme of an AMANDA OM is displayed consisting of an PMT enclosed into a glass sphere. The optical connection from the glass sphere to the PMT is guaranteed by the optical gel [C+02].

For the inner 10 strings, the PMT signal is conducted to the surface by coaxial cables or by twisted pair cables. The electric dispersion in the cables results in a widening of the PMT pulses from a duration of about 20 ns at the PMT to 200 ns at

the surface [A+00]. Hence, individual arrival times of many photons arriving within that time interval cannot be resolved. In order to improve the time resolution, the 9 strings forming the outer ring are equipped with a readout by optical fibers. The PMT signal is coupled to the optical fibers, transmitted to the surface and reconverted into electric pulses at the surface. With the optical readout, pulses can be separated if the photon arrival times differ by more than 20 ns. As backup, the electric readout via twisted pair cables is available for these strings.

4.2 Trigger and Data Acquisition

The AMANDA trigger identifies time coincidences of photons arriving at different OMs of AMANDA. With this trigger principle any charged high energy particle emitting Cherenkov light is registered.

If a photon gets absorbed at the PMT cathode, the induced photo electron gets amplified by the PMT. In order to separate photons from PMT noise, for each PMT a threshold is defined. If the voltage exceeds the threshold, the PMT signal is written out. The recorded signal information is called a hit consisting of the begin (leading edge) and end (trailing edge) of the time interval, where the voltage exceeds the threshold. These times are measured by Time to Digital Converters (TDCs).

If a time coincidence of many PMT hits is found, it is likely to be induced by a high energy particle, which can be reconstructed later. The used variable is M defined as the number of OMs which have at least one hit within a time window of 2.5 μs. If this multiplicity exceeds an adjustable threshold, normally set to $M = 24$ for AMANDA-II, the trigger condition is fulfilled and an event containing PMT hits in a time window of 34.13 μs is written out.

The data acquisition (DAQ) of AMANDA can register up to 8 hits from each OM within the same event. Additionally, for each OM, the value of the highest amplitude is recorded with peak-sensing Analog to Digital Converters (pADCs). The value of the pADC corresponds to the PMT amplitude and thus it indicates the number of photons reaching the OM at the same time. The readout process of the ADCs and TDCs takes, depending on the size of the events, up to 2.2 ms [Sch02]. In this time, no further event can be detected. With the $M = 24$ trigger condition, the readout process results in a dead time at the level of about 17% of the total time for the AMANDA detector.

An upgrade of the AMANDA DAQ, the TWR system [Wag04] was installed additionally in the years $2002-2005$. The TWR system is based on Transient Waveform Recorders (TWRs), which are Flash Analog to Digital Converters (FADCs) sampling the PMT signal in intervals of 10 ns. A feature extraction algorithm reduces the data rate by deleting the parts of the waveform without pulses. PMT pulses are recorded by the TWR system in a time window of 10.24 μs.

With the TWR system, the restriction to 8 pulses does not exist anymore, the amplitude of all pulses is available and the resolution of multi photoelectron pulses is improved by considering the waveform information. Since the TWR system is operating nearly without dead time, the trigger condition for the TWR system could be lowered in 2004 to $M = 18$. In 2005, a special software trigger was installed [M$^+$05a]. The software trigger searches for local coincidences in order to separate particle induced events from uncorrelated noise for those events with $12 \leq M < 18$.

4.2.1 Event signatures

Most of the events triggered by AMANDA are caused by atmospheric muons generated in charged CR induced air showers (see Chapter 2). Muons produced in charged current (CC) interactions of ν_μ can be separated from atmospheric muons by taking into account directional and energy information. The Earth serves as a shield so that upgoing muons must be ν_μ induced. The lower AMANDA threshold for ν_μ-induced events is around 50 GeV. As shown in Fig. 4.2, the transparency of the Earth for neutrinos decreases with energy. At PeV energies, the Earth becomes opaque for ν_μ. Thus, for energies below a few PeV, AMANDA's field of view for ν_μ is restricted to the Northern Sky. At higher energies, the search for downgoing ν_μ

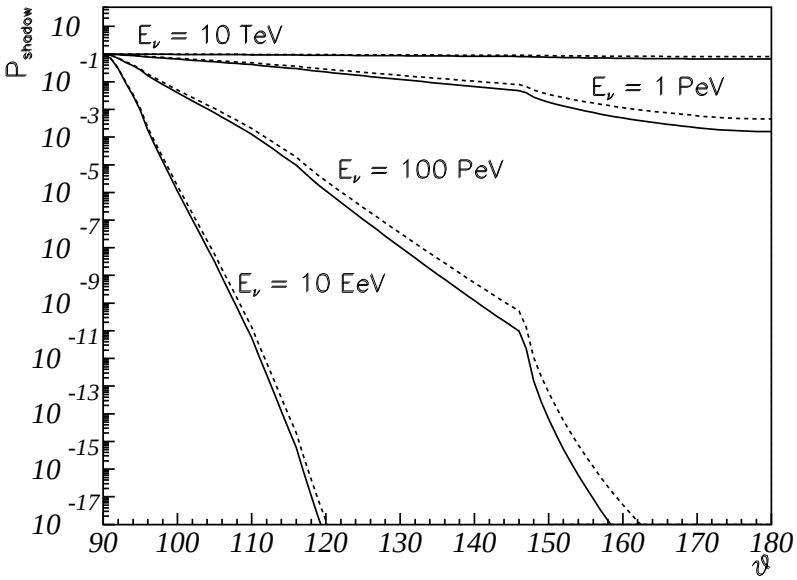

Figure 4.2: The shadow factor P_{shadow} for ν_μ (solid line) and $\bar{\nu}_\mu$ (dashed line) when traversing the Earth describes the probability that a neutrino does not get absorbed by the Earth [Bec04].

induced events is possible since the background of atmospheric muons falls steeply with energy. With help of the long lever arm of the muon tracks, an angular resolution of better than 3° has been achieved in AMANDA, depending on the declination angle and on the strength of quality cuts.

The energy losses of muons in the ice consist of an almost energy independent part due to ionization and of energy-dependent stochastic losses caused by radiative processes. The effective energy loss is parameterized as dE/dx = a + bE, where $a/b \approx 600$ GeV [Gee02]. Thus, for energies $E > 600$ GeV, the amount of Cherenkov light deposited in the detector turns out to be proportional to the energy and allows for energy reconstruction.

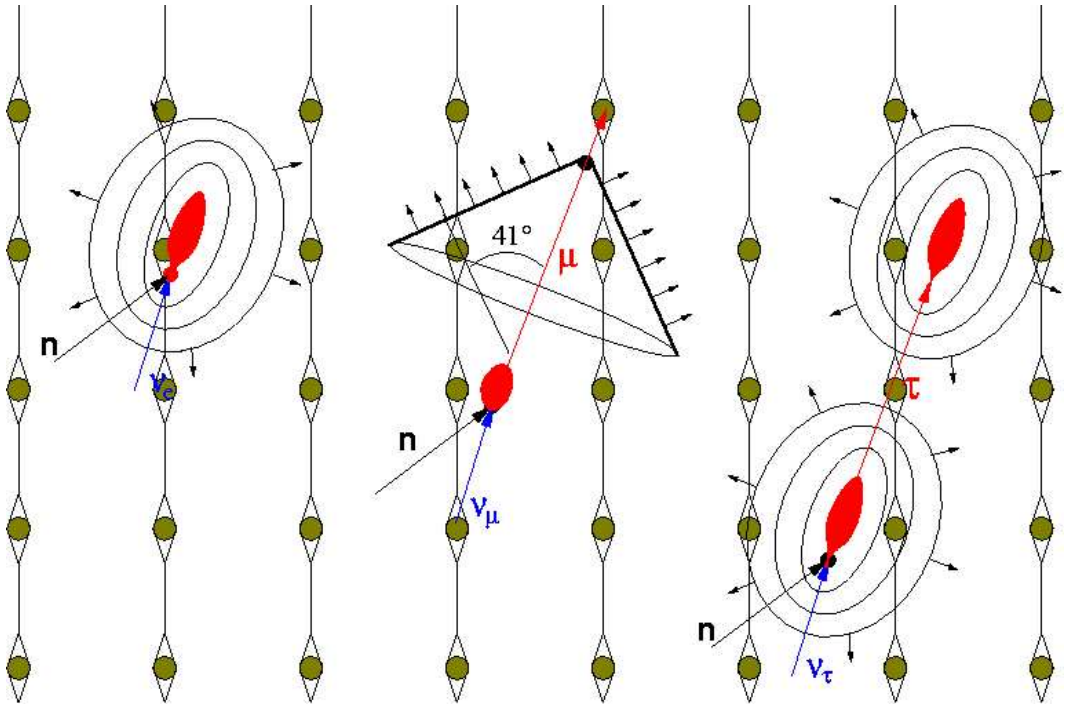

Figure 4.3: Neutrino detection principles in Cherenkov detectors: electron neutrinos are detected by the Cherenkov light produced by cascading secondary particles. Muon neutrinos are detected by the Cherenkov light emitted by the muon generated in the interaction of a muon neutrino. Tau neutrinos are detected by Cherenkov light emitted by cascading secondary particles. Depending on energy, the cascade of the charged current interaction can be separated from the cascade caused by the tau decay.

Other ν flavors can be detected by the light produced by hadronic and electromagnetic cascades, if the charged current interaction takes place within the detector. For ν_τ, a second cascade develops at the decay vertex of the generated τ. If the energy is sufficiently high, the two cascades can be separated in space. None of these double bang events has been observed with AMANDA yet.

For cascades, the event rates are much lower due to the smaller interaction volume. The lack of a long lever arm results in an angular resolution for cascades only at about 30°. The better angular resolution for the ν_μ channel and the larger event rates favor this channel for analyses of astrophysical sources.

The event signatures of all neutrino flavors are visualized in Fig. 4.3.

4.3 Ice properties

The understanding of the detector medium is the basis for any physical interpretation of light pulses recorded by the detector. In order to study ice parameters, light is emitted from steady and pulsed sources within the AMANDA detector. The recorded response of the AMANDA OMs allows for the reconstruction of absorption and scattering coefficients. It turns out that the antarctic ice sheet is not a homogeneous medium. The scattering coefficient has been found to vary by a factor of 7 as a function of depth in the ice, the absorption coefficient varies by a factor of three [A$^+$05b]. Figure 4.4 shows the scattering length and the absorption length as measured by AMANDA in the antarctic ice sheet as a function of depth. The changing ice properties are the result of a variable concentration of dust particles in the ice as the result of climate changes in the past. Additionally, the number of air bubbles in the ice decreases with the depth in ice. While at lower depths, the scattering on bubbles disfavors a detector there, at a depth of more than 1350 m, the bubbles condensate into air-hydrates and no scattering on bubbles takes place.

4.4 Detector simulation - The Monte Carlo chain

All relevant types of particle induced events in the AMANDA telescope are simulated by a chain of Monte Carlo simulation programs. First, events of a certain particle type (atmospheric muons, atmospheric neutrinos, neutrinos from astrophysical sources) are generated. Then the propagation of the generated particles through the atmosphere and/or the Earth is simulated. Finally, the response of AMANDA is simulated.

The event generator NUSIM [Hil96] generates muon neutrinos according to an E^γ spectrum. Either an isotropic angular distribution or point sources can be simulated. The energy spectrum is adjusted by changing the weights of the individual events. In addition to isotropic power law spectra, the weighting can be done according to predictions of the atmospheric flux [Lip93], including the corresponding zenith dependence.

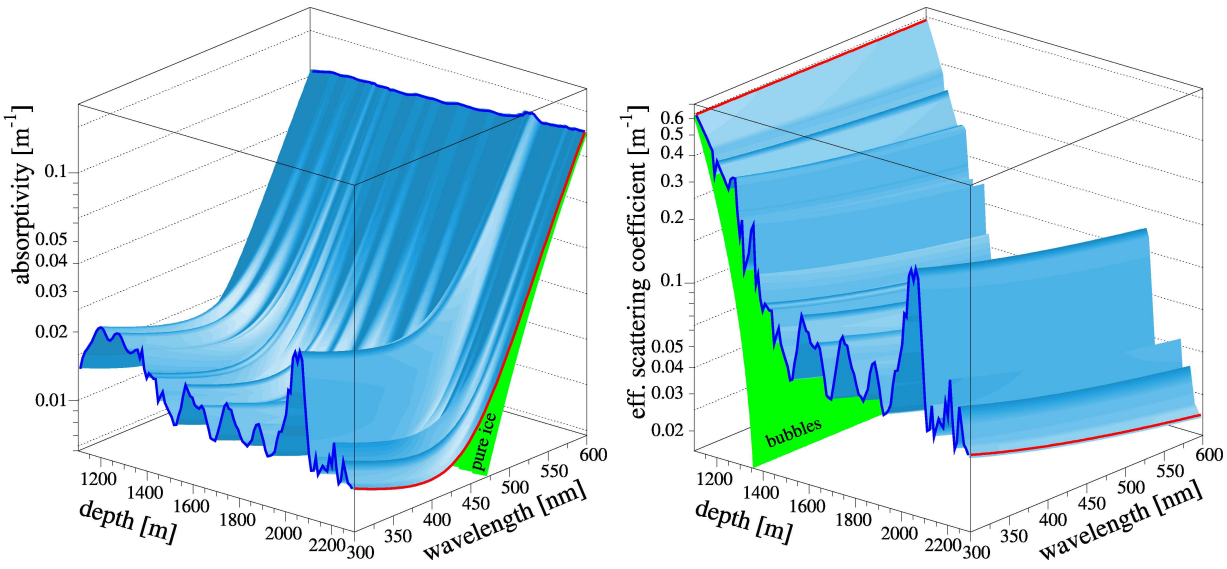

(a) (b)

Figure 4.4: Absorptivity (a) and scattering coefficient (b) in ice as a function of depth and wavelength [A$^+$05b]. The dust layer structure is clearly visible in both plots. The decrease of the scattering length in depths below 1300 m due to bubbles in the ice can be seen in (b). The scattering on bubbles only is indicated by a sheet in that plot.

Atmospheric muons are generated by CORSIKA [H$^+$98]. The code has been modified for the use in AMANDA, including an output of the results in the AMANDA data format (dCORSIKA) [Chi].

Muons generated in air showers or in charged current interactions from neutrinos are propagated through the ice by MMC (Muon Monte Carlo) [RC01, CR04]. Continuous energy losses by ionization are simulated as well as stochastic energy losses by pair production, bremsstrahlung and photonuclear interactions.

The AMANDA detector is simulated by AMASIM [Hun99], including the simulation of photons arriving at the OMs and the simulation of the detector response to these photons, resulting in an event in the same data format as measured AMANDA events. The propagation of individual photons through the ice is not simulated. Instead, the arrival times of photons are simulated according to probability tables for the photon arrival times. These parameterized tables were generated once for a given set of ice properties. The depth-dependent changes of the ice properties are taken into account only partially: the ice parameters at the level of the considered OM are used to propagate the photon the whole way from their emission to the OM.

4.5 Event reconstruction - direction and energy

In AMANDA, the arrival times of the Cherenkov light at the OMs are used to reconstruct muon tracks. Other variables like the total amount of hit OMs turn out to be energy dependent.

4.5.1 Time and amplitude calibration

Before the reconstruction of the triggered events is possible, the measured values have to be converted into time and number of arriving photons at the PMTs.

For the time calibration, two effects have to be considered: the propagation time of the signal from the OM to the AMANDA counting house and the time slewing due to the fixed PMT threshold. The propagation time is taken into account by subtracting a fixed propagation time, t_0, from the measured time at the surface, t_{surf}. For all OMs, t_0 has been measured with laser light. In this measurement, the true arrival times of the photons at the PMT are known. The correction for time slewing is necessary, since the time slewing of the PMT signal depends on the amplitude. This effect is illustrated in Fig. 4.5. An analysis of the arrival times of photons as a function of the measured pADC amplitude, A, for the laser measurements shows, that the time slewing is proportional to $t_{slew} = \alpha/\sqrt{A}$ with the OM dependent calibration constant α.

Finally, the calibrated photon arrival time is given by

$$t_z = t_{surf} - t_0 - t_{slew} \,. \tag{4.3}$$

The achieved time resolution for t_z with this method is in the range of 4 ns − 7 ns, depending on the individual OMs [A+00].

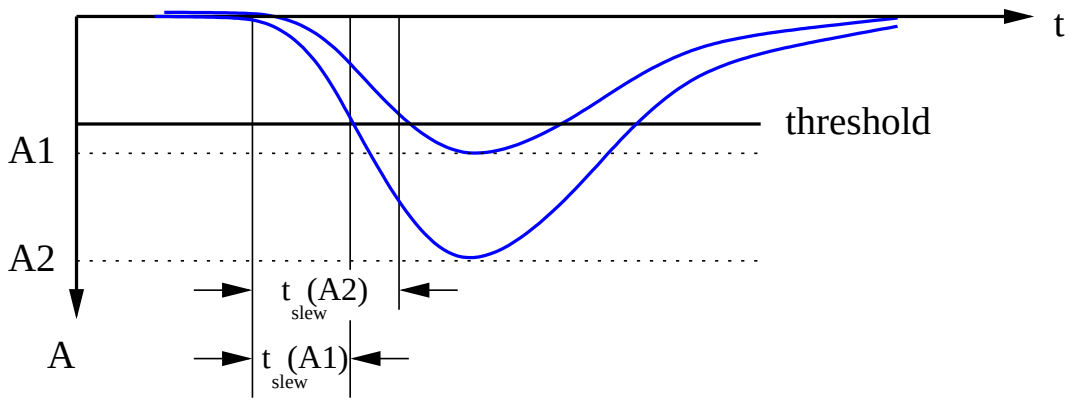

Figure 4.5: Time slewing due to fixed threshold. [Wag04]

The amplitude of the PMT pulses is an approximately linear function of the number of photons which arrive within the pulse duration (20 ns − 200 ns). The most abundant PMT pulses are single photo electron (SPE) pulses, where only one photon was registered in the PMT. Hence, the constant of proportionality, β, can be determined by fitting the most frequent amplitude for each OM. Then, the measured number of photo electrons is given by

$$N_{pe} = \beta \cdot A \tag{4.4}$$

4.5.2 Muon track reconstruction

The arrival time of Cherenkov photons follows a certain probability distribution for the time residual t_{res}, which is defined as the difference between the actual arrival time, t_{hit}, and the arrival time of the unscattered Cherenkov photons, t_{geo},

$$t_{res} = t_{hit} - t_{geo}\,. \tag{4.5}$$

With growing distance from the track, this probability distribution gets wider and the information on the Cherenkov cone from these hits gets less accurate. It turned out, that unscattered photons causing "direct" hits with small time residuals are essential for the reconstruction quality.

The reconstruction of muon tracks usually is done in two steps:

- A fast first guess algorithm is applied to all events.
- A slower maximum likelihood fit, aiming for best possible angular resolution, is applied to events fulfilling a cut on the result of the first guess.

The first guess algorithm is a pattern recognition algorithm searching for clusters of direct hits close to the assumed particle track.

The maximum likelihood method is a general procedure to estimate a set of unknown parameters, $\mathbf{a}$, from a given set of measured values, $\mathbf{x}$. In case of AMANDA, the unknown parameters are the track parameters (3 coordinates of a point on the track and 2 direction angles). The measured values are the arrival times and the number of photons arriving at the PMTs. The likelihood function, $L(x)$, is defined by

$$L(x) = \Pi_i p(x_i|\mathbf{a})\,, \tag{4.6}$$

where $p(x_i|\mathbf{a})$ is the probability to observe the measured value x_i for a given set of parameters $\mathbf{a}$ [A$^+$04b]. In the AMANDA track reconstruction, $L(x)$ is defined as the time likelihood, i.e., $p(x_i|\mathbf{a})$ is the probability to observe a photon hit at a certain time for the track parameters $\mathbf{a}$. The probability distribution of the arrival times

as a function of the distance is obtained by a fit to simulated events. The optimum likelihood reconstruction requires to be initialized with a rough estimate of the track provided by the first guess. The reconstruction in AMANDA is done by minimizing $-\log(L)$ with the software program recoos in the SiEGMuND [H$^+$01] package, or, more recently, with the SIEGLINDE software package [Boe05].

The quality of the likelihood fit is improved by applying the iterative likelihood fit. Since the optimization may converge into a local maximum, the optimization is repeated, initialized with the optimum parameters from the last iteration modified by a small random value. If a different maximum with a higher likelihood value is obtained, the track reconstruction gets improved by the iteration step. In the AMANDA data analysis, typically 16 or 64 iterations are used. It turned out that the best reconstruction performance is reached, if only the first hit in each OM is used for the reconstruction. For an overview on track reconstruction techniques see [A$^+$04b].

4.5.3 Energy reconstruction

The energy dependent light deposit in the detector allows for energy reconstruction. With the help of the AMANDA Monte Carlo (MC) simulation chain, some energy dependent variables have been identified, e.g., the number of hit OMs. However, due to the indirect measurement and due to stochastic fluctuations of the energy losses, only an energy resolution of 0.5 in log E has been achieved. While this uncertainties are too large to infer detailed information about individual events, the accuracy is sufficient to derive the energy spectrum from the distribution of energy correlated variables. In order to obtain the energy spectrum, the method of regularized unfolding [Blo84] is used for the correction of bin to bin fluctuations and of limited detector acceptance. The unfolding software is restricted to three input variables. Since more energy correlated variables have been identified, the information of several variables has been summarized by a neural net into a parameter proportional to energy. The parameter calculated by the neural net and two further energy dependent variables of all events are used as input variables to unfold the ν_μ energy spectrum [G$^+$03, M$^+$05b]. The unfolded spectrum derived from one year of AMANDA-II data is displayed in Fig. 4.6. No deviation from the expectation of the conventional atmospheric neutrino flux [H$^+$95, VZ80] has been found. Thus, the muon neutrino sample collected by AMANDA is strongly dominated by atmospheric neutrinos. With help of the probability density function inferred by a large number of Monte Carlo experiments, an upper limit on the extraterrestrial neutrino flux at energies between 100 TeV and 300 TeV [M$^+$05b] is determined preliminarily to

$$E^2\Phi < 2.6 \cdot 10^{-7}\ \mathrm{GeV\ cm^{-2}\ s^{-1}\ sr^{-1}}\,. \tag{4.7}$$

This limit is represented in Fig. 4.6 by a horizontal line above the corresponding energy bin.

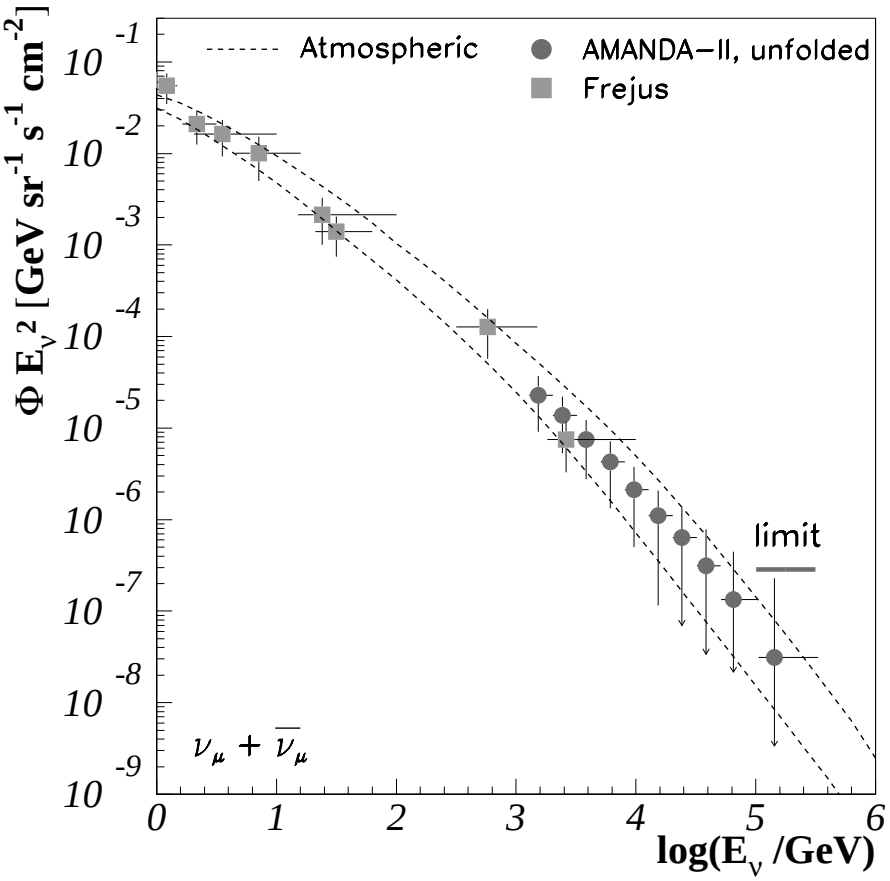

Figure 4.6: Unfolded neutrino ($\nu_\mu + \bar{\nu}_\mu$) energy spectrum as measured by AMANDA II [M$^+$05b] and Fréjus [DR$^+$95]. The dashed lines correspond to the expectation of the conventional atmospheric neutrino flux in horizontal (upper line) and vertical direction (lower line) [H$^+$95, VZ80]. The measured data points are in agreement with the predicted spectrum. An upper limit on the E^{-2} flux based on AMANDA-II measurements is marked by the solid line above the highest energy bin at 100 TeV to 300 TeV [M$^+$05b].

5

Analysis of AGN classes as neutrino point source candidates with AMANDA

This chapter begins with a review of the analysis of data collected by AMANDA for astrophysical sources. Then the analysis methods are adapted for the analysis of samples of generic sources in a source stacking analysis. This technique is applied to the samples of generic AGN classes which have been derived in Chapter 3. The results of the analysis are discussed.

5.1 The search for astrophysical neutrino sources with AMANDA

The search for astrophysical neutrino sources with AMANDA is based on the search for a statistically significant excess of measured neutrino events from a certain direction over the background of atmospheric neutrinos. The angular resolution of AMANDA is given by a median angle of $2^\circ - 2.5^\circ$ between true and reconstructed track if selecting well-reconstructed tracks [A$^+$04b]. Therefore, any considered candidates for astrophysical sources are point-like[1]. Thus, the extension of the candidate sources has not to be considered and the sources can be treated as point-like. This is done in a *point source analysis*. In the following, *point source analysis* will be used as a synonym for the analysis of a neutrino event sample for the flux from individual astrophysical sources.

Two different coordinate systems are used to describe the reconstructed arrival directions of neutrinos. At a technical level, the detector coordinates are used, the

[1] The angular diameter of the Moon and the Sun is about 0.5°.

zenith angle, Θ, and the azimuth angle, Φ. Additionally, astronomical coordinates are used, the right ascension (RA or α) and the declination (δ or DEC). Due to the unique location of AMANDA, Θ and δ can easily be converted,

$$\delta = \Theta - 90^\circ \,. \tag{5.1}$$

The conversion from Φ into α is done with the AMANDA reconstruction software [H$^+$01]. It corresponds to a correction for the rotation of the Earth.

Due to the location of AMANDA at the geographic South Pole, the background of atmospheric neutrinos is symmetric in RA. This allows to calculate the expected number of background events in a search bin on-source, n_{bg}, from the observed number of events off-source in the same zenith band, n_{zb}. The zenith band is defined as the part of the sphere enclosed by δ_{min} and δ_{max}. The definition of the search bins and the zenith band between δ_{min} and δ_{max} is illustrated in Fig. 5.1. The background is given by

$$n_{bg} = n_{zb} \cdot A_{bin}/A_{zb} \,, \tag{5.2}$$

where the space angle of a circular search bin with bin radius r_{bin} is given by

$$A_{bin} = 2\pi \left(1 - \cos(r_{bin})\right) \,, \tag{5.3}$$

and the space angle of the zenith band, which is defined as the range of the declination δ between δ_{min} and δ_{max}, is given by

$$A_{zb} = 2\pi \left(\sin(\delta_{min}) - \sin(\delta_{max})\right) \,. \tag{5.4}$$

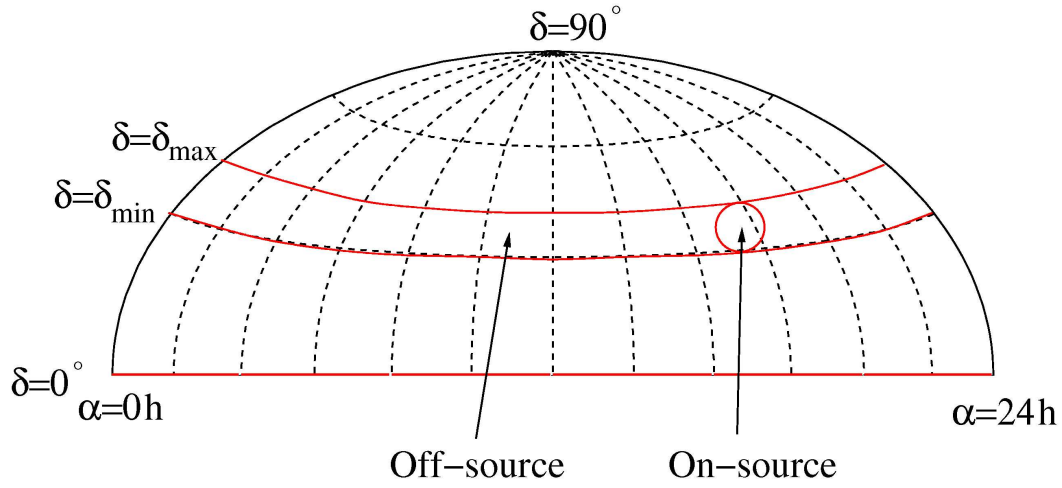

Figure 5.1: In the AMANDA point source analysis, the number of observed neutrino events on-source is compared with the background expectation off-source. The on-source events are located in a circular search bin around the candidate source. The corresponding off-source region is defined as the zenith range enclosed by δ_{min} and δ_{max}.

For a point source analysis, a sample of neutrino events has to be extracted from the collected data. The rejection of the background of atmospheric muons, which are at trigger level 10^6 times more abundant than neutrinos, is of central importance. A small fraction of atmospheric muons (usually $\sim 10^{-3}$) is misreconstructed as upgoing, however still dominant over neutrino induced events. Quality criteria on the reconstructed track are used to separate neutrino induced events from misreconstructed atmospheric muons. The strength of the cuts determines the purity of the neutrino sample and the signal efficiency. It is optimized by requiring maximum sensitivity to neutrino point sources.

This optimization has to be done according to the strict blindness principle the AMANDA collaboration has given itself, i.e., no signal is evaluated until all analysis parameters are fixed. Any optimization of analysis parameters has to be done on simulated or randomized data sets. The blindness principle ensures a statistically correct analysis and any bias of unknown trial factors is excluded. In case of a point source analysis, the blindness is ensured by considering only data sets with randomized RA ("scrambled data") or MC simulations in the optimization of the analysis parameters. A comparison of MC and measured data is possible for scrambled data, providing an important check of the understanding of AMANDA. In the resulting optimum event samples, the large majority of the events is given by atmospheric neutrinos, while a small contamination by misreconstructed atmospheric muons is expected, typically a few percent.

5.2 The analysis of generic source classes: Source stacking

With the AMANDA neutrino telescope, several point source analyses have been done [Hau04, A$^+$04c, A$^+$05c, A$^+$]. All-sky searches have been performed as well as the analysis of preselected candidate sources. In the all-sky search, any position in a grid of rectangular search bins is evaluated by considering the background expectation from the average number of events in the corresponding zenith range. The list of 33 preselected candidate sources contains AGN, microquasars and SNRs. An average sensitivity of $E^2\Phi = 6 \cdot 10^{-7}$ GeV cm^{-2}s^{-1} has been achieved in the most sensitive analysis based on 807 days of detector lifetime [A$^+$]. No neutrino point source has been detected with this sensitivity.

The sensitivity of AMANDA to generic point sources can be increased by the evaluation of the cumulative signal of several sources, a procedure which is known as source stacking. In a source stacking analysis, the number of on-source and background events is given by the sum of the corresponding values for the individual sources,

$$\begin{aligned} n_{on}^{stack} &= \sum_{i=1}^{N_{src}} n_{on}^{i} - n_{on}^{overlap}, \\ n_{bg}^{stack} &= \sum_{i=1}^{N_{src}} n_{bg}^{i} - n_{bg}^{overlap}. \end{aligned} \tag{5.5}$$

If two sources are so close to each other that the search bins overlap, the events in the overlap region contribute only once to the sum. The background expectation is corrected for the overlap by subtracting the background expectation of the overlap region, $n_{bg}^{overlap}$, which is calculated analogously to Eq. 5.2 replacing A_{bin} by the space angle of the overlap region. Catalogs of generic AGN classes which are suitable for a source stacking analysis are defined in Chapter 3 and ordered according to their photon flux at a certain selection energy. This ordering scheme is motivated by the assumption of a linear correlation between photon flux and neutrino flux, which does not depend on a specific AGN model.

For each catalog, the number of sources to be analyzed, N_{src}, and of the radius of search bins is optimized. The decreasing relative background fluctuations ($\propto 1/\sqrt{N_{src}}$ if Gaussian statistics are applied) compete with the smaller flux per source if including also weaker sources. The detector parameters of AMANDA enter the optimization in several ways. The background event rate has to be considered in the choice of the statistical method to be applied. The angular resolution of the detector determines the size of search bins. Thus, it determines the maximum number of sources which can be included before a significant fraction of the sky is covered with search bins.

The selection of candidate sources on the Northern Sky with $\delta > 10^{\circ}$ is done without any consideration of the directional information from the data sets to be analyzed. This ensures a statistically correct analysis without a posteriori trial factors, which cannot be estimated correctly. In this way, the AMANDA blindness principle is taken into account for the source stacking analysis.

Two different data sets collected by AMANDA are considered for this analysis. First, the source stacking method is illustrated with a data set collected by AMANDA in the year 2000. Then, the method is applied to a second data set which provides greater sensitivity by using data from various years and by making use of improved reconstruction methods. Data from the TWR system (see Chapter 4) have not been used for the analysis, since the original DAQ system currently provides greater

sensitivity due to its longer operation time. The optimization of the parameters of the stacking analysis is done for both data sets individually.

5.3 The analysis of a data set collected by AMANDA in 2000

The presented catalogs of generic AGN classes are analyzed for a cumulative neutrino flux considering a data set collected by AMANDA in the year 2000 between February, 13th and November, 5th. The selection of events for the analysis was optimized for best sensitivity to single point sources [Hau04, A$^+$04c]. After excluding low quality runs and a correction for dead-time (at a level of $\sim 17\%$), the data set corresponds to a detector lifetime of 197 days [Hau04]. Modules which have a very high noise rate for more of 3% of the runs are excluded from the analysis. The same is done for "dead" modules, which have very low hit rates in more than 50% of the available runs. Runs are excluded from the analysis, if more than 50 modules show an enhanced noise rate. By this, 3% of the available runs are rejected.

A further hit selection removes hits, which are isolated in time and space and thus unlikely to originate in Cherenkov light from a muon track. Hits with enormously low duration are most probably the result of electronic crosstalk in the cables along the detector strings. Thus, hits with a time over threshold (TOT) of less than 75 ns for channels with electric read out and with less than 5 ns for channels with optical read out are removed. The hit leading edge times are corrected for signal propagation in the cables and for time slewing as a result of a fixed discriminator threshold.

5.3.1 Track reconstruction and event selection

The trigger rate of AMANDA at about 100 Hz is strongly dominated by atmospheric muons generated in CR air showers. A large fraction of these events can be rejected by a fast first guess track reconstruction. Hence, a CPU time intensive full reconstruction is not necessary for all events. With the fast pattern recognition algorithm "DirectWalk" [A$^+$04b], events clearly induced by atmospheric muons are removed. The muon track candidate is identified by maximizing the number of unscattered ("direct") hits near the muon track. This reflects the increasing scattering probability as a function of distance to the track. For the further analysis, only events with the reconstructed zenith angle $\Theta_{DW} > 70^\circ$ are considered for further analysis. This cut rejects 97% of the total experimental data, but it is passed by more than 90% of the neutrino induced events according to simulations.

For the remaining events, an iterative maximum likelihood reconstruction is applied with 16 iterations. All events with a reconstructed zenith angle below 80° are re-

jected. After this cut, only 0.4% of the experimental data are selected, but more than 86% of simulated neutrino events. The cuts on the reconstructed zenith angle are visualized in Fig. 5.2.

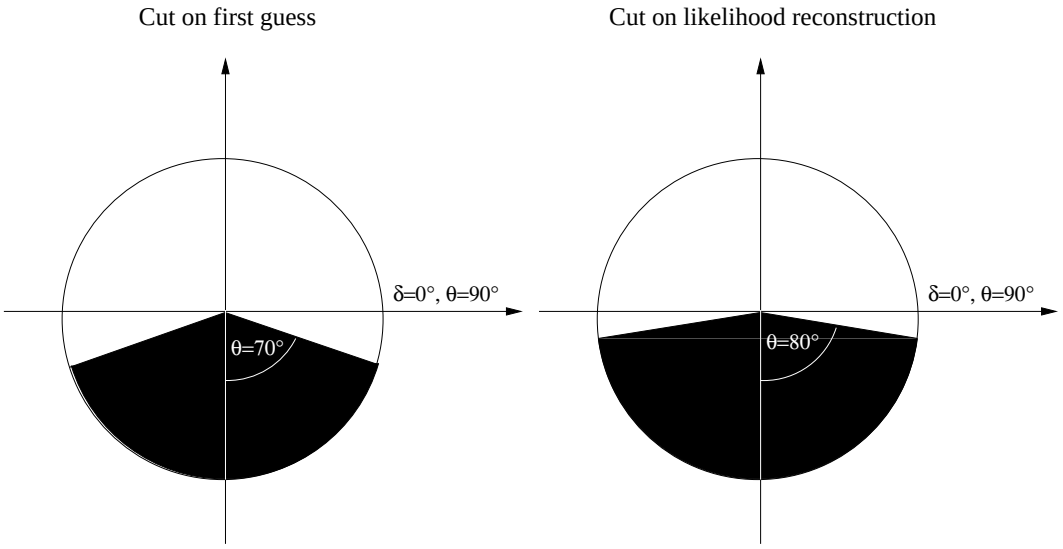

Figure 5.2: Cuts on the reconstructed zenith angle Θ: Events with the reconstructed track in the regions of the sky marked black are rejected after the corresponding reconstruction step.

The remaining event sample is still strongly dominated by misreconstructed atmospheric muons. A large set of quality parameters has been considered to separate these misreconstructed tracks. For all events, a second maximum likelihood reconstruction has been applied, where the reconstructed track is enforced to be downgoing. Bayes' theorem,

$$P(A|B) = \frac{P(B|A)P(A)}{P(B)}\,, \tag{5.6}$$

can be used to consider the prior information that downgoing muons are much more abundant than neutrino induced upgoing events. For this, $P(A|B)$ is identified with the probability that the observed event is really caused by the reconstructed track and $P(B|A)$ is identified with the probability that the reconstructed track would cause the observed event, i.e., the likelihood L. The relative abundance of events caused by downgoing atmospheric muons and of neutrino induced events results in different values of $P(A)$ for upgoing and downgoing tracks [A$^+$04b]. Hence, if the likelihood of the upgoing track is only slightly above the likelihood of the downgoing track, the true track is probably downgoing.

Furthermore, a neural net has been trained with 6 further quality dependent variables. These are the number of direct hits, N_{dir}, the length of the track between

Cut	Pass_ν (MC)	Pass_{Data}
$\Theta_{DW} > 70°$	$> 90\%$	3%
$\Theta_{16LLH} > 80°$	$> 86\%$	0.4%
NN cut	$\sim 30\%$	$5 \cdot 10^{-7}$

Table 5.1: Passing rate of simulated neutrino events (E^{-2} spectrum) and of experimental data after different cuts on the reconstructed tracks.

the first and the last direct hit, L_{dir}, the normalized likelihood of the fit, L^{red}_{track}, the mean angular difference between the results of different reconstruction algorithms, Δ_Ψ, the reduced liklihood difference between a fitted track and a fitted cascade event, $\Delta L = L^{red}_{track} - L^{red}_{csc}$, and the smoothness parameter of the fitted track, $|S|$. The smoothness parameter describes the homogeneity of observed direct hits along the track [A$^+$04b]. If the upgoing track fit is caused by two nearly coincident downgoing muons, the event is expected to have a larger absolute value of S. The teaching function

$$Q_{teach} = \frac{1}{1 + e^{-(\Psi(\text{true,reco})/(1°)-3)}} \tag{5.7}$$

is chosen, where $\Psi(true, reco)$ represents the angle between simulated and reconstructed track. The neural net is trained with this function to identify well reconstructed events with $\Psi(true, reco) < 3°$. The trained neural net is used to calculate the event quality parameter for each event, Q.

Monte Carlo simulations of signal and background are used to determine the optimum cut value on Q and ΔL zenith dependent in steps of $5°$ from $\delta = -5°$ to $\delta = 85°$. The optimum configuration is defined as the configuration resulting in the best average *model rejection factor* (MRF), which is the average upper limit in the case that no signal is present [HR03]. The optimum parameters are listed in [Hau04].

The passing rate of simulated neutrino events and measured data after the presented cuts are summarized in Tab. 5.1. In total, 1557 events fulfill these selection rules. 699 of these events are upgoing ($\delta > 0°$), the others are in the range of $-5° < \delta < 0°$. The arrival directions of these events are shown in Fig. 5.3.

The angular resolution of the data sample is estimated from Monte Carlo simulations. It is described by the Point Spread Function (PSF). The PSF averaged over the considered part of the sky is plotted for various spectral indices of the neutrino flux, $\alpha_\nu = 1, 2$ and 3 in Fig. 5.4. The zenith dependence of the median of the PSF is shown in Fig. 5.5 for an E^{-2} spectrum.

The event sample has been analyzed for a statistically significant excess from a point source. No evidence for a point source has been found, because all observed fluctuations are equivalent to those found in randomized data sets [Hau04, A$^+$04c].

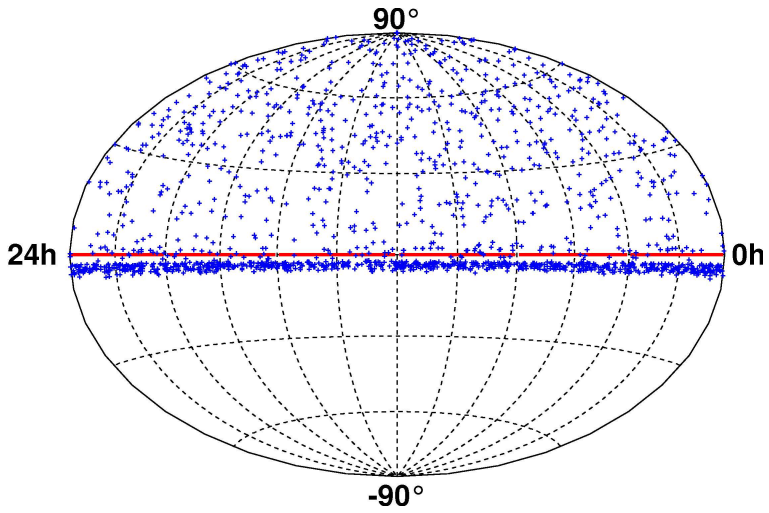

Figure 5.3: Reconstructed arrival direction of 1557 selected events in the year 2000 sample [A$^+$04c]. The events below $\delta = 0°$ are dominated by atmospheric muons.

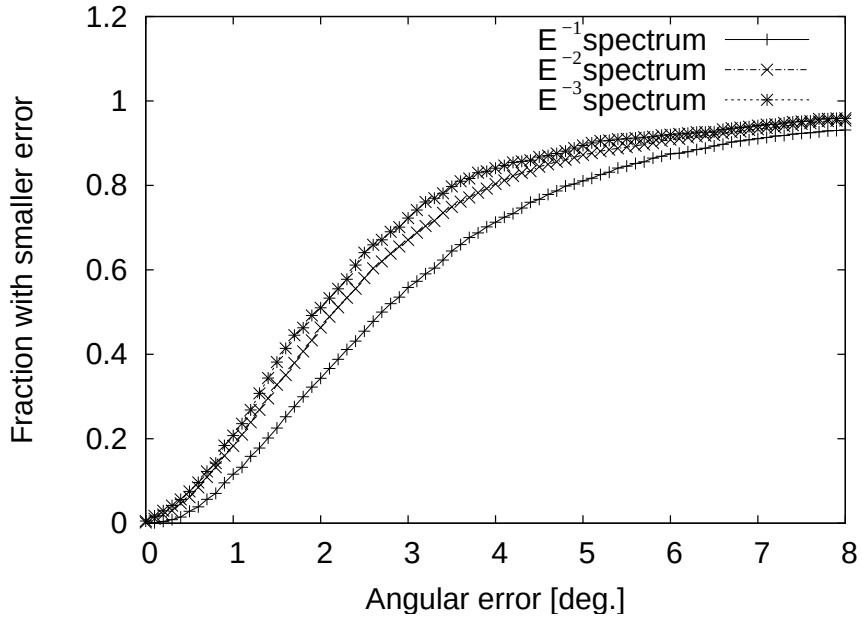

Figure 5.4: Cumulative Point Spread Function of the year 2000 neutrino sample after quality cuts for various spectral indices.

5.3.2 Optimization of the number of sources to include

In order to increase sensitivity, the presented data set is analyzed in this thesis for a cumulative neutrino flux from the generic AGN classes defined in Chapter 3. The different hypotheses on the neutrino flux from the sources in the derived catalogs determine the relative source strength within each class but leave the normalization free. An estimate for a suitable normalization of the signal is obtained by relating

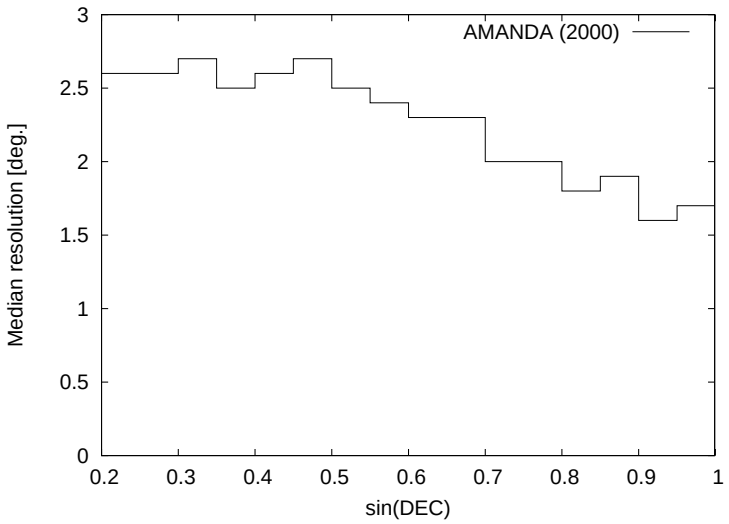

Figure 5.5: Median PSF of AMANDA for data collected in 2000 as a function of $\sin(\delta)$.

the sensitivity of the point source analysis to the hypothetical signal of the strongest source in each sample.

The all-sky search for point sources based on the presented data search corresponds to an AMANDA-II observation of any source in the Northern Sky with 197 days of lifetime. With this analysis, an zenith-averaged sensitivity[2] of $E^2\Phi = 2 \cdot 10^{-7}$ GeV cm^{-2}s^{-1} has been achieved [A$^+$04c]. This sensitivity can be translated into the maximum number of signal events in each bin by the multiplication of the sensitivity with the effective area, the lifetime of the analysis and the bin efficiency. For circular search bins of 3.5° radius, more than three signal neutrinos can be excluded at 90% confidence level. This motivates the choice of the normalization of the neutrino flux for the most intense source. For the expectation value of the number of signal events from that source, S_1, only values of $S_1 \leq 3$ events are considered. Significantly higher signal normalizations would imply that the most intense source would have been visible as an excess in the point source analysis. On the other hand, for smaller values than one for S_1, the expected signal is too faint to expect any notable effect in the source stacking analysis. Hence, the optimization of the number of sources to be included in the stacking analysis is performed for $S_1 = 1, 2, 3$ events (also using the bin efficiency for 3.5°). The number of signal neutrinos from the n^{th} source, S_n, is determined by the applied normalization for S_1 and the assumed linear correlation of the neutrino flux to the measured photon flux. The cumulative signal expectation for the strongest N_{src} sources is given by $S(N_{src}) = \sum_{i=1}^{N_{src}} S_i$. With the chosen normalizations, all values of $S(N_{src})$ of all catalogs agree with the limits of the current diffuse analyses [W$^+$04, A$^+$03b].

[2]The sensitivity is defined as the average upper limit in case of no signal.

Since the sensitivity of the AMANDA-II detector is almost independent of the declination, in the optimization procedure the background is approximated to be constant in the considered declination range. A total amount of 699 events in the year 2000 neutrino sample results in a background of $111.25/sr$ for that year. The expected number of background events per source, BG_1, is obtained by multiplication of this background density with the bin area. The background of the cumulative signal is given by $BG(N_{src}) = N_{src} \cdot BG_1$.

Due to the small numbers of S and BG, Gaussian statistics do not describe the significance accurately. For these small numbers, either Poisson statistics or a likelihood ratio method [LM83] can be applied. In this thesis, Poisson statistics are used to calculate significances from the expectation values of signal and background. The quantity to be optimized is the median significance, which will be reached in 50% of the experiments being performed under the assumed conditions. For a given number of sources N_{src}, the number of expected signal events $S(N_{src})$ and the mean number of expected background events, $BG(N_{src})$ are considered. According to Poisson statistics, the probability to observe at least n events is given by

$$P(n_{obs} > n|S, BG) = \Gamma_I(n, S + BG)\,, \tag{5.8}$$

where Γ_I is the normalized incomplete Gamma function. The median of this distribution is given by the value n_{median} for which $P(n_{obs} > n_{median}) = 0.5$. It is obtained by inverting and resolving this equation for n_{median}. The significance of the observation of n_{median} events is given by the probability under the assumption of pure background. It is given by the cumulative Poisson probability

$$P(n_{obs} > n_{median}|BG) = \Gamma_I(n_{median}, BG)\,. \tag{5.9}$$

The significance in terms of a probability, P, is rescaled to the corresponding number of standard deviations of a Gaussian, s, by inverting

$$\begin{aligned} P &= 1 - \Phi(s) \\ &= \frac{1 - \mathrm{erf}(s/2)}{2}\,, \end{aligned} \tag{5.10}$$

where Φ is the cumulative Gaussian distribution. Finally the median significance in terms of standard deviations is obtained as a function of the number of sources to include. The optimum number of sources, as determined by this median significance procedure, corresponds to the highest value of s.

The same procedure is applied to the size of circular search bins, varying the signal according to the point spread function (PSF) and the background according to the area covered by the search bins. The PSF is evaluated for an E^{-2} spectrum as expected from Fermi acceleration. Since the PSF is not completely independent of the declination, the PSF averaged over all declinations is used.

The optimum number of sources and the optimum bin size depend on each other. Thus, an iterative procedure is applied. First the number of sources is optimized with roughly estimated bin size. Then the bin size is optimized for the given number of sources, and finally, the number of sources is checked again.

The results for the optimum values have been checked by a second procedure which will be called maximum observation probability procedure. A minimum significance s is predefined and the probability to observe at least this significance is optimized. As the expected signal is rather small, a value of 3σ is chosen for s.

Conditions for stacking on the flux distribution

In Sec. 3.6, the flux of the n^{th} source $F(n)$ as a function of the source number n has been considered to evaluate the conditions for a sensitivity improvement by stacking on the source strength distribution. A power law has been used to parameterize $F(n) \propto n^{\alpha}$. For Gaussian statistics, an improvement of the sensitivity is obtained, if $-1.27 < \alpha < -0.5$. The presented optimization scheme based on Poisson statistics and the AMANDA sensitivity is applied to $F(n)$. The maximum sky coverage with search bins has been restricted to 10%. This corresponds for 2.6° search bins to a maximum of 100 sources. With these assumptions, the range for source stacking with AMANDA is given by $-1.1 < \alpha < -0.65$. The smaller range with respect to the general consideration based on Gaussian statistics is caused by taking into account restrictions on the maximum source number caused by the finite size of search bins additionally.

The resulting samples

The presented optimization scheme is applied to the samples of generic AGN. The resulting parameters for year 2000 data are listed in Table 5.2.

In Fig. 5.6, the median significance is plotted as a function of the number of EGRET blazars to be included for different signal normalizations from $S_1 = 1$ to $S_1 = 4$. For the further AGN samples, the median significance as a function of the number of sources to be analyzed is displayed in Appendix D. The highest normalization of $S_1 = 4$ signal neutrinos from the strongest source is unlikely, as it implies a median significance above 3σ for the single source search. Hence, $S_1 = 4$ is not considered for the evaluation of the optimum source number.

For most source classes, an optimum of about 10 sources is found. With one exception, the source stacking analysis is more sensitive in testing the corresponding hypotheses than the point source analysis of single sources. A second sample shows always increasing significance, when including further sources. The observed peaks in the further samples are asymmetric: if more sources than the optimum num-

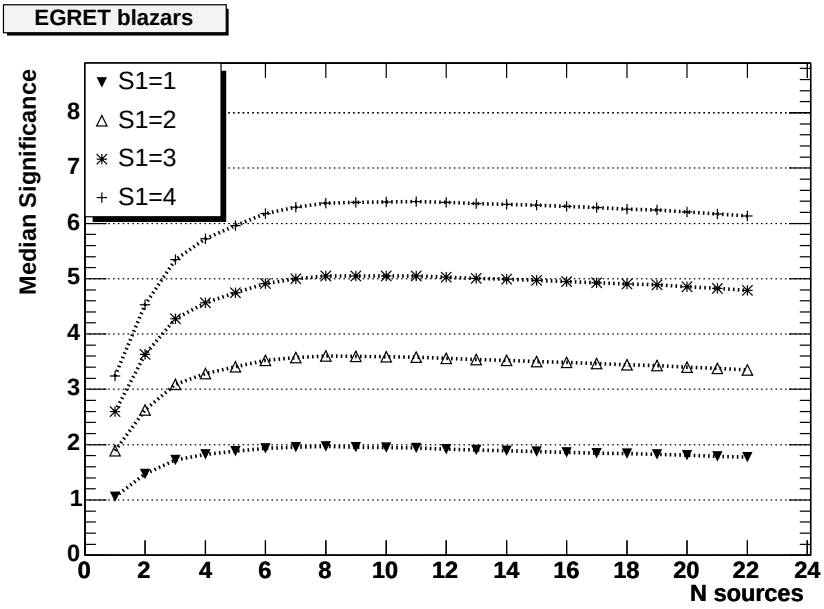

Figure 5.6: Median significance as expected under the considered hypothesis as a function of the number of GeV blazars to be stacked. The expectation value of the number of signal events for the strongest source is represented by $S1$. The highest value of the median significance corresponds to the optimum number of sources.

ber are included, the expected significances decrease only slowly. In contrast the significance falls quite steeply if fewer sources are included.

The exceptions are found for FR-I and for FR-II radio galaxies. As there is a luminous FR-I galaxy in the cosmological neighborhood of the Milky Way, M87, the FR-I flux would be strongly dominated by M87. The HEGRA measurement of TeV photons (with a significance of 4.1σ) from this misaligned blazar [A$^+$03a], theoretically predicted in [PDR03], also supports the uniqueness of this source. The optimization suggests to analyze the ν flux from that source only. However, a FR-I sample without M87 is analyzed additionally for two reasons. First, there is always the possibility that a single source does not contribute to the neutrino flux due to a reason not considered at selection. Second, in the opposite case, if M87 would be identified as a neutrino point source, the cumulative signal of the other sources contains the information, if the ν flux would be a specific feature of M87 or a general characteristic of FR-I galaxies. Excluding M87, nearly constant values for observation probability and median significance are found for more than 15 sources.

The situation of FR-II galaxies is opposite to that of FR-I galaxies. There are a lot of sources with similar luminosities. Hence, the sensitivity increases monotonically by the inclusion of further sources. Then, the coverage of the sky by search bins reaches a significant fraction of the sky and the techniques of point source analysis become less suitable to analyze the signal. In the end, the arrival direction will

not be suitable to identify signal neutrinos. If the energy spectrum of the signal differs from the atmospheric background, diffuse techniques searching for global excess of high energy neutrinos are more sensitive to FR-II galaxies. However, since point source analyses and diffuse analyses are using complementary techniques and a point source analysis can give information about the origin of the excess, a source stacking analysis of FR-II galaxies is also useful. Since the optimization fails, the most suitable value for the number of FR-II sources to be analyzed has to be defined. For it, a local saddle point at 17 sources is used to introduce the cutoff. Above this point, the sensitivity grows only marginally if further sources are included.

These exceptions are expected, since the fit power law indeces α (with $F(n) \propto n^{\alpha}$), $\alpha_{FR-I} = -4.1$ and $\alpha_{FR-II} = -0.6$ for FR-I and FR-II radio galaxies, are not in the interval $-1.1 < \alpha < -0.65$ where source stacking provides an improvement in sensitivity for the current data set.

The check of the results with the maximum observation probability procedure results in deviations between the two procedures which are within the corresponding uncertainties of the determination of the optimum.

The optimum bin size has been found between 2.6° for the unidentified GeV sources and 3.0° for M87 only. As expected [A$^+$93], the bin size decreases with the size of the sample.

source class	N_{src}^{MS}	N_{src}^{DP}	**listed in**	**Bin size [deg.]**
IR blazars (IRAS)	11^{+0}_{-1}	11^{+0}_{-1}	Table C.1	2.8 ± 0.2
keV blazars (ROSAT)	8 ± 1	9 ± 1	Table C.2	2.8 ± 0.2
keV blazars (HEAO-A)	3 ± 0	3 ± 0	Table C.3	2.9 ± 0.2
GeV blazars	8 ± 1	9 ± 1	Table C.4	2.8 ± 0.2
unidentified GeV sources	22 ± 5	20 ± 5	Table C.5	2.6 ± 0.2
TeV blazars	5*	5*	Table C.6	2.8 ± 0.2
GPS and CSS	8 ± 1	8 ± 2	Table C.7	2.8 ± 0.2
FR-I radio galaxies	1 ± 0	1 ± 0	Table C.8	3.0 ± 0.2
FR-I without M87	20^{+3}_{-5}	19 ± 4	Table C.8	2.6 ± 0.2
FR-II radio galaxies	122	17^{+105}_{-5}**	Table C.9	2.6 ± 0.2***
Radio-weak quasars	11^{+1}_{-3}	11^{+1}_{-3}	Table C.10	2.8 ± 0.2

Table 5.2: Resulting parameters for the source stacking analysis.
N_{src}^{MS} and N_{src}^{DP} stand for the optimum number of sources determined with the median significance procedure and, respectively, the maximum observation probability procedure.
* All sources included without optimization, see above .
** Only a saddle point. The observation probability increases again, when including all sources (→ diffuse analysis). See Sec. 5.3.2.
*** Bin size evaluated for 17 sources.

5.3.3 The results for the year 2000

The sources are selected according to the results of our optimization procedure. Selected sources are listed in the source listings of Table C.4-C.10 in the appendix. In this analysis, only the cumulative result for a source class is evaluated, not the signal for individual sources.

The background for each source is calculated according to Eq. 5.2. If two sources of the same sample are very close to each other, their search bins overlap. The background expectation is corrected for the overlap and events in the overlapping area contribute only once to the cumulative signal.

Poisson statistics are used to calculate the probability of any observed number of on-source events under the assumption of pure background. The correctness of the analysis is tested with two procedures. First, to test the correct evaluation of the significance, a collection of data sets with randomized right ascension is created and the significance of the signal from the stacked sources in these randomized data sets is determined. As expected for randomized data sets, the significance distribution follows a Gaussian with a width of one centered at zero. Additionally, hypothetical source lists with random source positions are evaluated using the original data set. A difference of the significance distribution to that of randomized data sets, which follows a Gaussian (see above), would indicate that the assumption of a background flat in RA is not correct. Also in this case, the observed significance distribution follows the expectation. The significance distribution for both tests is shown in Fig. 5.7.

For none of the considered AGN classes, a statistically significant deviation from the assumption of pure background was found and only upper limits could be calculated. For the calculation of the limits, Feldman-Cousins [FC98] confidence intervals and Poisson statistics are used. The measured event rates, the background expectation and the resulting upper limits in terms of event counts and integral neutrino fluxes above 10 GeV are presented in Table 5.3. The limits do not contain systematic errors estimated to be at the level of 30%. A dedicated analysis of uncertainties in AMANDA is currently in preparation for a multi-year data set. For a better visualization, the limits are plotted in Fig. 5.8. The derived limits on the flux of generic sources are compared with the single source sensitivity for the same data set and for 4 years of data from AMANDA [A^+]. Except for the smallest samples, the limits on generic point sources based on one year of data are below the sensitivity to a single point source achieved with 4 years of AMANDA data.

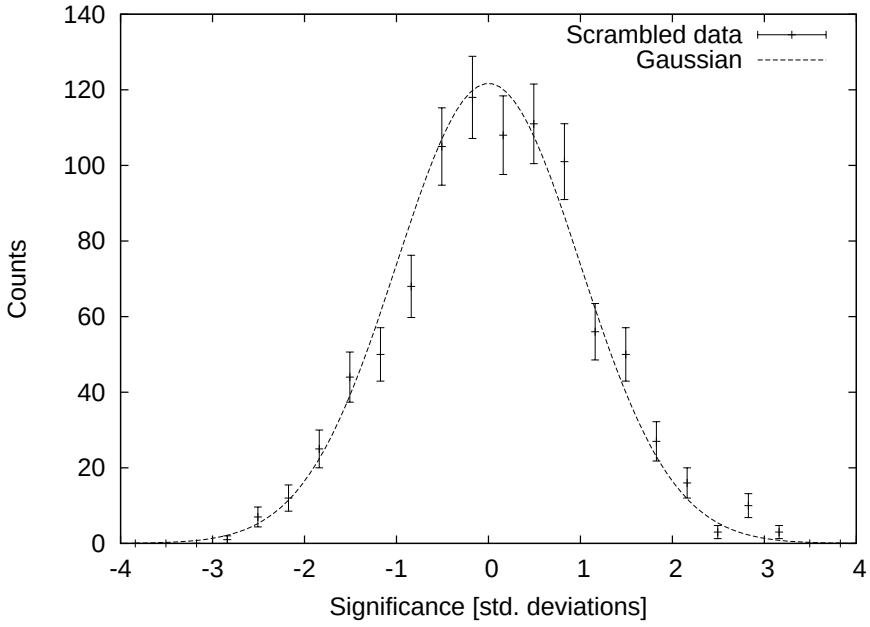

(a)

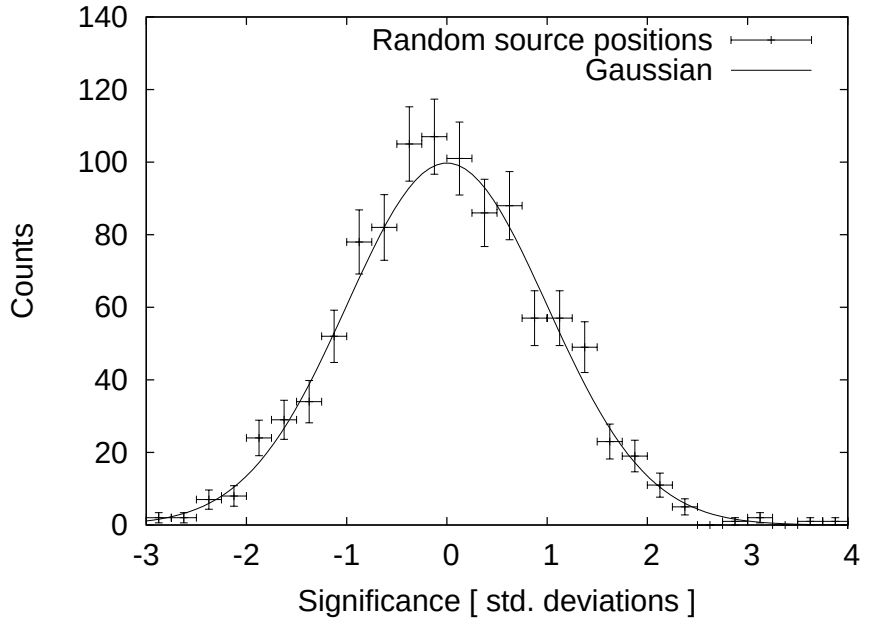

(b)

Figure 5.7: Significance distribution for selected sources in scrambled data sets (a) and for samples of 10 sources with random source positions evaluated with the unscrambled data set (b).

sample	N_{src}	N_ν^{obs}	N_ν^{bg}	n_{lim}	f_{lim}	f_{lim}/src
IR blazars	11	7	10.17	3.0	20	1.8
keV blazars (ROSAT)	8	4	6.68	2.4	16	2
keV blazars (HEAO-A)	3	2	2.47	3.5	28	9
GeV blazars	8	6	5.3	6.3	40	5
unid. GeV sources	22	15	14.9	7.6	56	2.5
TEV blazars	5	4	4.53	4.1	28	5.6
GPS and CSS	8	7	6.14	6.4	43	5.4
FR-I galaxies	1	0	0.56	1.9	13	13
FR-I without M87	20	9	11.50	3.9	27	1.4
FR-II galaxies	17	10	13.42	3.7	27	1.6
radio-weak quasars	11	4	7.55	1.9	13	1.2
single point source sensitivity (1yr)	-	-	-	-	-	20
single point source sensitivity (4yr)	-	-	-	-	-	6

Table 5.3: Results for the year 2000 data: number of sources, measured number of events, the corresponding background and the limits. The limits are 90% C.L upper limits on the differential flux for an E^{-2} spectrum in units of 10^{-8}GeV cm^{-2} s^{-1} and do not include systematic errors. For comparison, the average sensitivity to single point sources is listed for this data set [A$^+$04c] and for a 4 year data set [A$^+$05d].

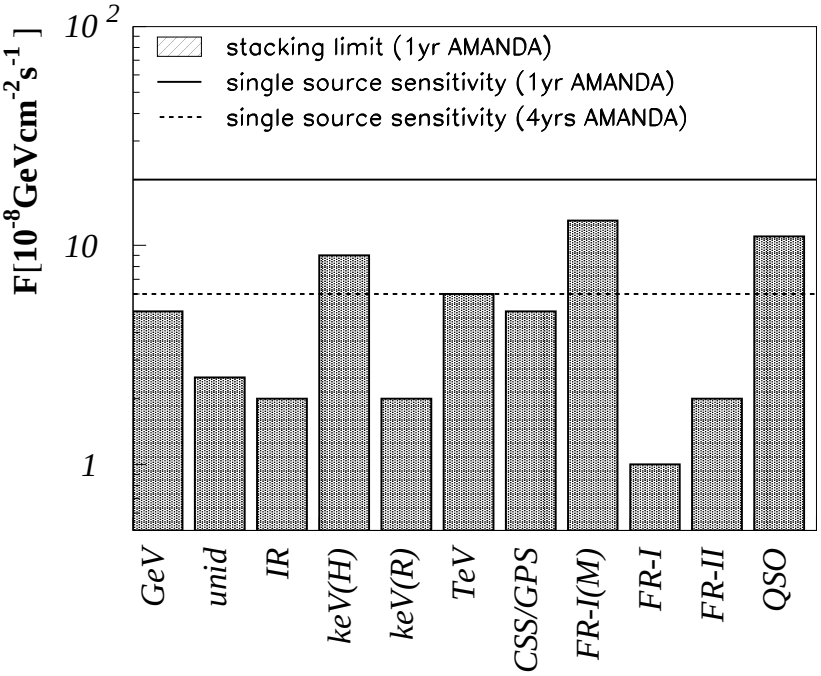

Figure 5.8: Limits on the neutrino flux from an average source in the generic AGN classes using data from the year 2000. The average sensitivity to single point sources is indicated by horizontal lines for this data set [A$^+$04c] a well as for a 4 year data set [A$^+$05d].

5.4 The analysis of a multi-year data set collected in 2000-2003

The source stacking method has been developed in order to increase the sensitivity of AMANDA. It is logical to apply this method to the most sensitive data set. This is currently given by a multi-year data set collected by AMANDA in the years $2000 - 2003$ [A$^+$05d]. The track reconstruction and the event selection has been optimized for greatest sensitivity to single point sources. All data in this sample have been processed according to the same scheme. After the exclusion of periods with detector maintenance work in the austral summer, the rejection of short periods of detector instability and a correction for dead time, the data set corresponds to 807 days of detector lifetime.

5.4.1 Track reconstruction and event selection

With the applied run selection, the data set consists of 7.14 billion events at trigger level. It is strongly dominated by atmospheric muons.

In order to improve the background rejection, two different first guess algorithms for track reconstruction are applied. In addition to the DirectWalk fit [A$^+$04b], which has been applied in the 2000 analysis, JAMS[3] is used as a new pattern recognition algorithm. JAMS searches for clusters of hits on projections orthogonal to the assumed track direction. As in DirectWalk, only hits with a small time residual with respect to the Cherenkov cone are considered.

As in the analysis of the year 2000 data, cuts on the reconstructed zenith angle Θ in the first guess are applied in order to eliminate events clearly induced by atmospheric muons. Only for events with $\Theta_{DW} > 70^\circ$ and $\Theta_{JAMS} > 80^\circ$ a full maximum likelihood reconstruction is performed. While 3.7% of experimental data pass the cut on DirectWalk, only 0.39% remain after the additional cut on the JAMS fit.

Before the maximum likelihood reconstruction is executed, a dedicated hit cleaning for electric cross talk[4] is performed. The hit cleaning is based on maps of channel pairs known for a high level of cross talk [Tab02]. After cross talk cleaning, a 16-fold maximum likelihood reconstruction is performed. A cut on the reconstructed zenith angle, $\Theta_{16LH} > 80^\circ$, is passed only by 0.11% of the original data set.

At this cut level, the data set consists of 7.85 million events and is still dominated by atmospheric muons. Neutrino induced events are identified by imposing track quality requirements. For this, an additional 64-fold likelihood fit is applied, where

[3] JAMS: Just Another Muon Search

[4] The cross talk is the result of electromagnetic induction on the cables of 2 km length in the ice.

Cut	Pass_{Data}
$\Theta_{DW} > 70°$	3.7%
$\Theta_{JAMS} > 80°$	0.39%
$\Theta_{16LLH} > 80°$	0.11%
final cut	$4.17 \cdot 10^{-7}$

Table 5.4: Passing rate of experimental data after different cuts on the reconstructed tracks.

only downgoing tracks are considered. The likelihood ratio L_{down}/L_{up} serves as quality parameter. Furthermore, the homogeneity of hits along the track ("smoothness" variable) and the angular uncertainty of the reconstructed track [Neu04] are considered as quality parameters. As in the previous data set, the final event selection is determined by optimizing the cut values for best sensitivity zenith dependent in 5° steps.

Two different signal spectra have been considered: an E^{-2} spectrum as expected from the mechanism of Fermi acceleration, and a weaker E^{-3} spectrum, as it might be expected from galactic sources. The final parameters are chosen in order to get best performance for both spectra simultaneously.

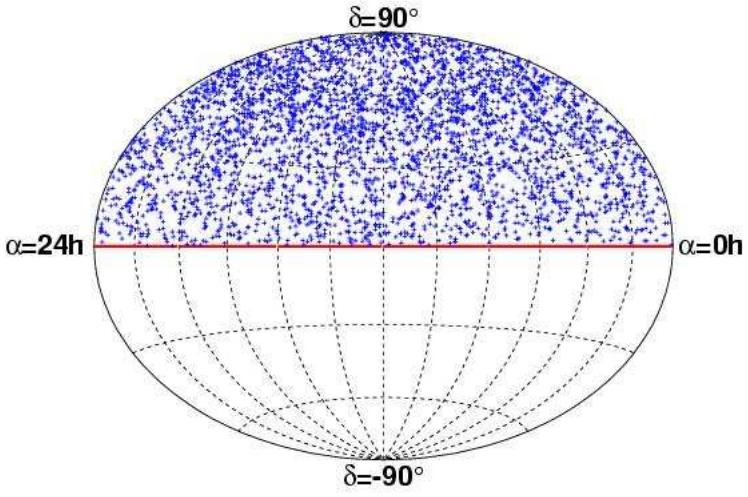

Figure 5.9: Reconstructed arrival direction of 3329 neutrino events in the year 2000-2003 sample [A$^+$].

The optimum cuts of the quality parameters result in an event sample of 3369 events, of which 3329 are upgoing. This is statistically in agreement with the expectation of 3438 events from Monte Carlo simulations of atmospheric neutrinos according to the AMANDA Monte Carlo chain (see Sec. 4.4). The arrival directions of the individual neutrinos are shown in Fig. 5.9.

The Point Spread Function (PSF) for this data set has been determined from the same Monte Carlo simulations by considering the weights of the individual events according to an neutrino energy spectrum proportional to E^{-2}. The resulting PSF is plotted in Fig. 5.10.

5.4.2 Optimization of the source stacking parameters

In order to apply the source stacking method to the multi-year data set, the optimization of the number of sources to be included, N_{src}, and the radius of the search bins, r_{bin}, is repeated for the multi-year data set. As for the year 2000 data set, the median significance is optimized according to the hypothesis of linearly correlated photon and neutrino fluxes. The considered normalization factors are doubled, taking into account the larger amount of data. In comparison with the year 2000 optimization, the procedure is simplified by optimizing directly on a 2-dim parameter space defined by N_{src} and r_{bin}. For nearly all samples, the optimum number of sources for the multi-year data set turns out to be the same as for one year of data. Only for the sample of FR-I galaxies, where M87 is excluded, the optimum number decreases from 20 to 17 sources. In appendix D, the median significance as a function of the number of sources to be stacked is displayed for each considered AGN category.

The optimum bin radius is smaller for the 4 year data set than for the single year data set. In addition to the statistical effect of a decreasing bin size with increasing amount of data [A+93], this is caused by differences in the shape of the considered PSF. For the multi-year data set, the optimum bin radius is in the range of 2.3° for the largest samples and 2.5° for the smallest samples.

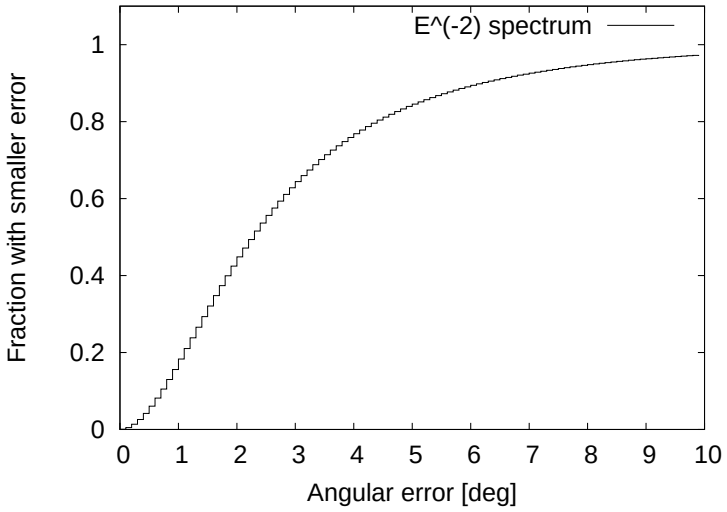

Figure 5.10: Cumulative Point Spread Function after quality cuts for an E^{-2} spectrum in the four year sample.

The distribution of the reconstructed RA is shown in Fig. 5.11 for different declination ranges. No deviation from a flat RA distribution has been found.

5.4.3 The results for the multi-year data set

The source stacking analysis is applied to the presented data set. With an estimate of the number of background events, the significance of any observed excess of on-source events is evaluated after some quality tests on the data sets.

The calculation of the expected number of background events on-source is done the same way as for the data from the year 2000. Additionally, the statistical error of this background expectation is calculated. The number of events in a 5° zenith band is typically at the order of several hundreds. Thus, the statistical error of the background expectation can be calculated according to Gaussian statistics. For an individual source it is given by $\Delta N_{bg} = \sqrt{N_{zb}}$, if N_{zb} events in the zenith band are used for the background calculation. For 5° zenith bands, the relative error of the background expectation is in the range of 10%. Enlarging the zenith range would result in a decrease of the statistic error. However, the systematic error due to the zenith dependent background density would increase.

In the source stacking analysis, the inclusion of further sources reduces the relative statistical error of the background. However, in the case of overlapping zenith bands the same off-source events contribute to the background estimate of several sources. Hence, the error of the background is correlated for these sources. If the background is calculated rather zenith dependent than source dependent, these correlated errors can be avoided:

$$N_{bg}^{stack} = \sum_{src_i} N_{bg}^{src_i} \tag{5.11}$$

$$\approx \sum_{zb_i} N_{bg}^{zb_i}\,, \tag{5.12}$$

where $N_{bg}^{zb_i} = A_{on}^{zb_i}/A_{zb_i} \cdot N_{zb_i}$ and $A_{on}^{zb_i}$ is the solid angle in the considered zenith band covered by on-source search bins. The background estimate according to both expression differs only by about 1%, which is due to the zenith dependent background density. Equation 5.11 is more accurate, since for each source the zenith band is centered at the zenith of that source. Thus, it is used for the calculation of the background expectation. In contrast, Eq. 5.12 ensures independent entries and thus allows to calculate the statistical error of the background according to

$$\Delta N_{bg}^{stack} = \sqrt{\sum_{zb_i} \left(\Delta N_{bg}^{zb_i}\right)^2} \text{ with } \Delta N_{bg}^{zb_i} = \sqrt{N_{zb_i}}\,. \tag{5.13}$$

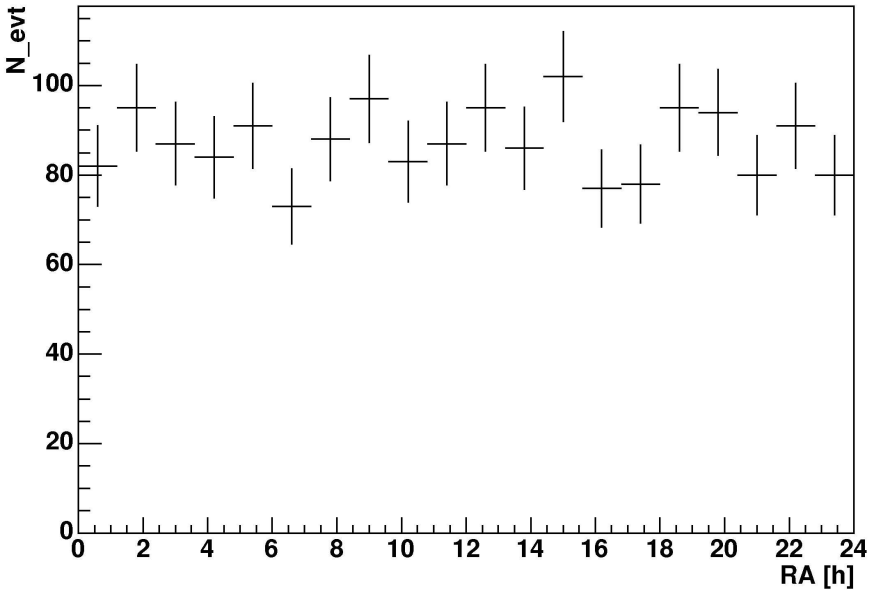

(a)

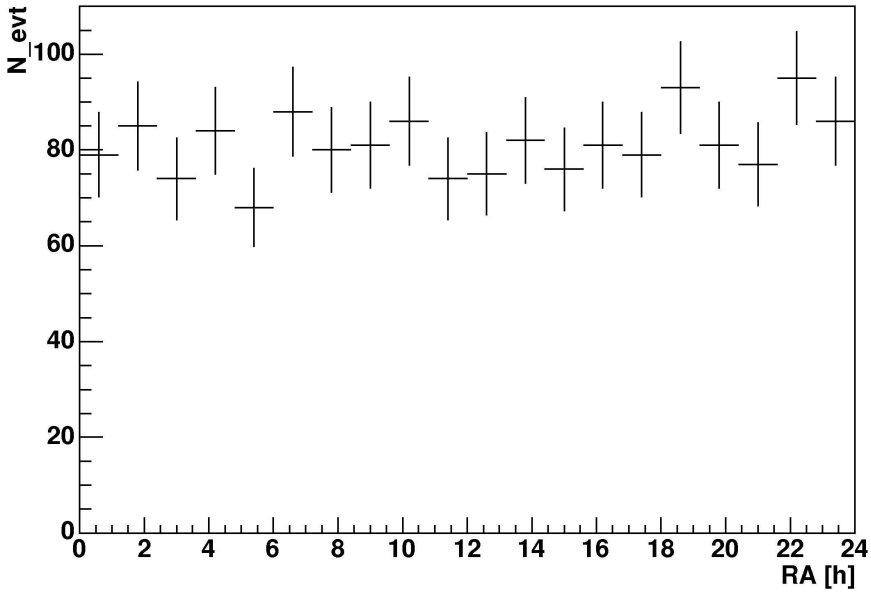

(b)

Figure 5.11: Distribution of the reconstructed RA for events with $\delta < 40°$ (a) and for events with $\delta > 40°$ (b). The distributions are compatible with the expected flat distribution.

Finally, this results in a relative statistical error of the background estimate of typically around 3% for the stacking analysis.

Before an evaluation of the signal from the 11 selected AGN samples, some quality tests of the analysis and the underlying data set are performed. For these tests, 1000 scrambled data sets have been generated, where the RA of all events has been randomized.

The numbers of on-source events in the selected samples of generic AGN are calculated for these data sets. The mean number of on-source events is in agreement with the background expectation and the resulting distribution of on-source counts follows the expectation from Poisson statistics.

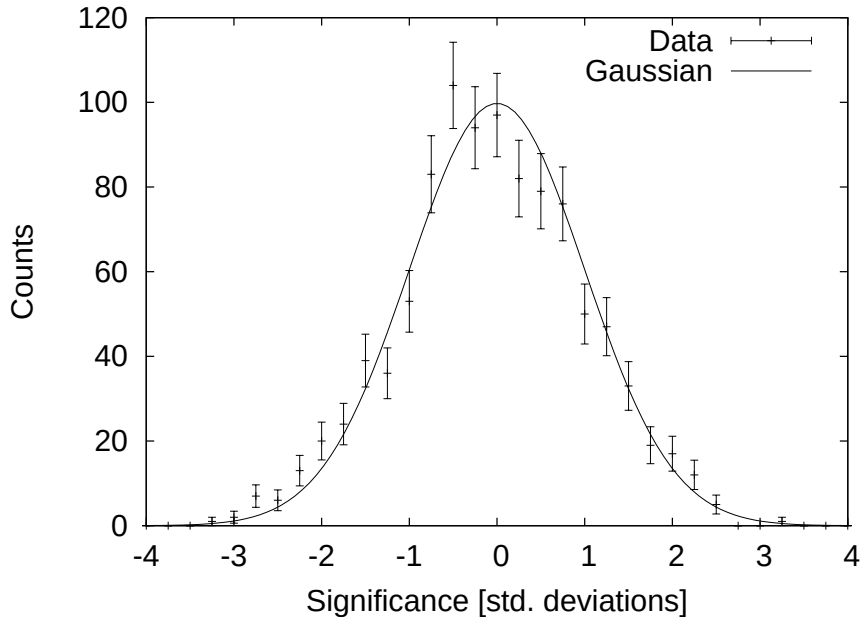

Figure 5.12: Significance distribution for hypothetical source samples of 10 sources at random positions.

Additionally, a large number of samples is analyzed using the final data set (without randomization of RA). Each of these samples contains 10 hypothetical sources with random source positions. The non-detection of extraterrestrial neutrinos up to now suggests a random distribution of the significance. The results of the point source analysis of the considered data set [A$^+$04c] and the unfolded neutrino spectrum [M$^+$05b] suggest that the data sample is strongly dominated by atmospheric neutrinos. If this holds, a difference of the significance distribution to that of randomized data sets, which follows a Gaussian (see above), would indicate that our assumption of a flat background in RA is not correct. Also in this case, the observed significance distribution follows our expectation. The significance distribution for these test data sets is shown in Fig. 5.12.

AGN category	N_{src}	N_ν^{obs}	N_ν^{bg}	$\Delta N_\nu^{bg}/N_\nu^{bg}$	n_{lim}	f_{lim}	f_{lim}/N_{src}
GeV blazars	8	12	20.5	3.0%	1.96	3.2	0.40
unid. GeV sources	22	62	60.1	3.2%	16.4	31.7	1.44
IR blazars	11	30	34.1	2.7%	6.88	12.2	1.12
keV blazars (HEAO-A)	3	7	11.0	5.7%	2.80	5.9	1.97
keV blazars (ROSAT)	8	19	25.8	3.0%	3.64	6.3	0.79
TEV blazars	5	14	18.3	3.2%	3.95	6.9	1.38
GPS and CSS	8	16	22.7	2.9%	3.28	5.7	0.71
FR-I galaxies	1	2	2.5	6.7%	3.44	5.4	5.4
FR-I without M87	17	28	45.0	2.9%	2.34	4.3	0.25
FR-II galaxies	17	58	53.8	2.7%	18.2	34.6	2.04
radio-weak quasars	11	29	32.5	2.6%	6.89	12.5	1.14

Table 5.5: Results of the stacking analysis for each AGN category: the number of included sources is given by N_{src}, the number of expected events is listed under N_ν^{bg} and the number of observed events is given by N_ν^{obs}. The relative statistical error of the background expectation is given by $\Delta N_\nu^{bg}/N_\nu^{bg}$. The limits on the cumulative flux of each sample is listed under f_{lim} in units of 10^{-8}GeV cm^{-2}s^{-1} for the differential flux multiplied by E^2. The flux limits per generic source are given by f_{lim}/N_{src}

The reconstructed arrival directions of the 3329 upgoing neutrinos from the data set and the search bins around the selected sources are plotted in Figs. E.1-E.4 for different AGN classes. The number of observed on-source events and the background expectation of each sample are listed in Tab. 5.5 together with the statistical uncertainties of the background expectation. A comparison of these numbers shows no statistically significant excess for any of the considered AGN categories. Thus, no generic point sources of high energy neutrinos could be detected. In contrast, for 9 of the considered 11 samples, less events than expected are found, while only for 2 samples slightly more events are measured on-source than the background expectation. The most significant deficit is found for the FR-I radio galaxies with a significance of -2.7σ, while the largest excess is found for FR-II radio galaxies with 0.5σ. The significance distribution of all considered samples is plotted in Fig. 5.13. The generally lower numbers of on-source events motivated further more detailed investigations on the systematic errors of the analysis which will be discussed below. No asymmetry in the background could be proven.

Consequently, only upper limits on the collective neutrino flux could be calculated. A confidence level of 90% has been chosen for the limits. The statistical uncertainties of the background are taken into account according to [C$^+$03, TC05]. The limit on the neutrino flux from the corresponding AGN category is included in Tab. 5.5. In Fig. 5.14, the obtained limits for generic sources are compared with the single source sensitivity of AMANDA with the considered data set [A$^+$05d, A$^+$] and with the expected sensitivity of IceCube based on one year of data [A$^+$04d].

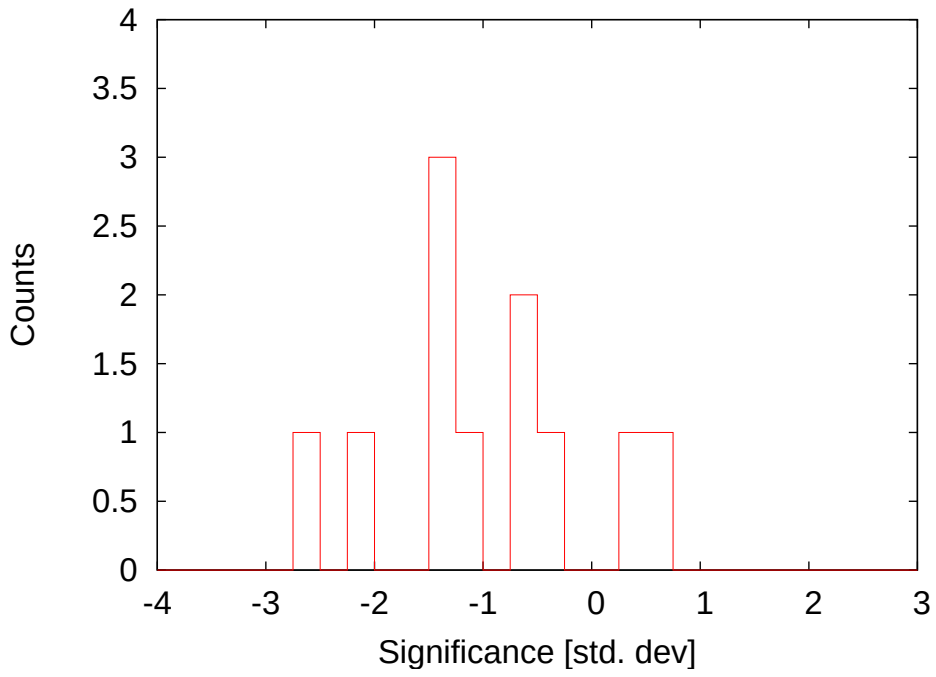

Figure 5.13: Significance distribution of the source stacking samples (2000-2003 event sample).

The derived limits do not contain systematic errors. A detailed investigation of systematic errors is currently being done in the AMANDA collaboration, including a more detailed description of ice parameters in the detector simulation. Preliminarily, the systematic uncertainties can be estimated from the uncertainty of the atmospheric neutrino flux (25%), the cross section for charge current interactions of ν_μ (10%) and the contamination of the data set by misreconstructed atmospheric muons (5%). Combining these independent errors results in an estimate of the total systematic error to be at 30% to be added to the presented limits.

5.4.4 Investigations on systematic errors of the background

Several additional tests are performed in order to check, whether the observed deficit of on-source events may be caused by systematic errors. An error in the background estimation could be excluded by performing the analysis on data sets with randomized RA. With a different software code, the event density is determined as a function of the angle to the source. A superposition of the event density around all sources in the considered samples is plotted in Fig. 5.15 as a function of the angular difference to the corresponding source.

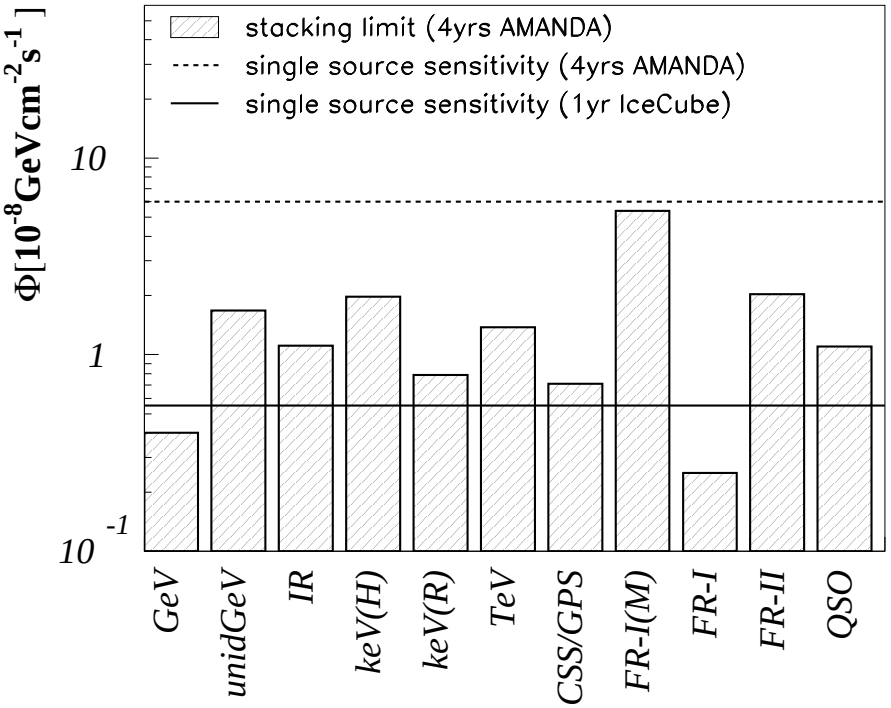

Figure 5.14: Limits on the flux per generic source using the 4 year data set.

The time structure of the ratio of observed events to expected events is analyzed. The year of the observation is considered as well as the day within the year. A structure in the latter could be due to seasonal variations of the rate of atmospheric neutrinos. Figure 5.16 shows clearly that no structure in the day of year is present, while there are hints that the deficit decreases with time. A strict evidence of a structure is, however, not present.

Additionally, it is tested, if the event deficit originates in a certain zenith range. For this, the cumulative signal of all sources in the same zenith range is evaluated. It turns out that the ratio of observed events to expected events is smallest in the range of $0.2 < \sin(\theta) < 0.3$. The event sample is searched for any further deviations from the expectation in this zenith range. In Fig. 5.17, the histogram of the zenith angle is shown for events, where the number of channels with at least one hit, Nch, is larger than 60. The zenith angle distribution of these large events deviates from the expectation from Monte Carlo simulations of atmospheric neutrinos. There is an excess at the same zenith interval where the observed event deficit observed is strongest. If these events are misreconstructed atmospheric muons, their distribution is expected to be flat in RA as well. Since the event selection is not optimized for

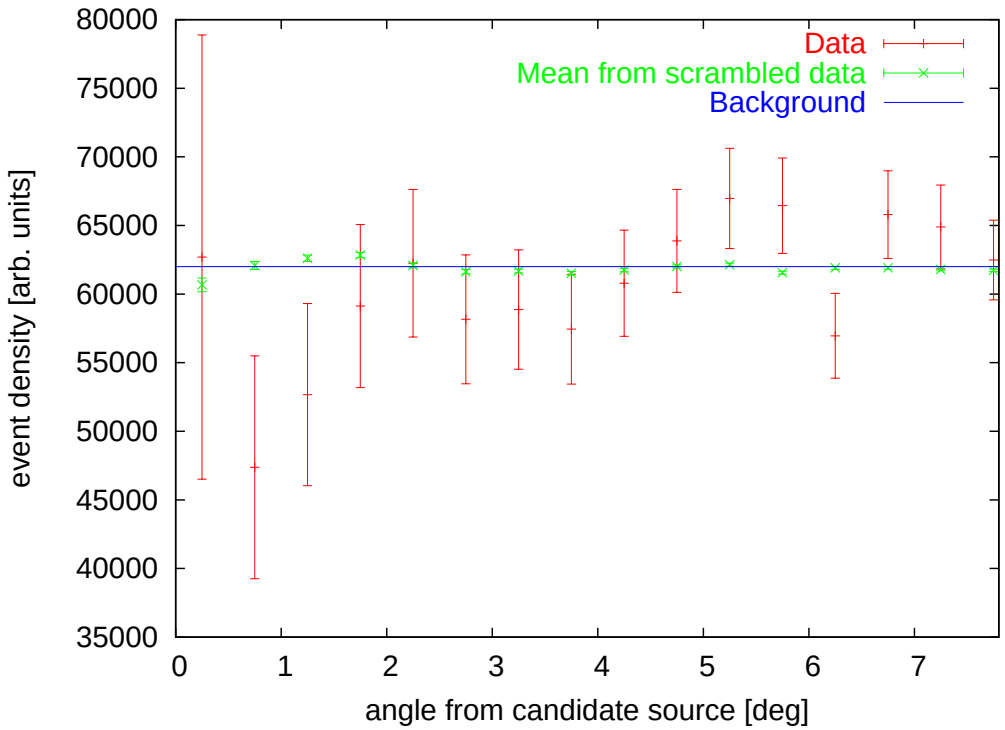

Figure 5.15: Event density as a function of the angular difference to candidate sources. The background expectation is indicated by the horizontal line. The mean from scrambled data sets shows only small deviations from the background expectation, while for the unscrambled data, the event density has a minimum close to the sources.

maximum purity, the presence of a few percent of misreconstructed atmospheric muons in the neutrino sample is expected. However, due to the similar zenith structure of these events and the observed event deficit, a further investigation of the events is necessary.

For this reason, the events with $Nch > 60$ and $\delta < 40°$ are isolated and a test with stacking of randomly distributed sources is performed only with these events. No deviations to randomized data set have been detected. The power of this method was proven by considering randomized data sets, where a RA structure was put to 1/2 or 1/3 of the events. The effect of these structures in the significance distribution is clearly visible. If less events contribute to a structure in RA, the number of events is too small to explain the observed event deficit. In these considerations no evidence of a structure in the RA distribution could be found. This supports the assumption of a flat background with sufficient accuracy, i.e., any deviation from this assumption is smaller than the statistical error of the background expectation.

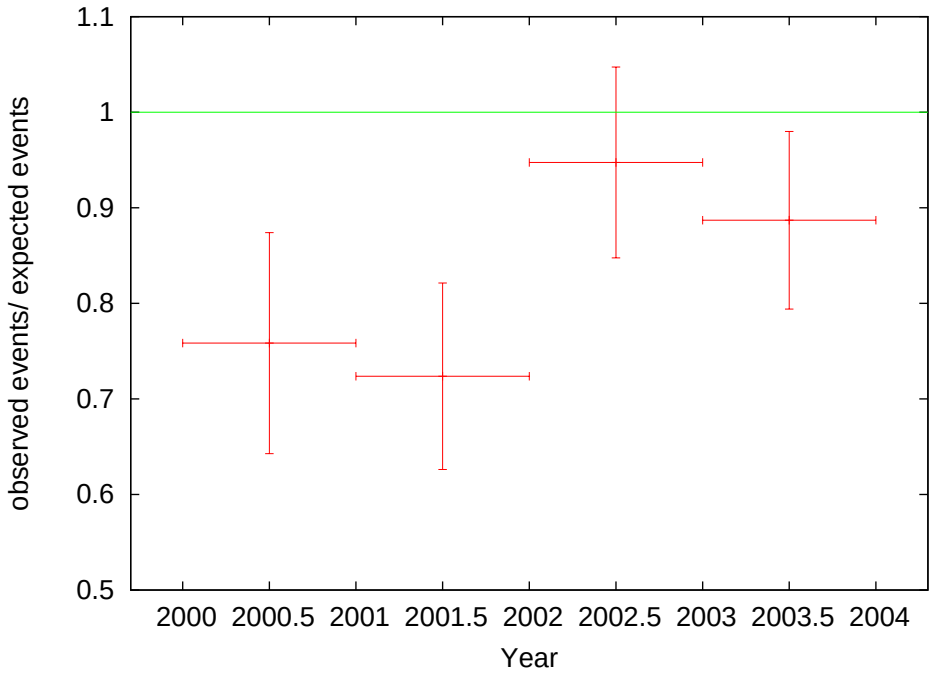

(a)

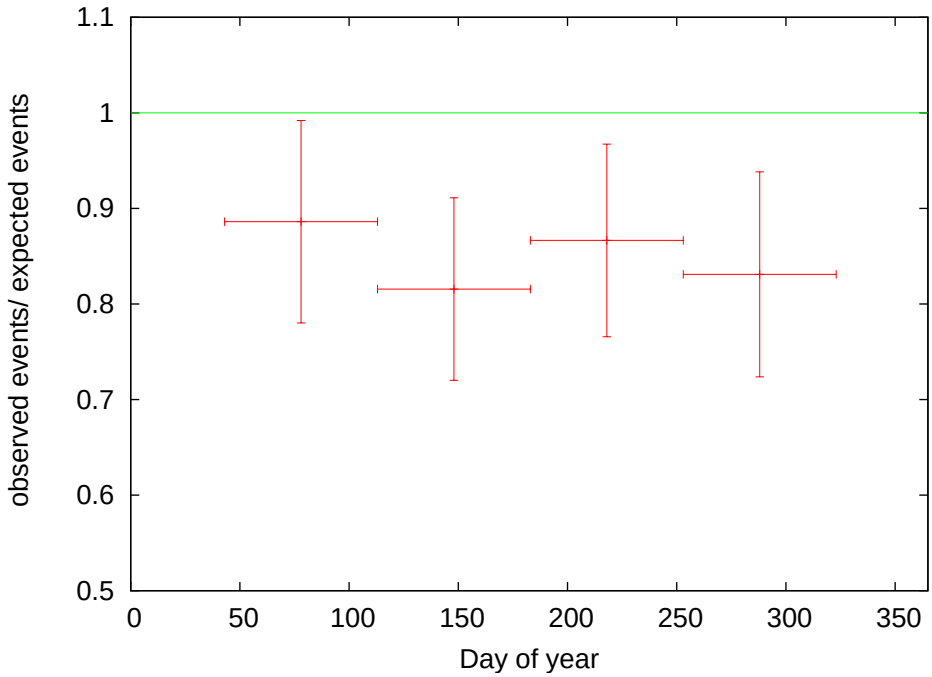

(b)

Figure 5.16: Ratio of observed to expected on-source events as a function of time. In (a), the year of the events is considered. In (b), this ratio is plotted as a function of the day of the year as a check for a seasonal dependence of the observed event deficit on-source.

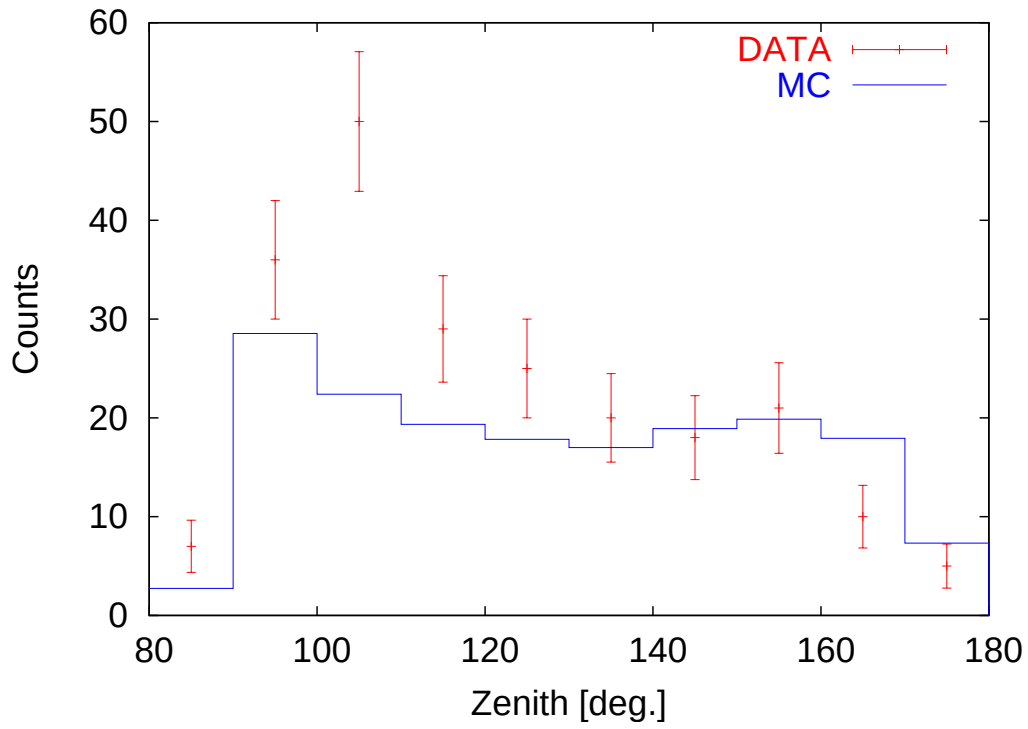

Figure 5.17: Zenith angle distribution for events with $Nch > 60$: the measured number of events deviates from the Monte Carlo expectations from atmospheric neutrinos for small zenith angles. The largest deviation has been found between $\Theta = 100°$ and $\Theta = 110°$. The additional events are most likely misreconstructed atmospheric muons.

5.5 Conclusions

In this chapter, the derived catalogs of generic AGN have been analyzed for a cumulative neutrino flux using data collected by AMANDA. Two data sets have been considered. The previously performed standard point source analysis of these data sets resulted in no evidence of a high energy neutrino point source. The aim of the source stacking analysis has been to improve the AMANDA sensitivity to generic sources and possibly to allow in this way for the detection of generic sources, when individual sources are slightly below the sensitivity. First, the source stacking method has been illustrated using data collected in the year 2000. Then, the most sensitive data set collected in the years 2000 till 2003 has been analyzed. In these analyses, the sensitivity to generic AGN classes has typically been improved by a factor of three, depending on the individual samples. However, for none of the considered samples a statistically significant excess over the background expectation has been found and no generic point source has been detected. The upper limits obtained by source stacking give presently the strongest constraint on the neutrino flux from astrophysical objects.

The limits to generic sources based on one year of AMANDA data are below the sensitivity of AMANDA to single sources based on 4 years of data. With the 4 year data set, providing currently the greatest sensitivity, limits on generic AGN are derived in the range of the expected sensitivity of the IceCube detector to single sources based on one year of data [A$^+$04d]. Especially for those samples where less events are observed than expected from the background, the limits represent a strong constraint on the neutrino flux. For the GeV blazars, where only 12 on-source events are observed at an expected background of 20.5 events, the resulting limit is for instance below the IceCube sensitivity to single sources. Given these limits, by extending the lifetime of AMANDA, a significant improvement of the limits or the detection of point sources with AMANDA is unlikely. An improvement of the sensitivity by a factor of two requires 16 years of data. The derived constraints on the flux suggest the application of source stacking methods to a more sensitive detector, e.g., to the IceCube detector.

6

Analysis of galactic candidates for neutrino sources

The possibilities to improve the analysis of galactic candidates for high energy neutrino sources are discussed in this chapter. First the possibilities to extend the method of source stacking from AGN to galactic sources are considered. Then, a different approach is presented, since many galactic sources have are time-dependent photon flux. If this time-dependence is taken into account, the sensitivity gets increased by background reduction. Pulsars show pulsed emission with a period of milliseconds to seconds. As an example for an time-dependent approach, the Crab Pulsar is analyzed here for pulsed neutrino emission. A time-dependent analysis of AGN and microquasars by selecting active periods according to the photon light curves has been done elsewhere [A$^+$05a].

6.1 Considerations on source stacking of galactic source candidates

In addition to AGN, there are further TeV neutrino source candidates. On the one hand there are transient extragalactic sources like gamma-ray bursts (GRB). For the GRB, a search for the cumulative signal has already been applied with AMANDA using data from 1997 till 2000 [H$^+$03]. The analysis is based on a search for a coincidence in direction and in time. On the other hand, several types of neutrino source candidates in our own galaxy have been discussed. A recent review of galactic neutrino source candidates can be found in [BBM05].

Microquasars are jet-disk systems similar to AGN with a central mass (black hole or neutron star) of about $1 - 10$ solar masses in binary systems. In these systems, the accretion disk is fed by the second star losing matter. Due to the smaller size of the systems in comparison to AGN, the accretion disk is located much closer to

the central mass. That yields a higher temperature in the inner part of the disk of several million degrees shifting the thermal emission from the blue bump in AGN spectra into the X-ray regime. While radio emission has been detected for many X-ray binaries, due to a high background in the galactic plane and relatively weak emission only in a few X-ray binary systems a radio jet has been resolved. Current microquasar samples require a resolved jet for the selection of X-ray binaries and contain less than 20 sources. The detection of hydrogen spectral lines in the jet of SS433 demonstrates the presence of hadrons and enhances the expectation of neutrino production. Since microquasar systems are much smaller than AGN, the time scales are much shorter. For example, significant changes of the accretion rate have been observed. Unlike the variability of AGN occurring at a roughly constant accretion rate, for microquasars the accretion rate itself is variable within typical observation time scales. Thus, depending on the time variability of the matter transfer from the companion star, some microquasars are persistent, some intermittent or periodic sources [DGWL02].

This subdivides the small sample again in various subclasses, making stacking of these sources more complicated. There are only two steady sources in the Northern Sky, SS433 and Cyg X-1 [DGWL02]. For Cyg X-1, the jet could not be resolved due to its weak radio emission. It is estimated to be three orders of magnitude weaker than that of SS433. Therefore, a stacking analysis of these two sources is not more sensitive than the standard point source analysis of SS433 alone.

In addition to the microquasars detected in X-rays and in radio photons, a subsample of the unidentified EGRET sources close to the galactic center may also consist of microquasars [R$^+$04a]. If this hypothesis is true, these sources might be a relevant class for a stacking analysis, especially for neutrino telescopes sensitive to the Southern Hemisphere.

Further galactic source candidate classes are different types of supernova remnants covering plerions, pulsars in binary systems and magnetars. Plerions are supernova remnants with a filled morphology, containing a pulsar in the center. A pulsar is a rotating neutron star from which pulsed photon fluxes are detected. The spectra from the radio frequencies to X-rays are well-understood as synchrotron emission of relativistic e^+e^- pairs emitted from the central pulsar. The origin of the highest energy emission may be, as in AGN, hadronic processes like pion decay or pure leptonic Compton upscattering of synchrotron photons. If the first mechanism is dominant, a neutrino flux similar to the photon flux is expected.

The prototype plerion is the Crab Nebula, the remnant of a supernova that erupted in 1054. In the Northern Sky, only very few plerions have been detected and the emission is strongly dominated by the Crab Nebula. Further plerions in the Northern Sky are PSR 1951+32 and PSR J0205+6449. Their luminosities of $3.7 \cdot 10^{36}$ erg/s [GM96] respectively $2.6 \cdot 10^{36}$ erg/s [M$^+$02] are substantially weaker than the Crab Nebula luminosity of $4 \cdot 10^{38}$ erg/s. In the high energetic photon radiation, the

Crab Nebula is even more dominant. Neither PSR 1951+32 nor PSR J0205+6449 have been detected in the regime of highly energetic photons. Hence, when selecting according to any of these parameters, the resulting sample would consist of the Crab Nebula alone.

Further source classes discussed consist of one source in the Northern Sky only, the magnetar SGR 1900+14 and the binary system A 0535+26. Additionally the dense matter region at Cygnus OB2 is likely to contain a neutrino emitting pulsar.

For these classes of galactic source candidates, no samples of sufficiently similar generic sources have been found in the Northern Sky. Therefore, a stacking analysis of these source classes is not more sensitive than the analysis of the strongest source only. In the Southern Sky, the situation may be different since the central region of the galaxy can be observed.

6.2 An analysis of pulsed emission of high energy neutrinos from the Crab Nebula

The Crab Nebula is the brightest plerion showing bright continuum emission and filamentary structures. The compact object in the center of the nebula is the Crab Pulsar. The pulsar and the nebula have been observed in photons in every accessible wavelength band. The period of the pulsed emission is 33 ms [A$^+$04a].

The total loss of spin energy of the pulsar may be described by the spin-down luminosity of the pulsar, which has been found to be $L = 5 \cdot 10^{38}$ erg s^{-1}. Pulsed emission from the central object has been detected in sub-mm, radio, keV and GeV photons. While the Crab Nebula is the strongest persistent source in TeV photons, no pulsed emission has been found in this energy band. An upper limit of less than 3% of the Crab Nebula TeV emission could be set on the pulsed emission [A$^+$04a]. The Crab Pulsar emission is characterized by a bimodal pulse shape, where the two maxima are separated by $\sim 145°$ in phase. The relative strength of both peaks and the exact position of the peaks varies with the photon energy. In addition to these maxima present at various photon energies, two further maxima have been found in the radio emission at frequencies between 4.7 GHz and 8.5 GHz.

The detection of pulsed emission of high energy photon raises the question, if high energy neutrinos may be emitted from the pulsar. The non-detection of pulsed TeV photons does not exclude the production of TeV neutrinos in the pulsar, since the production environment may be optically thick for TeV photons. If neutrinos are emitted in a pulsed way, it is possible to reduce the background of atmospheric neutrinos by considering only time intervals simultaneously to the maxima of the pulsed emission.

The detection of various maxima in the photon flux, depending on energy, does not determine the hypothetical neutrino phase in a clear way. Hence, a search for an accumulation of neutrinos at any value of the phase is performed.

The calculation of the phase from the arrival times of the neutrinos is done similar to the calculations presented in [R$^+$04b]. The Jodrell Bank Crab Monthly Ephemeris provide about one absolute arrival time of the main pulse at the Sun after a dispersion correction to infinite frequency. With help of the exact period of the Crab Pulsar at that time, the phase of an arbitrary time can be calculated. The estimated time accuracy is listed additionally. It is typically around 100 μs, though there are a few periods with up to 4000 μs uncertainty. With the current bounds on the neutrino mass, the delay of TeV neutrinos in comparison to photons in vacuum propagating from the Crab Pulsar to the Sun is negligible. The travel time from the Sun to Earth, however is of the order of minutes and thus it is relevant. Consequently, a barycenter correction from the center of the solar system to the geographic South Pole has to be applied. This correction is done with help of the tool faseBin [Bla95].

With this procedure, the phase of all events in a search bin around the Crab Nebula is calculated. The $2000 - 2003$ data set, as presented in Chapter 5, is considered. It contains 10 events in the on-source bin, while the background of atmospheric neutrinos is determined to 5.36 events. Periods are excluded, when the time uncertainty of the Crab Pulsar is above 1 ms. The bin size is chosen at 1/40 period of the Crab Pulsar.

In none of the phase bins, a statistically significant accumulation of events is found. This means, there is no evidence for pulsed emission of high energy neutrinos from the Crab Pulsar. In Fig. 6.1, the histogram of the observed phase of the neutrinos is compared with the phase distribution of photons in various wavelengths from radio to X-rays.

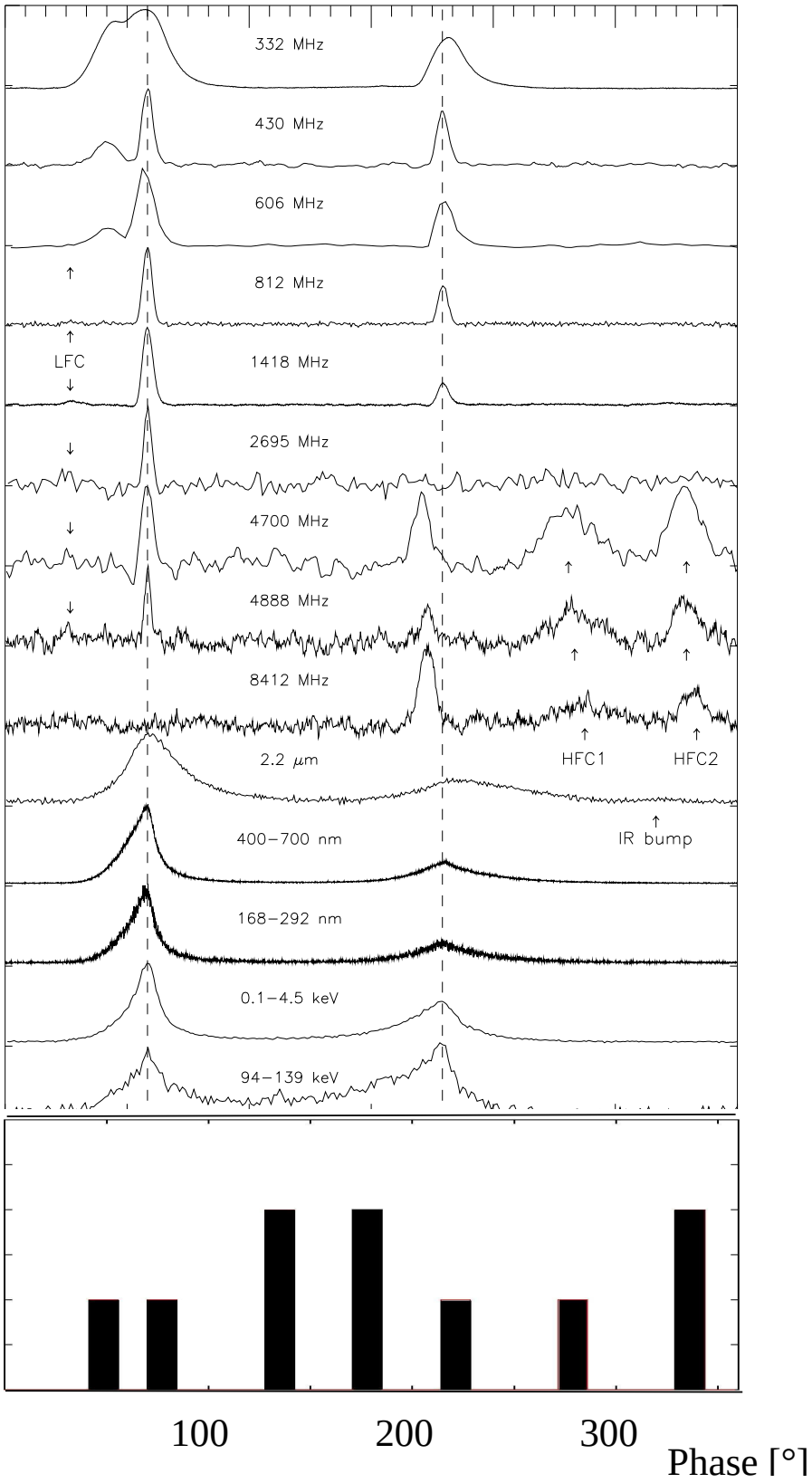

Figure 6.1: Multi-wavelength and multi-messenger data from the Crab Pulsar. Photon data at wavelengths from radio to X-rays from [MH96] are compared with the phase histogram of high energy neutrinos detected by AMANDA from 2000-2003 in a search bin around the Crab Pulsar.

7

Summary and outlook

The AMANDA neutrino telescope provides currently the greatest sensitivity to point sources emitting high energy neutrinos. Several searches for point sources were performed with data from AMANDA [A^+04c, A^+05c, A^+]. However, no point source was detected in these analyses. The absence of detected sources motivated to select the improvement of AMANDA's sensitivity as the central aim of this thesis. The source stacking method was known from photon astronomy to improve the sensitivity by the evaluation of the cumulative signal from several sources of the same type. In this thesis, the source stacking method has been applied to neutrino astronomy for the first time. Active Galactic Nuclei have been chosen as theoretically promising candidate sources.

The presented source stacking analysis was based on a systematical definition of samples of generic AGN. The attributes of generic AGN classes have been identified with help of an axisymmetric AGN model and by the consideration of intrinsical differences among AGN like the luminosity dependent jet morphology. Since the detailed neutrino production in AGN is unknown, the correlation between photon production and neutrino production has been used to sort the AGN samples with respect to their photon flux. Various photon energy intervals below the AMANDA energy threshold have been considered, because in optically thick sources the energy of TeV photons gets redistributed by electromagnetic cascades to photons of lower energy.

For each sample of generic AGN, the number of sources to be analyzed with AMANDA has been optimized. In the optimization, a linear correlation between the measured photon flux and the expected neutrino flux has been assumed. Typically, the optimum samples contain about 10 AGN.

In comparison to the point source analysis based on the same data set, the sensitivity to generic AGN classes has been improved by the source stacking analysis on average by a factor of three. For none of these samples, a neutrino flux has been detected. The derived 90% confidence level upper limits on the flux of generic AGN

AGN category	Limit to a generic point source $[10^{-8}$ GeV cm^{-2}s$^{-1}]$
GeV blazars	0.40
unid. GeV sources	1.44
IR blazars	1.12
keV blazars (HEAO-A)	1.97
keV blazars (ROSAT)	0.79
TEV blazars	1.38
GPS and CSS	0.71
FR-I galaxies	5.4
FR-I without M87	0.25
FR-II galaxies	2.04
radio-weak quasars	1.14
single point source (4yr AMANDA)	$\sim$6
single point source (1yr IceCube)	$\sim$0.55

Table 7.1: Results of the source stacking analysis for each AGN category: the limit on the differential flux per source multiplied by E^2 is given by f_{lim}/N_{src} in units of 10^{-8} GeV cm^{-2}s^{-1}. For comparison, the average sensitivity to single point sources for the presented AMANDA data set is listed as well as with the expected sensitivity for one year of IceCube data [A$^+$04d].

are summarized in Table 7.1. For comparison, the expected sensitivity for one year of data of the IceCube neutrino telescope currently under construction [A$^+$04d] is included in the table. Since the limits on the neutrino flux of generic AGN obtained with data from AMANDA are in the range of the expected sensitivity of IceCube to single point sources for one year of data, they represent a significant constraint on the high energy neutrino flux from AGN.

In addition to AGN, galactic source classes have been discussed in this thesis. The application of the source stacking methods to the considered galactic source classes was not adequate, because these classes are dominated by their strongest source. A complimentary way to improve the sensitivity is the time-dependent analysis of variable candidate sources. This technique reduces the background by selecting only active periods of the source. An example of a time-dependent analysis has been given in this thesis by the search for a pulsed high energy neutrino flux from the Crab Pulsar. No evidence for a pulsed neutrino emission has been found.

Since the improvement of sensitivity reached by the applied methods was not sufficient to detect a point source with AMANDA, a more sensitive detector like IceCube will be required for a detection. The source stacking method presented in this thesis is also relevant for IceCube. Due to the constraining limits in the range of the IceCube sensitivity, a detection of point sources with IceCube is questionable without the application of dedicated analysis techniques making use of astronomical information about the sources.

For the source stacking method, the sensitivity gain with IceCube is even larger than for an all-sky search using a grid of bins. In the all-sky search, the improvement of the sensitivity due to the better angular resolution of IceCube is partially compensated by an increase of the statistical trial factor caused by the larger number of search bins. An analysis, which preselects candidate sources from astronomical catalogs, benefits from the improved angular resolution without restrictions.

These considerations emphasize the relevance of the presented method for the IceCube experiment. The source stacking method can easily be adapted to the parameters of IceCube and some extensions of the method are possible. Further source classes can be considered additionally. Regions in our galaxy with an increased matter density, e.g., molecular clouds, are a target for CRs to interact. A detection of neutrinos produced in these interactions would give information on the matter density and the CR flux at these clouds. Another reservoir of candidate sources is given by the large number of galactic sources detected by EGRET in GeV photons with no identification at other wavelengths.

Furthermore, the inclusion of time information in the source stacking method may combine the advantages of both techniques. A stacking analysis of GRBs will naturally be an example of a time-dependent source stacking analysis. In the case of AGN, the classification as presented in this thesis may be extended on AGN flares, which are periods of enhanced high energy photon emission. The idea of such an analysis is to get the best possible signal to noise ratio by selecting only the active periods of several sources.

Summarizing, the sensitivity to the flux of generic AGN has been improved in this thesis. In future, the application of the source stacking method to data from more sensitive neutrino telescopes is valuable and an extension of the method is possible.

Appendix A

Physical constants and units

Physical constants

Constant		Value	Explaination
c	$=$	2.998×10^{8} m/s	Speed of light (in vacuum)
e	$=$	1.602×10^{-19} C	electron charge
$\hbar = h/2\pi$	$=$	6.582×10^{-22} MeV s	reduced Planck constant
m_e	$=$	9.109×10^{-31} kg	electron mass
	$=$	0.511 MeV$/c^2$	
m_p	$=$	1.007×10^{-27} kg	proton mass
	$=$	938.3 MeV$/c^2$	

Common units in Astroparticle Physics

Unit		SI Unit	Name
1 ly	$=$	9.4605×10^{15} m	light year
1 pc	$=$	3.0857×10^{16} m	parsec
	$=$	3.2616 ly	
1 eV	$=$	$e \cdot 1$ V	electron volt
	$=$	1.602×10^{-19} J	
1 erg	$=$	0.624 TeV	
1 $M_\odot$	$=$	1.989×10^{30} kg	solar mass

Appendix B

The distance correction of fluxes

The distance dependence of a measured flux density F_ν at the observer's frequency ν of a source with luminosity $L_{\nu'}$ is given by

$$F_\nu = L_{\nu'} \frac{1}{4\pi d_l(z)^2}\,, \tag{B.1}$$

with the luminosity distance d_l and the frequency at the source $\nu' = \nu(1+z)$. In a cosmology with non-vanishing cosmological constant Λ, the luminosity distance as a function of redshift [CPL92] is given by

$$d_l(z) = \begin{cases} \frac{(1+z)c}{H_0 \cdot |\Omega_k|^{0.5}} \sin\left\{|\Omega_k|^{0.5} \cdot I(z)\right\}\,, & \text{if } \Omega_k < 0\,, \\ \frac{(1+z)c}{H_0}\,, & \text{if } \Omega_k = 0\,, \\ \frac{(1+z)c}{H_0 \cdot |\Omega_k|^{0.5}} \sinh\left\{|\Omega_k|^{0.5} \cdot I(z)\right\}\,, & \text{if } \Omega_k > 0\,, \end{cases} \tag{B.2}$$

I(z) is given by

$$I(z) = \int_0^z \left[(1+z')^2 \cdot (1+\Omega_m z') - \Omega_\Lambda z'(2+z')\right]^{-0.5} dz'\,, \tag{B.3}$$

with the normalized curvature Ω_k. The cosmological parameters have been taken according to the values found in recent measurements, $\Omega_m = 0.27 \pm 0.04$ for the normalized mass density, $\Omega_\Lambda = 0.75 \pm 0.04$ the normalized dark energy density [S$^+$03] and $h = 0.71^{+0.04}_{-0.03}$ for the Hubble parameter [B$^+$03]. Then, the Friedmann equation yields

$$\begin{aligned} \Omega_k &= 1 - \Omega_m - \Omega_\Lambda \\ &= -0.02 \pm 0.06\,, \end{aligned} \tag{B.4}$$

compatible with a spatially flat geometry.

For a power law spectrum with spectral index α, the redshift results in

$$L_{\upsilon'}\mathrm{d}\nu' = L_{\nu\cdot(1+z)} \cdot (z+1)^{\alpha+1}\mathrm{d}\nu\,. \tag{B.5}$$

Finally, the correction to $z = 0.1$ for a source at redshift z is given by

$$F^{z=0.1} = F \cdot \left(\frac{d_l(z)}{d_l(z=0.1)}\right)^2 \cdot \left(\frac{z+1}{0.1+1}\right)^{\alpha+1}\,. \tag{B.6}$$

Appendix C

Source catalogs for AMANDA

radio source (1950 coord)	**IR source** (1950 coord)	F_{5GHz} [Jy]	**SI**	$F_{12\mu\mathrm{m}}$ [Jy]	$F_{25\mu\mathrm{m}}$ [Jy]	$F_{60\mu\mathrm{m}}$ [Jy]	$F_{100\mu\mathrm{m}}$ [Jy]	**z**	$F_{5GHz}^{z=0.1}$ [Jy]
1Jy 0851+20	IRAS F08519+2017	2.62	0.11	0.2838	0.4335	0.8911	1.1580	0.306	36.8
1Jy 1404+28	IRAS F14047+2841	2.95	0.80	0.1850	0.3994	0.7288	0.9376	0.077	1.7
1Jy 1641+39	IRAS F16413+3954	10.81	0.54	0.1068	0.2918	0.5999	1.3840	0.594	756
1Jy 1308+32	IRAS F13080+3237	1.53	0.20	0.1744	0.2710	0.4198	0.5760	0.996	525
1Jy 2200+42	IRAS F22006+4202	4.77	-0.13	0.1393	0.2495	0.4029	1.9690	0.070	2.2
1Jy 1732+38	IRAS F17326+3859	1.13	0.85	0.0964	0.1688	0.3280	0.6699	0.970	246
1Jy 1803+78	IRAS F18036+7827	2.62	0.25	0.0931	0.1826	0.3083	0.7386	0.684	301
1Jy 0735+17	IRAS F07352+1749	1.99	0.05	0.1868	0.1907	0.2519	0.5198	0.424	66.3
1Jy 0716+71	IRAS F07162+7126	1.12	0.22	0.1121	0.1260	0.2374	0.7825	0.300	15.7
1Jy 0235+16	IRAS F02358+1623	2.85	1.03	0.1105	0.1068	0.2344	0.9074	0.851	403
1Jy 1418+54	IRAS F14180+5437	1.09	0.38	0.0659	0.0857	0.2121	0.5459	0.151	2.7

Table C.1: Strongest IR sources in blazar catalog. F_{5GHz} stands for the radio flux at 5 GHz [K$^+$81b], while the mean IR flux at $12, 25, 60$ and 100 μm is labeled $F_{12\mu m} \ldots F_{100\mu m}$ [M$^+$90]. SI is the spectral index α determined between 2.7 GHz and 5 GHz. z is the cosmological redshift. The distance corrected radio flux flux is given by $F_{5GHz}^{z=0.1}$. The IR data has been taken in the 1980s.

X-ray source (2000 coord)	**Radio source** (1950 coord)	F_X [cnt/s]	**HR I**	**HR II**	F_{5GHz} [Jy]	**SI**	**z**	$F_{5GHz}^{z=0.1}$
1RXS J172320.5+341756	S4 1721+343	1.0160	0.20	0.07	0.934	-0.43	0.206	5.2
1RXS J225358.0+160855	1Jy 2251+158	0.6094	0.96	0.26	17.42	0.64	0.859	3100
1RXS J084125.1+705342	1Jy 0836+710	0.5308	0.62	0.19	2.59	-0.32	2.16	15300
1RXS J115324.4+493108	1Jy 1150+497	0.3699	0.26	0.07	1.12	-0.48	0.334	22.1
1RXS J164258.9+394822	1Jy 1641+399	0.3253	-0.18	-0.05	10.81	0.54	0.594	756
1RXS J192748.0+735757	1Jy 1928+738	0.2772	0.86	0.25	3.34	-0.01	0.36	73.1
1RXS J220315.6+314535	1Jy 2201+315	0.2424	0.94	0.28	2.32	0.24	0.298	29.9
1RXS J092702.8+390221	1Jy 0923+392	0.2376	-0.16	0.38	8.73	1.03	0.698	756
1RXS J072153.2+712031	1Jy 0716+714	0.1925	0.12	0.19	1.12	0.22	0.30	14.7
1RXS J163813.1+572028	1Jy 1637+574	0.1158	0.03	0.24	1.42	0.35	0.750	202
1RXS J074541.2+314249	S2 0742+31	0.1147	0.81	0.57	0.96	-0.23	0.462	43.6
1RXS J220244.4+421626	1Jy 2200+420	0.1144	0.98	0.44	4.77	-0.13	0.070	2.2
1RXS J083454.3+553417	1Jy 0831+557	0.1027	0.58	0.03	5.65	-0.46	0.242	39.7
1RXS J135703.6+191915	1Jy 1354+195	0.1005	0.42	0.69	1.56	-0.07	0.720	239

Table C.2: ROSAT sources identified with strong radio blazars. The X-ray flux measured by ROSAT is given by F_X [V$^+$99]. The hardness ratios HR I and HR II display the ratio between low and high energetic X-rays: HR $= (n_{HE} - n_{LE})/(n_{HE} + n_{LE})$. For HR I the low energy range is $0.1 - 0.4$ keV and the high energy range is $0.5 - 2.0$ keV. For HR II the intervals are $0.5 - 0.9$ keV and $0.9 - 2.0$ keV. SI is the spectral index α determined between 2.7 GHz and 5 GHz. F_{5GHz} stands for the radio flux at 5 GHz [K$^+$81b, P$^+$72, P$^+$78]. SI is the spectral index α determined between 2.7 GHz and 5 GHz with $F_\nu \propto \nu^\alpha$. The distance corrected radio flux is given by $F_{5GHz}^{z=0.1}$.

HEAO-A source (1950 coord)	**radio source** (1950 coord)	F_X [cnt/s]	F_{5Ghz} [Jy]	**SI**	**z**	$F_{5GHz}^{z=1}$ [Jy]
1H0717+714	1Jy 0716+714	0.0030	1.12	0.22	0.30	14.7
1H1154+294	S3 1156+29	0.0029	0.89	-0.44	0.73	167
1H1922+746	1Jy 1928+73	0.0027	3.34	-0.01	0.36	73.1

Table C.3: HEAO-A sources identified with strong radio blazars: The mean flux measured by HEAO-A [W$^+$84] is given by F_X, and F_{5GHz} stands for the radio flux at 5 GHz [K$^+$81b, P$^+$78]. All data have been taken within an 6 month interval in 1977-1978, though the observation times of individual sources are shorter. SI is the spectral index α determined between 2.7 GHz and 5 GHz with $F_\nu \propto \nu^\alpha$. The cosmological redshift is given by z and the distance corrected radio flux flux is given by $F_{5GHz}^{z=0.1}$.

GeV source (2000 coord)	**radio source** (1950 coord)	$\mathbf{F}_{5\mathrm{GHz}}$ [Jy]	**SI**	$\mathbf{F}^{\mathrm{max}}_{\mathrm{GeV}} * 10^{-8}$ $[s^{-1}cm^{-2}]$	$\mathbf{F}^{\mathrm{mean}}_{\mathrm{GeV}} * 10^{-8}$ $[s^{-1}cm^{-2}]$	**z**
3EG J0450+1105	1Jy 0446+112	1.23	0.56	109.5	14.9	1.207
3EG J1635+3813	1Jy 1633+382	4.02	0.73	107.5	58.4	1.814
3EG J0530+1323	1Jy 0528+134	3.97	0.47	93.5	93.5	2.060
3EG J0237+1635	1Jy 0235+164	2.85	1.03	65.1	25.9	0.940
3EG J2254+1601	1Jy 2251+158	17.42	0.64	53.7	53.7	0.859
3EG J1200+2847	S3 1156+29	0.89	-0.44	50.9	7.5	0.73
3EG J2202+4217	1Jy 2200+420	4.77	-0.13	39.9	11.1	0.069
3EG J1608+1055	1Jy 1606+106	1.49	0.42	34.9	25.0	1.226
3EG J1614+3424	1Jy 1611+343	2.67	0.10	26.5	26.5	1.401
3EG J0829+2413	S3 0827+24	0.94	0.05	24.9	24.9	2.05
3EG J0204+1458	1Jy 0202+149	2.47	-0.43	23.6	8.7ă	0.405
3EG J2232+1147	1Jy 2230+114	3.61	-0.50	19.2	19.2	1.037
3EG J1738+5203	1Jy 1739+522	1.98	0.68	18.2	18.2	1.375
3EG J0721+7120	1Jy 0716+714	1.12	0.22	17.8	17.8	0.300
3EG J0737+1721	1Jy 0735+178	1.99	0.05	16.4	16.4	0.424
3EG J0958+6533	1Jy 0954+658	1.46	0.35	15.4	6.0	0.368
3EG J2358+4604	1Jy 2351+456	1.42	-0.05	14.3	14.3	1.992
3EG J0239+2815	1Jy 0234+285	1.44	-0.24	13.8	13.8ă	1.21
3EG J0917+4427	S4 0917+449	0.80	0.66	13.8	13.8	2.18
3EG J0853+1941	1Jy 0851+202	2.62	0.11	10.6	10.6	0.306ă
3EG J0845+7049	1Jy 0836+710	2.59	-0.32	10.2	10.2	2.172
3EG J0952+5501	1Jy 0954+556	2.28	-0.19	9.1	9.1	0.901

Table C.4: 3EG sources identified with strong radio blazars: F_{5GHz} is the radio flux [$\mathrm{K}^{+}81\mathrm{b}, \mathrm{P}^{+}78$] at 5 GHz [$\mathrm{K}^{+}81\mathrm{b}, \mathrm{PK}72, \mathrm{P}^{+}78$], SI is the spectral index α determined between 2.7 GHz and 5 GHz. The maximum and the mean flux as measured by EGRET in 1991-1995 [$\mathrm{H}^{+}99$] are listed under $\mathrm{F}^{\mathrm{max}}_{\mathrm{GeV}}$ resp. $\mathrm{F}^{\mathrm{mean}}_{\mathrm{GeV}}$. z is the cosmological redshift. The EGRET catalog uses the reference system of the year 2000.

EGRET source	F_{GeV}^{max} $[10^{-8}s^{-1}cm^{-2}]$	F_{GeV}^{mean} $[10^{-8}s^{-1}cm^{-2}]$	$\|b\|$ [°]	3EG Id. flag
3EG J2243+1509	73.1	9.9	37.49	
3EG J2255+1943	62.2	5.8	35.43	a
3EG J1835+5918	60.6	60.6	25.07	
3EG J1212+2304	50.8	3.3	80.32	
3EG J1850+5903	46.7	12.6	23.18	
3EG J0439+1555	42.9	4.8	19.98	
3EG J0010+7309	42.3	42.3	10.54	
3EG J1822+1641	40.6	7.1	13.84	
3EG J2314+4426	40.4	13.9	15.10	
3EG J2352+3752	37.5	6.1	23.54	a
3EG J1825+2854	34.3	6.5	18.03	
3EG J0407+1710	32.1	7.3	25.06	
3EG J1824+3441	28.7	8.1	20.14	
3EG J1308+8744	23.9	7.6	29.38	
3EG J1733+6017	22.9	8.7	32.94	
3EG J1227+4302	21.7	4.6	73.33	
3EG J1347+2932	21.0	9.6	77.50	
3EG J0910+6556	18.3	5.9	38.56	
3EG J1323+2200	18.1	5.2	81.15	a
3EG J0215+1123	18.0	9.3	46.37	
3EG J0329+2149	17.2	7.4	27.88	
3EG J0245+1758	16.9	8.8	37.11	
3EG J0426+1333	14.0	14.0	23.82	
3EG J0917+4427	13.8	13.8	44.19	a
3EG J2248+1745	12.9	12.9	36.17	

Table C.5: Unidentified and weakly identified extragalactic EGRET sources, possibly blazars. The maximum and the mean flux as measured by EGRET [H$^+$99] are listed under F_{GeV}^{max} resp. F_{GeV}^{mean}.

X-ray source	**other name**	F_{TeV} [crab flux]	**5 GHz flux** [Jy]	**z**
1ES 1101+38.4	Mrk 421	0.04-7.4	0.72	0.0300
1ES 1652+39.8	Mrk 501	0.33-6	1.38	0.0336
H 1426+428	-	0.03-0.08	0.04	0.1290
1ES 1959+650	-	0.05-2.20	0.25	0.0470
1ES 2344+514	-	0.03	0.23	0.0440

Table C.6: TeV blazars with $\delta > 10°$, The TeV fluxes [Wee03a] are listed in units of the flux of the Crab nebula, $dJ_\gamma/dE = (2.79 \pm 0.02 \pm 0.5) \cdot 10^{-7}(E/TeV)^{-2.59 \pm 0.03 \pm 0.05}$. F_{5GHz} stands for the radio flux at 5 GHz [K$^+$81b, P$^+$78, NED], while the cosmological redshift is given by z.

Coordinate name (1950 coord)	**other name**	**Sample**	**Mag**	**z**	F_{5GHz} [Jy]	θ [arcsec]	ν_m [MHz]	$\log P_{5GHz}$	**Size** [kpc]
0248+430	n. a.	G	15.5	1.316	1.24	0.06	5000	27.9	0.474
0134+329	3C 48	C	16.1	0.367	5.3	0.50	80	27.3	2.255
0738+313	n. a.	G	16.1	0.630	3.62	0.010	5300	27.6	0.061
1458+718	3C 309.1	C	16.8	0.905	3.5	2.11	40	28.0	14.831
1345+125	4C 12.50	G	17.0	0.122	3.05	0.080	400	26.0	0.160
1328+307	3C 286	C	17.2	0.849	7.4	3.2	80	28.2	21.966
0740+380	3C 186	C	17.6	1.063	0.3	2.2	40	27.2	16.330
1328+254	3C 287	C	17.7	1.055	3.2	0.048	50	28.1	0.355
0538+498	3C 147	C	17.8	0.545	8.2	0.55	150	27.9	3.101
1442+101	OQ 172	CG	17.8	3.535	1.20	0.02	900	29.3	0.185
0221+276	3C 67	C	18.0	0.309	0.9	2.5	50	26.3	10.100
2352+495	n. a.	G	18.4	0.237	1.49	0.050	700	26.3	0.168
2249+185	3C 454	C	18.5	1.758	0.8	0.66	40	28.1	5.562
0518+165	3C 138	C	18.8	0.760	4.1	0.60	100	27.8	3.942
0345+337	3C 93.1	C	19.0	0.244	0.8	0.25	60	26.0	0.858
1153+317	4C 31.38	C	19.0	1.557	1.0	0.9	100	28.0	7.397
1203+645	3C 268.3	C	19.0	0.371	1.1	1.36	80	26.6	6.175
1323+321	4C 32.44	CG	19.0	0.369	2.39	0.06	500	26.9	0.272
1443+77	3C 303.1	C	19.0	0.267	0.5	1.7	100	26.0	6.219
1819+39	4C 39.56	C	19.0	0.4	1.0	0.44	100	26.6	2.091
1358+624	4C 62.22	CG	19.9	0.429	1.80	0.07	500	26.9	0.347
0127+233	3C 43	C	20.0	1.459	1.1	2.60	20	28.0	21.054
0428+205	OF 247	CG	20.0	0.219	2.38	0.250	1100	26.4	0.793
1117+146	4C 14.41	G	20.0	0.362	1.00	0.08	500	26.5	0.358
1829+29	4C 29.56	C	20.0	0.842	1.1	3.1	100	27.3	21.212

Table C.7: GPS and CSS sources fulfilling our selection rules. In Sample, G means GPS and C means CSS. Mag is the optical magnitude. The cosmological redshift is given by z, while F_{5GHz} stands for the radio flux at 5 GHz. θ is the angular size of the source. ν_m is the turnover frequency and P_{5GHz} stands for log of power at 5 GHz (assuming isotropic emission). The linear size of the sources is listed in kpc [O'D98].

Source	F_{178} [Jy]	**SI**	δ [°]	**RA** [°]	**z**
3C 274.0	1050.	-0.76	12.6667	12.4667	0.004
3C 84.0	61.3	-0.78	41.3167	3.26667	0.017
3C 433.0	56.2	-0.75	24.85	21.35	0.101
3C 310.0	55.1	-0.92	26.2	15.0333	0.054
3C 338.0	46.9	-1.19	39.65	16.4333	0.029
3C 465.0	37.8	-0.75	26.75	23.5833	0.029
3C 83.1	26.0	-0.64	41.6667	3.23333	0.025
3C 264.0	26.0	-0.75	19.8833	11.7	0.020
3C 66.0	24.6	-0.62	42.75	2.33333	0.021
3C 386.0	23.9	-0.59	17.15	18.6	0.017
3C 272.1	19.4	-0.60	13.15	12.3667	0.003
3C 288.0	18.9	-0.85	39.1	13.6	0.246
3C 315.0	17.8	-0.72	26.3	15.1833	0.108
3C 31.0	16.8	-0.57	32.1333	1.06667	0.016
3C 28.0	16.3	-1.06	26.1333	0.883333	0.195
3C 442.0	16.1	-0.96	13.5833	22.2	0.026
3C 305.0	15.7	-0.85	63.4667	14.8	0.041
3C 231.0	14.6	-0.28	69.9167	9.85	0.000
3C 296.0	13.0	-0.67	11.0333	14.2333	0.023
3C 293.0	12.7	-0.45	31.6833	13.8333	0.045
3C 76.1	12.2	-0.77	16.2333	3	0.032
3C 449.0	11.5	-0.58	39.1	22.4833	0.017
3C 346.0	10.9	-0.52	17.35	16.6833	0.161
3C 314.1	10.6	-0.95	70.95	15.1667	0.119

Table C.8: FR-I radio galaxies: F_{178} is the radio flux at 178 MHz, SI is the spectral index α determined between 178 MHz and 750 MHz, RA and δ stand for right ascension resp. declination in the reference system of 1950 [S$^+$85]. Note, in the original 3CRR catalog, the spectral index is defined with an opposite sign. The cosmological redshift is given by z [L$^+$83].

Source	F_{178} [Jy]	**SI**	δ [°]	**RA** [°]	**z**
3C 123.0	189.0	-0.70	29.5667	4.55	0.218
3C 295.0	83.5	-0.63	52.4333	14.15	0.461
3C 196.0	68.2	-0.79	48.3667	8.15	0.871
3C 452.0	54.4	-0.78	39.4167	22.72	0.081
3C 33.0	54.4	-0.76	13.0667	1.1	0.059
3C 390.3	47.5	-0.75	79.7167	18.75	0.056
3C 98.0	47.2	-0.78	10.2833	3.93	0.030
3C 438.0	44.7	-0.88	37.7667	21.88	0.290
3C 20.0	42.9	-0.67	51.7833	0.67	0.174
3C 219.0	41.2	-0.81	45.85	9.28	0.174
3C 234.0	31.4	-0.86	29.0167	9.97	0.184
3C 61.1	31.2	-0.77	86.0833	2.17	0.186
3C 79.0	30.5	-0.92	16.9	3.12	0.255
3C 330.0	27.8	-0.71	66.0667	16.15	0.550
3C 427.1	26.6	-0.97	76.35	21.07	0.572
3C 47.0	26.4	-0.98	20.7	1.55	0.425
3C 388.0	24.6	-0.70	45.5	18.7	0.090
3C 280.0	23.7	-0.81	47.6	12.9	0.997
3C 228.0	21.8	-1.00	14.5667	9.78	0.552
3C 109.0	21.6	-0.85	11.0667	4.17	0.305
3C 55.0	21.5	-1.04	28.6167	1.9	0.734
3C 268.1	21.4	-0.59	73.2833	11.95	0.973
3C 225.0B	21.3	-0.94	13.9833	9.65	0.582
3C 192.0	21.1	-0.79	24.3	8.03	0.059
3C 401.0	20.9	-0.71	60.5667	19.65	0.201
3C 326.0	20.4	-0.88	20.2333	15.82	0.088

Table C.9: FR-II radio galaxies: F_{178} is the radio flux at 178 MHz, SI is the spectral index α determined between 178 MHz and 750 MHz RA and δ stand for right ascension resp. declination in the reference system of 1950 [S$^+$85]. Note, in the original 3CRR catalog, the spectral index is defined with an opposite sign. The cosmological redshift is given by z [L$^+$83].

quasar name	$F_{60\mu}$ [mJy]	z	$\log \nu f_{14.5}$
PG 0050+124	2293	0.061	-13.30
PG 1351+640	757	0.087	-13.86
PG 1440+356	652	0.077	-13.70
PG 1613+658	635	0.129	-13.97
PG 1119+120	546	0.049	-13.82
PG 1501+106	486	0.036	-13.54
PG 1700+518	480	0.292	-13.90
PG 1351+236	364	0.055	-13.75
PG 1543+489	348	0.400	-14.52
PG 2214+139	337	0.067	-13.70
PG 1634+706	318	1.334	-14.00
PG 1402+261	229	0.164	-14.10
PG 1248+401	224	1.030	-14.59
PG 0947+396	201	0.206	-14.57
PG 1148+549	196	0.969	-14.30
PG 1114+445	191	0.144	-14.14
PG 0804+761	191	0.100	-13.70
PG 0838+770	174	0.131	-14.25
PG 0906+484	172	0.118	-14.30
PG 1229+204	163	0.064	-13.74
PG 0844+349	163	0.064	-13.82
PG 1411+442	162	0.089	-13.87
PG 1448+273	117	0.065	-13.81
PG 1444+407	117	0.267	-14.28
PG 1415+451	112	0.114	-14.05
PG 0052+251	93	0.155	-14.09

Table C.10: Radio-weak quasars from the BQS [SG83, S$^+$89] sorted according to IRAS flux at $\lambda = 60\mu$m, $F_{60\mu m}$ [S$^+$89]. The cosmological redshift is given by z. The logarithm of the energy flux density is given by $\log \nu f_{14.5}$

Radio source	**other name**	**Samples (Position)**
1Jy 0316+41	NGC 1275	IR blazars (1), keV blazars (ROSAT (1) and HEAO-A (1))
1Jy 1652+398	Mrk 501	keV blazars (ROSAT (2) and HEAO-A (2))
1Jy 1222+13	M 84	IR blazars (6)
1Jy 0055+30	NGC 315	IR blazars (11)
1Jy 1807+698		keV blazars (HEAO-A (31))

Table C.11: Nearby intrinsically weak sources. Due to their proximity they nevertheless may contribute significantly to the neutrino flux at the Earth.

Appendix D

Plots of the optimization of the number of sources

D.1 The single year data set

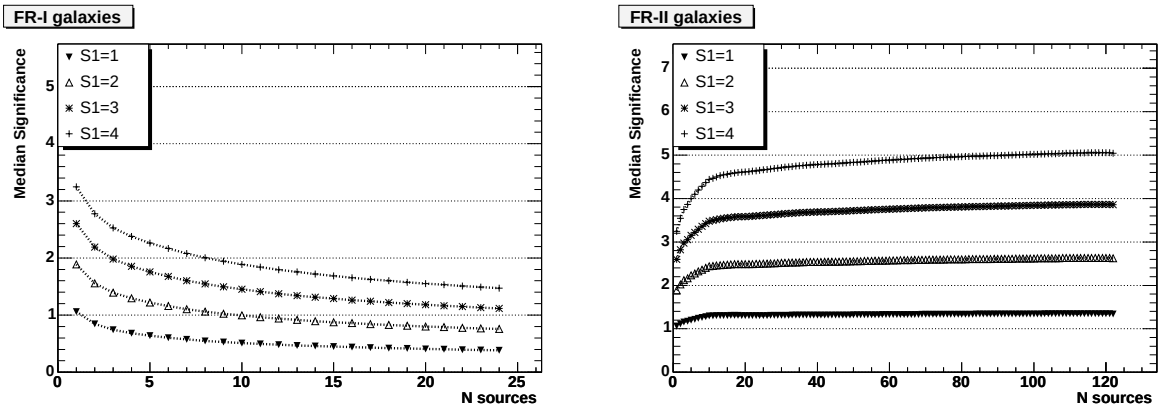

(a) (b)

Figure D.1: Median significance for the single year data set as expected under the considered hypothesis as a function of the number of radio galaxies to be stacked. The expectation value of the number of signal events for the strongest source is represented by $S1$. The highest value of the median significance corresponds to the optimum number of sources.

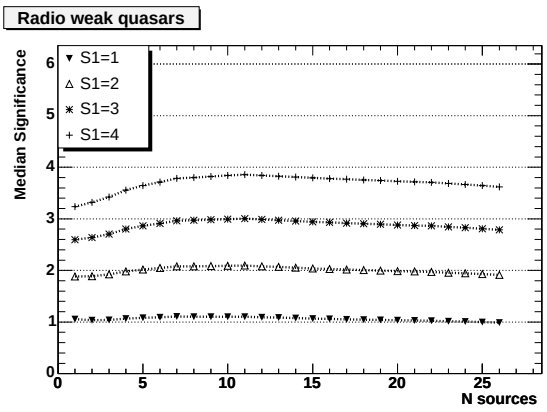

(a)

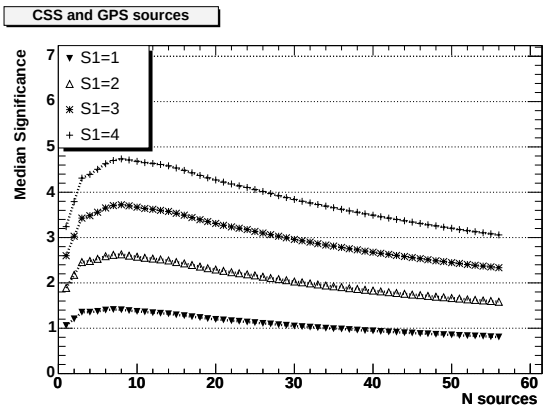

(b)

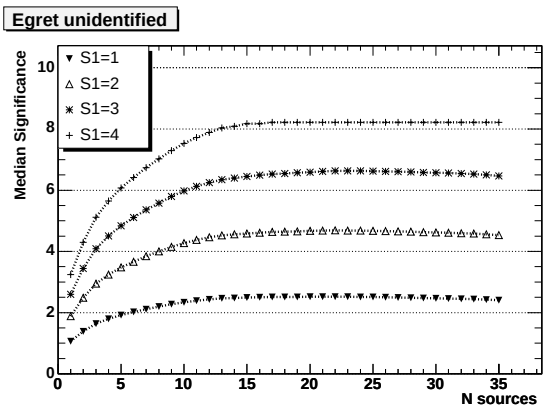

(c)

Figure D.2: Median significance for the single year data set as expected under the considered hypothesis as a function of the number of QSO (a), compact AGN (b) and unidentified EGRET sources (c) to be stacked. The expectation value of the number of signal events for the strongest source is represented by $S1$. The highest value of the median significance corresponds to the optimum number of sources.

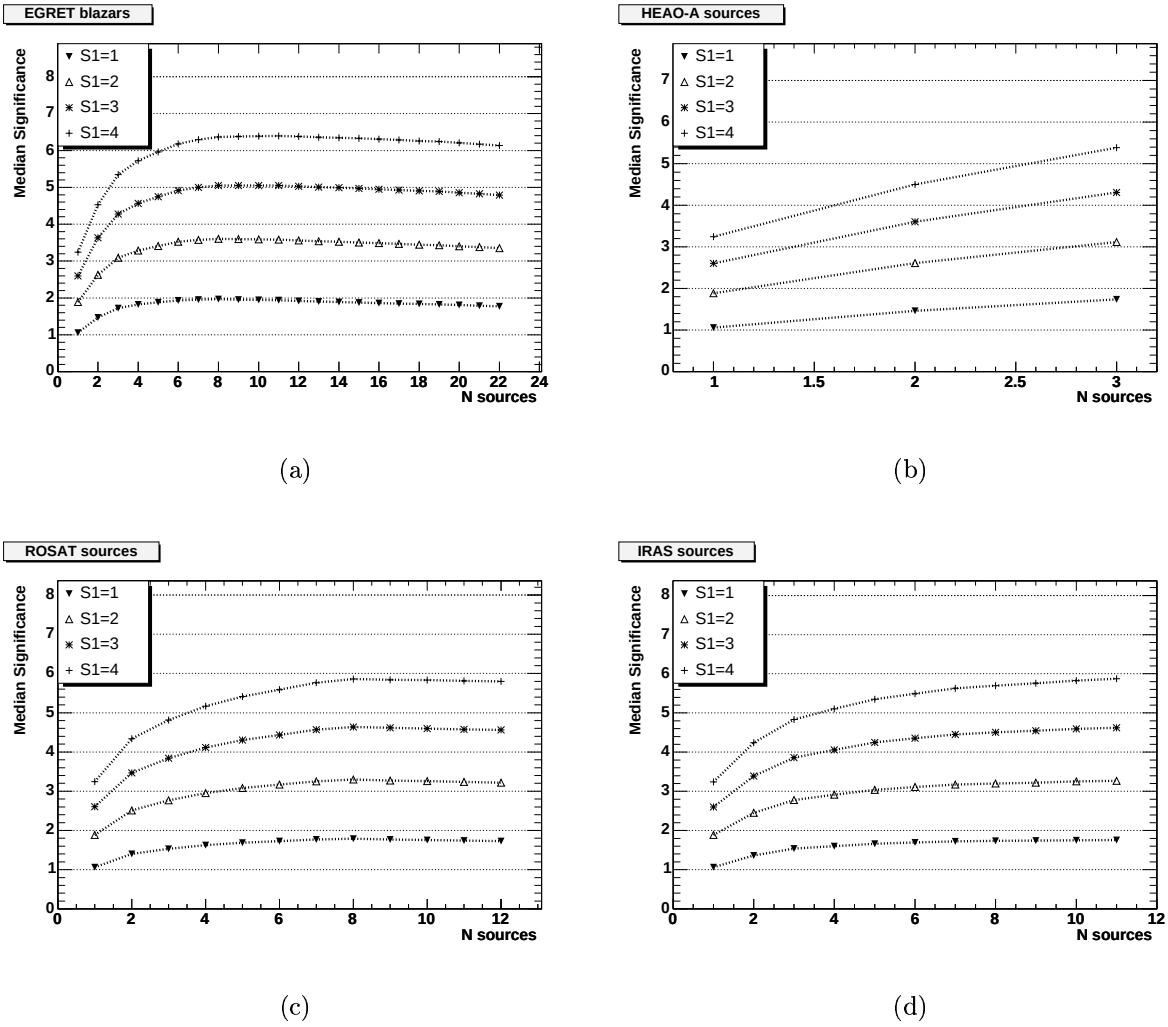

Figure D.3: Median significance for the single year data set as expected under the considered hypothesis as a function of the number of blazars to be stacked. The expectation value of the number of signal events for the strongest source is represented by $S1$. The highest value of the median significance corresponds to the optimum number of sources.

D.2 The multi year data set

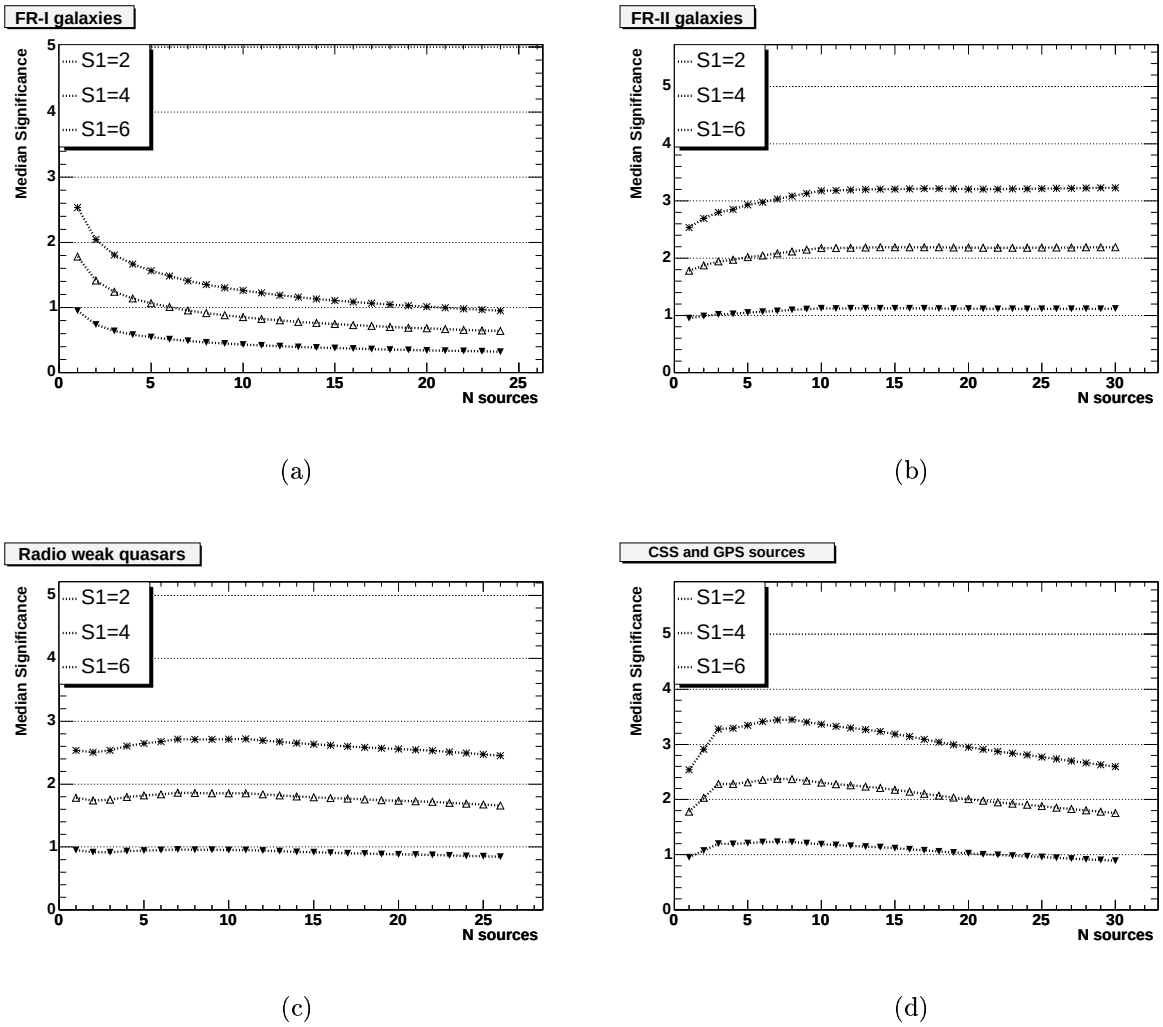

(a) (b)

(c) (d)

Figure D.4: Median significance for the multi year data set as expected under the considered hypothesis as a function of the number of AGN to be stacked. The expectation value of the number of signal events for the strongest source is represented by $S1$. The highest value of the median significance corresponds to the optimum number of sources.

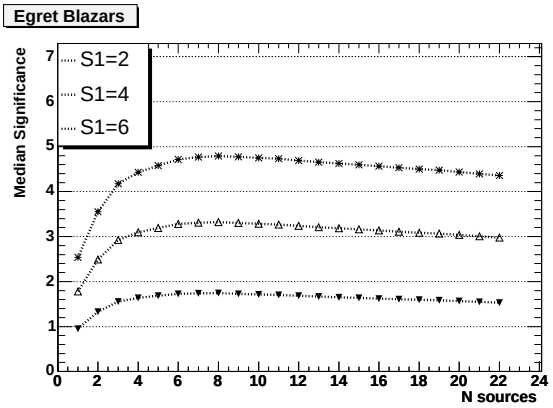

(a)

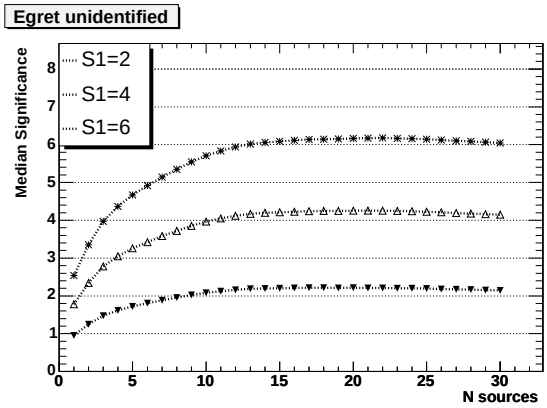

(b)

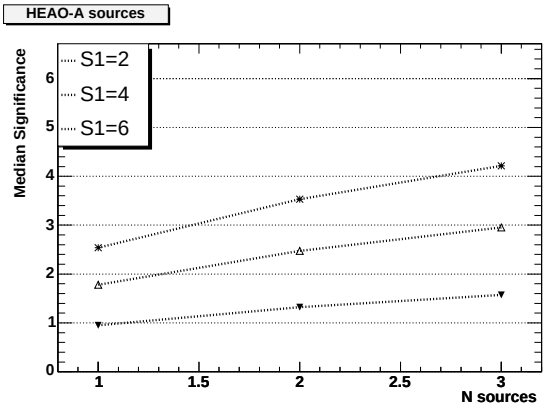

(c)

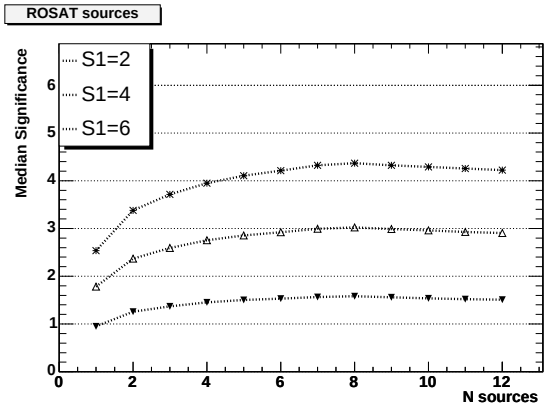

(d)

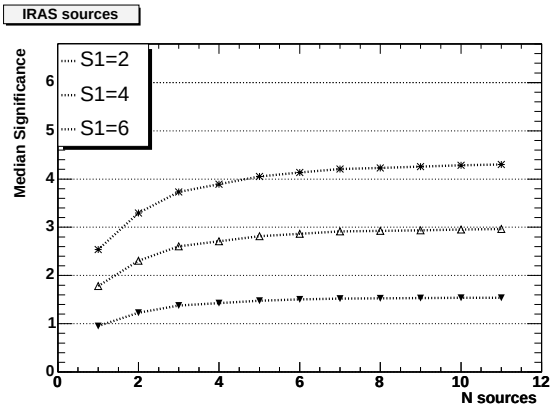

(e)

Figure D.5: Median significance for the multi year data set as expected under the considered hypothesis as a function of the number of blazars to be stacked. The expectation value of the number of signal events for the strongest source is represented by $S1$. The highest value of the median significance corresponds to the optimum number of sources.

Appendix E

Skyplots for the multi-year data set

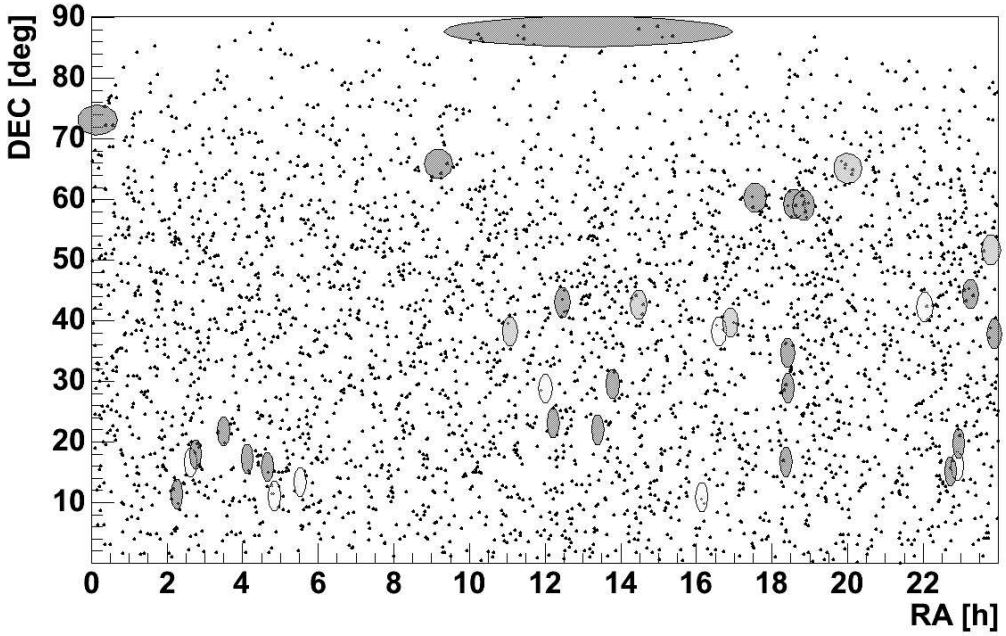

Figure E.1: RA and δ of all neutrino events in the multi-year sample. The search bins of TeV and GeV blazars are indicated by ellipses.

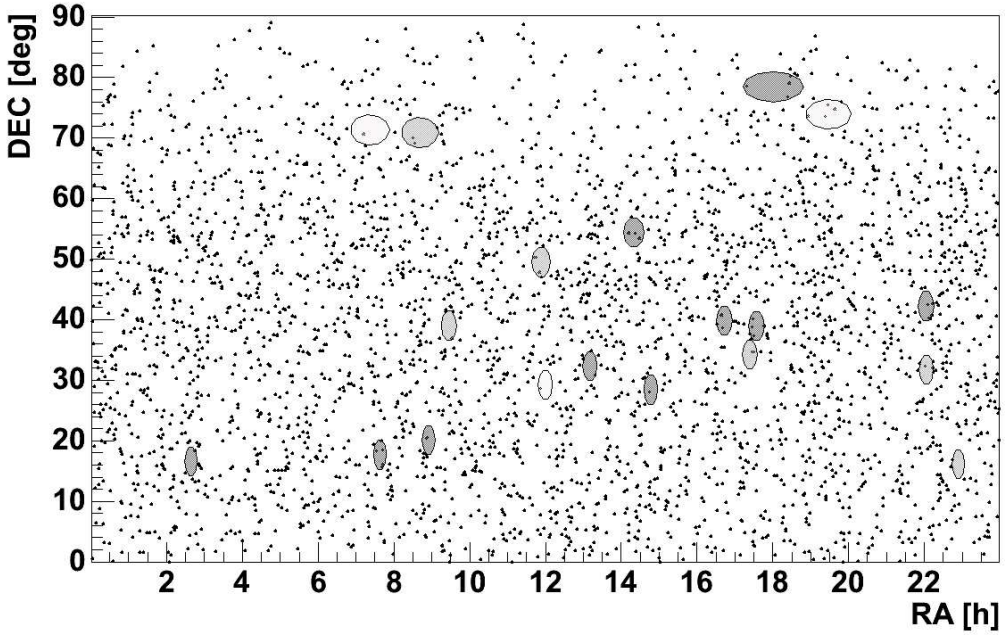

Figure E.2: RA and δ of all neutrino events in the multi-year sample. The search bins around selected keV blazars from HEAO-A and ROSAT and around IR indicated by ellipses.

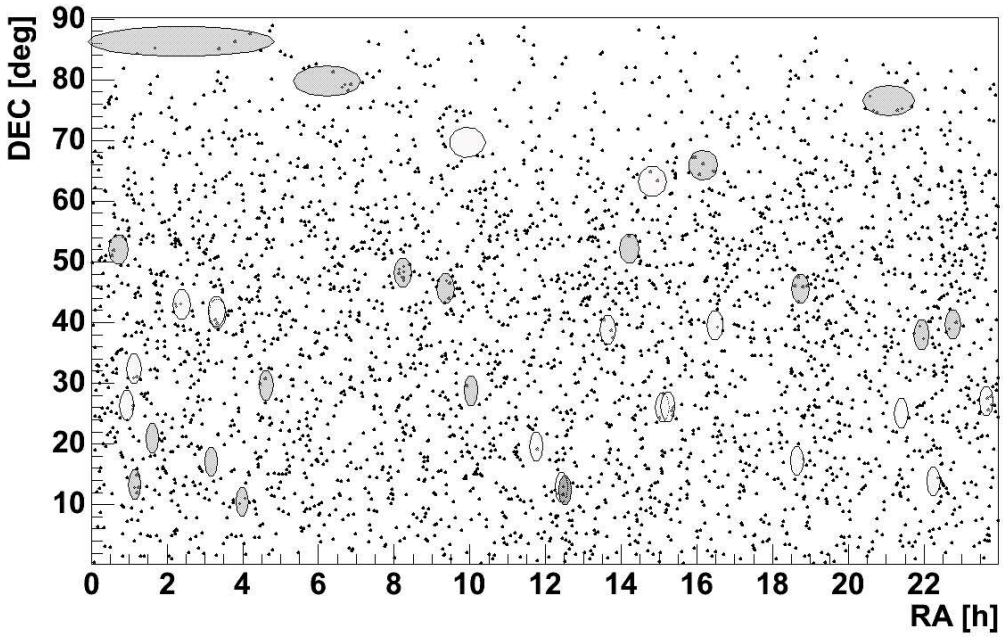

Figure E.3: RA and δ of all neutrino events in the multi-year sample. The search bins around selected FR-I and FR-II radio galaxies are indicated by ellipses.

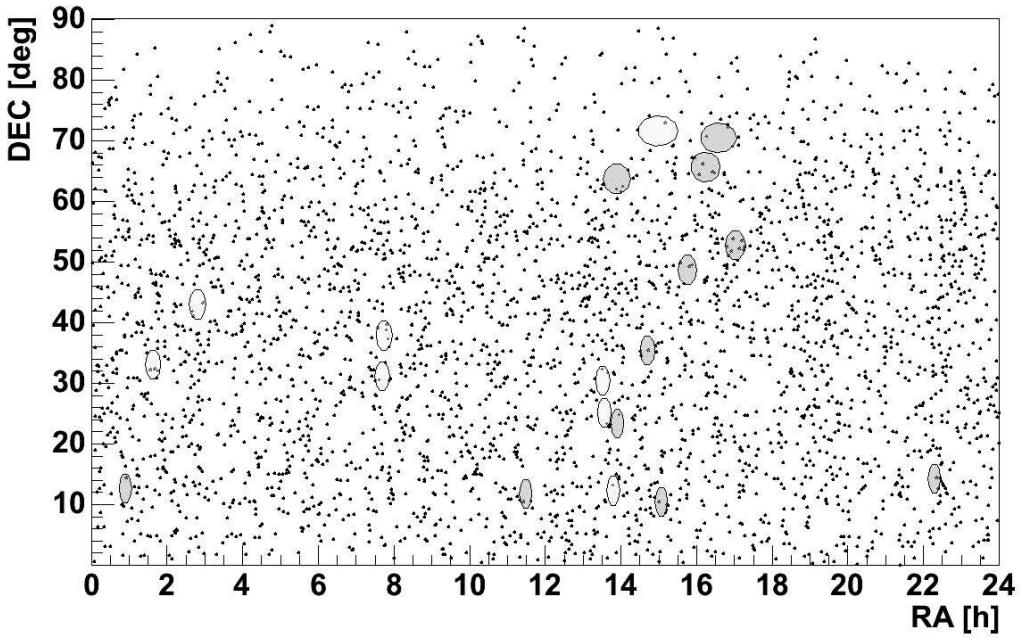

Figure E.4: RA and δ of all neutrino events in the multi-year sample. The search bins around selected GPS/CSS and QSO are indicated by ellipses.

List of Figures

List of Tables

Bibliography

[A+] M. Ackermann et al. Search for astrophysical neutrinos from steady and transient sources in the northern hemisphere using the AMANDA detector. to be published.

[A+93] D. E. Alexandreas et al. Point source search techniques in ultra high energy gamma ray astronomy. *Nuclear Instruments & Methods*, A 328:570–577, 1993.

[A+00] E. Andres et al. The AMANDA Neutrino Telescope: Principle operation and first results. *Astroparticle Physics*, 13:1–20, 2000.

[A+03a] F. Aharonian et al. Is the giant radio galaxy M87 a TeV gamma-ray emitter? *Astronomy & Astrophysics*, 403:L1–L6, 2003.

[A+03b] J. Ahrens et al. Limits on diffuse fluxes of high energy extraterrestrial neutrinos with the AMANDA-B10 detector. *Physical Review Letters*, 90:251101, 2003.

[A+04a] F. Aharonian et al. The Crab Nebula and Pulsar between 500 GeV and 80 TeV: Observations with the HEGRA stereoscopic air Cherenkov telescopes. *Astrophysical Journal*, 614:897–913, 2004.

[A+04b] J. Ahrens et al. Muon track reconstruction and data selection techniques in AMANDA. *Nuclear Instruments & Methods*, 524:169–194, 2004.

[A+04c] J. Ahrens et al. Search for extraterrestrial point sources of neutrinos with AMANDA-II. *Physical Review Letters*, 92:070201, 2004.

[A+04d] J. Ahrens et al. Sensitivity of the IceCube detector to astrophysical sources of high energy muon neutrinos. *Astroparticle Physics*, 20:507, 2004.

[A+05a] M. Ackermann et al. Multiwavelength comparison of selected neutrino point source candidates. In *Proceedings of the 29th ICRC, Pune*, 2005.

[A+05b] M. Ackermann et al. Optical properties of deep glacial ice at the south pole. *Journal of Geophysical Research*, 2005. submitted.

[A+05c] M. Ackermann et al. Search for extraterrestrial point sources of high energy neutrinos with AMANDA-II using data collected in 2000-2002. *Physical Review D*, 71:077102, 2005.

[A+05d] M. Ackermann et al. Search for high energy neutrino point sources in the northern hemisphere with the AMANDA neutrino telesope. In *Proceedings of the 29th ICRC, Pune*, 2005.

[A+05e] F. Aharonian et al. A detailed spectral and morphological study of the gamma-ray supernova remnant RX J1713.7-3946 with H.E.S.S. *ArXiv Astrophysics e-prints*, 2005.

[AM85] R.R.J. Antonucci and J.S. Miller. Spectropolarimetry and the nature of NGC 1068. *Astrophysical Journal*, 297:621–632, 1985.

[AMA] http://amanda.uci.edu.

[ANT97] ANTARES proposal: Towards a large scale high energy cosmic neutrino undersea detector. 1997, astro-ph/9707136. see also http://antares.in2p3.fr.

[Arg00] S. Argiro. *The fluorescence detector of the Pierre Auger Cosmic Ray Observatory and its readout electronics.* PhD thesis, Universita degli Studi di Milano, 2000.

[B+02] X. Bertou et al. Tau neutrinos in the Auger Observatory: a new window to UHECR sources. *Astroparticle Physics*, 17:183, 2002.

[B+03] A. Balbi et al. Probing dark energy with the cosmic microwave background: Projected constraints from the Wilkinson Microwave Anisotropy Probe and Planck. *Astrophysical Journal Letters*, 588:L5–L8, 2003.

[B+05] M. Blazejowski et al. A multi-wavelength view of the TeV blazar Markarian 421: Correlated variability, flaring, and spectral evolution. *ArXiv Astrophysics e-prints*, 2005, astro-ph/0505325. submitted to Astrophysical Journal.

[BBM05] W. Bednarek, G.F. Burgio, and T. Montaruli. Galactic discrete sources of high energy neutrinos. *New Astron.Rev.*, 49:1, 2005.

[BBR05] J. K. Becker, P. L. Biermann, and W. Rhode. The diffuse neutrino flux from FR-II radio galaxies and blazars: A source property based estimate. *Astroparticle Physics*, 23:355–368, 2005.

[Bec04] J. K. Becker. Calculation of the AGN neutrino flux and of event rates for large volume neutrino telescopes. Master's thesis, University of Wuppertal, 2004. WU D 04-06.

[Bel78a] A.R. Bell. The acceleration of cosmic rays in shock fronts. I. *Monthly Notices of the Royal Astronomical Society*, 182:147, 1978.

[Bel78b] A.R. Bell. The acceleration of cosmic rays in shock fronts. II. *Monthly Notices of the Royal Astronomical Society*, 182:443, 1978.

[Bie93] P. L. Biermann. Cosmic rays. 1. The cosmic ray spectrum between 10^4 GeV and $3 \cdot 10^9$ GeV. *Astronomy & Astrophysics*, 271:649, 1993.

[Bie04] P. L. Biermann. Cosmic rays, stellar evolution and supernova physics. *New Astronomy Reviews*, 48:41–46, 2004.

[Bla95] J. K. Blackburn. FTOOLS: A FITS Data Processing and Analysis Software Package. In *ASP Conf. Ser. 77: Astronomical Data Analysis Software and Systems IV*, pages 367–+, 1995.

[Blo84] V. Blobel. Unfolding methods in high–energy physics experiments. Proceedings of the 1984 CERN School of Computing, CERN, 1984.

[Boe05] D. Boersma. Sieglinde user manual, 2005, http://amanda.wisc.edu/software/sieglinde/usermanual/index.html.

[Boj03] H. Bojahr. *Suche nach TeV-Blazaren mit dem HEGRA-System der abbildenden Cherenkov-Teleskope*. PhD thesis, University of Wuppertal, 2003.

[BS87] P. L. Biermann and P. A. Strittmatter. Synchrotron emission from shock waves in active galactic nuclei. *Astrophysical Journal*, 322:643–649, 1987.

[BS01] P. L. Biermann and G. Sigl. Introduction to Cosmic Rays. *LNP Vol. 576: Physics and Astrophysics of Ultra-High-Energy Cosmic Rays*, 576:1–+, 2001.

[BS05] J.K. Becker and T. Stanev. private communication. 2005.

[BTV95] M. Barone, G. Tsorbatzoglou, and G. Vekinis. Nestor: an underwater cerenkov detector for neutrino astronomy. In G. Pizzella E. Coccia and F. Ronga, editors, *First Edoardo Amaldi Conference on Gravitational Wave Experiments, Villa Tuscolana, Frascati, Rome, 14-17 June 1994*, page 288. World Scientific, 1995.

[C+00] M. Cappi et al. A qualitative test of a unified model of Seyfert galaxies with Bepposax. *Advances in Space Research*, 25:815–818, 2000.

[C+02] D.F. Cowen et al. Results from the Antarctic Muon and Neutrino Detector Array. *ArXiv Astrophysics e-prints*, 2002, astro-ph/0211264.

[C+03] J. Conrad et al. Including systematic uncertainties in confidence interval construction for poisson statistics. *Physical Review D*, 67:012002, 2003.

[C+05] W. Cui et al. News from a multi-wavelength monitoring campaign on mrk 421. In F.A. Aharonian, H.J. Völk, and D. Horns, editors, *High Energy Gamma-Ray Astronomy: 2nd International Symposium, AIP Conference Proceedings*, volume 745, pages 455–461, 2005.

[Cao03] Z. Cao. The Physics Results from HiRes Fly's Eye Experiment. In *Very High Energy Phenomena in the Universe*, page 205, 2003.

[Caw90] M.F. Cawley. A high resolution imaging detector for TeV gamma-ray astronomy. *Experimental Astronomy*, 1:173–193, 1990.

[CGR] http://cossc.gsfc.nasa.gov/.

[CH05] A.N. Cillis and R.C. Hartman. EGRET diffuse gamma-ray maps between 30 MeV and 10 GeV. *Astrophysical Journal*, 621:291–295, 2005.

[CHB04] A.N. Cillis, R.C. Hartman, and D.L. Bertsch. Stacking searches for gamma-ray emission above 100 MeV from radio and seyfert galaxies. *Astrophysical Journal*, 601:142–150, 2004.

[Chi] D. Chirkin, http://amanda.berkeley.edu/~dima/work/CORSIKA/.

[CO96] B.W. Carroll and D.A. Ostlie. *Modern Astrophysics*. Addison Wesley, 1996.

[Cos01] C.G.S. Costa. The prompt lepton cookbook. *Astroparticle Physics*, 16:193–204, 2001.

[CPL92] S. M. Carroll, W. H. Press, and E. L.Turner. The cosmological constant. *Ann. Rev. Astron. Astrophys.*, 30:499, 1992.

[CR04] D. Chirkin and W. Rhode. Muon monte carlo: a high-precision tool for muon propagation through matter. *ArXiv Astrophysics e-prints*, 2004, hep-ph/0407075.

[CTR05] A.N. Cillis, D.F. Torres, and O. Reimer. Egret upper limits and stacking searches of gamma-ray observations of luminous and ultra-luminous infrared galaxies. *Astrophysical Journal*, 2005.

[DB02] G.V. Domogatskii and Baikal Collaboration. Status of the BAIKAL neutrino project. 2002, astro-ph/0211571.

[DGWL02] C. Distefano, D. Guetta, E. Waxman, and A. Levinson. Neutrino flux predictions for known galactic microquasars. *Astrophysical Journal*, 575:378–383, 2002.

[DR+95] K. Daum, W. Rhode, et al. Determination of the atmospheric neutrino spectra with the Fréjus detector. *Zeitschrift für Physik C*, 66:177, 1995.

[Dre03] M. Drees. The top-down interpretation of ultra-high energy cosmic rays. 2003, hep-ph/0310331. invited talk at VHEPA-3, ICRR, Tokyo, March 2003.

[Dre05] J. Dreyer. Hard- und Softwareentwicklung im Rahmen der Experimente AMANDA und IceCube. Master's thesis, University of Dortmund, 2005.

[F+90] R. Fanti et al. On the nature of compact steep spectrum radio sources. *Astronomy & Astrophysics*, 231:333–346, 1990.

[FB95] H. Falcke and P. L. Biermann. The jet-disk symbiosis. I. Radio to X-ray emission models for quasars. *Astronomy & Astrophysics*, 293:665, 1995.

[FC98] G. J. Feldman and R. D. Cousins. A unified approach to the classical statistical analysis of small signals. *Physical Review D*, 57:3873–3889, 1998.

[Fer49] E. Fermi. On the origin of the cosmic radiation. *Physical Review*, 75:1169, 1949.

[FGKB95] H. Falcke, Gopal-Krishna, and P. L. Biermann. Unified schemes for active galaxies: a clue from the missing Fanaroff-Riley type I quasar population. *Astronomy & Astrophysics*, 298:395, 1995.

[FMB95] H. Falcke, M. A. Malkan, and P. L. Biermann. The jet-disk symbiosis. II. Interpreting the Radio/UV correlations in quasars. *Astronomy & Astrophysics*, 298:375, 1995.

[FR74] B. L. Fanaroff and J. M. Riley. The morphology of extragalactic radio sources of high and low luminosity. *Monthly Notices of the Royal Astronomical Society*, 167:31–36, 1974.

[FSP96] H. Falcke, W. Sherwood, and A.R. Patnai. The nature of radio-intermediate quasars: What is radio-loud and what is radio-quiet? *Astrophysical Journal*, 471:106, 1996.

[G+00] H. Gehrels et al. Discovery of a new population of high-energy γ-ray sources in the milky way. *Nature*, 404:363–365, 2000.

[G+03] H. Geenen et al. Atmospheric neutrino and muon spectra measured with the AMANDA-II detector. In *Proceedings of the 28th Int. Cosmic Ray Conf.*, page 1313, 2003.

[G+05a] J. Gorosabel et al. The short-duration grb 050724 host galaxy in the context of the long-duration grb hosts. *ArXiv Astrophysics e-prints*, 2005, astro-ph/0510141.

[G+05b] A. Groß et al. Recent results from the AMANDA-II neutrino telescope. In *Proccedings of th 40th Rencontrees de Moriond - Electro-weak interaction and unified theories*, 2005, astro-ph/0505278.

[Gai90] Thomas K. Gaisser. *Cosmic Rays and Particles.* Cambridge University Press, 1990.

[Gan98] R. Gandhi. Neutrino interations at ultrahigh energies. *Physical Review D*, 58:093009, 1998.

[Gee02] H. Geenen. Energy reconstruction and spectral unfolding of atmospheric leptons with the AMANDA detector. Master's thesis, BU Wuppertal, 2002.

[GM96] P. Goldoni and C. Musso. Isolated neutron stars, their efficiencies and EGRET observations. *Astronomy and Astrophysics Supplement*, 120:103, 1996.

[GM99] N. Gehrels and P. Michelson. GLAST: the next-generation high energy gamma-ray astronomy mission. *Astroparticle Physics*, 11, 1999.

[Gre66] K. Greisen. End to the Cosmic-Ray Spectrum? *Physical Review Letters*, 16, 1966.

[Gru93] C. Grupen. *Teilchendetektoren.* B.I. Wissenschaftsverlag, 1993.

[H+95] M. Honda et al. Calculation of the flux of atmospheric neutrinos. *Physical Review D*, 52:4985, 1995.

[H+98] D. Heck et al. A Monte Carlo code to simulate extensive air showers. *Wissenschaftlicher Bericht FZKA 6019*, 1998.

[H+99] R. C. Hartman et al. The third EGRET catalog of high-energy gamma-ray sources. *Astrophysical Journal*, Suppl. Ser. 123:79–202, 1999.

[H+01] G.C. Hill et al. The SiEGMuND software package. 2001, http://amanda.wisc.edu/software/siegmund/.

[H+02a] D. Horan et al. Detection of the BL Lacertae Object H1426+428 at TeV Gamma-Ray Energies. *Astrophysical Journal*, 571:753–762, June 2002.

[H+02b] D. Horns et al. Multi-wavelength observations of the TeV Blazars Mkn 421, 1ES1959+650, and H1426+428 with the HEGRA Cherenkov telescopes and the RXTE X-ray satellite. In *Proceedings for "High Energy Blazar astronomy", Turku, Finland*, 2002.

[H+03] R. Hardtke et al. Searching for high energy muon neutrinos from gamma-ray bursts with AMANDA. In *Proceedings of the 28th Int. Cosmic Ray Conf.*, 2003.

[H+05a] A. Haungs et al. Investigating the 2nd knee: The KASCADE-Grande experiment. 2005, astro-ph/0508286. Invited talk at the "Workshop on Physics of the End of the Galactic Cosmic Ray Spectrum", Aspen, USA, April 25 - 29, 2005.

[H+05b] J. Hjorth et al. GRB 050509B: Constraints on short gamma-ray burst models. *Astrophysical Journal Letters*, 630:L117, 2005.

[Hau04] T. Hauschildt. *Search for Cosmic Point Sources of High Energy Neutrinos with the AMANDA-II Detector*. PhD thesis, Humboldt-Universitĺat zu Berlin, 2004.

[Hil84] A. M. Hillas. The Origin of Ultra-High-Energy Cosmic Rays. *Ann. Rev. Astron. Astrophys.*, 22:425, 1984.

[Hil96] G. Hill. *Experimental and Theoretical Aspects of High Energy Neutrino Astrophysics*. PhD thesis, University of Adelaide, 1996.

[HR03] G. C. Hill and K. Rawlins. Unbiased cut selection for optimal upper limits in neutrino detectors: the model rejection potential technique. *Astroparticle Physics*, 19:393–402, June 2003.

[HS02] S. Heinz and R.A. Sunyaev. Cosmic rays from microquasars: a narrow component to the cr spectrum? *Astronomy & Astrophysics*, 390:751–766, 2002.

[Hun99] S. Hundertmark. AMASIM neutrino detector simulation program. In C. Spiering, editor, *Proceedings of Workshop on Simulation and Analysis Methods for Large Neutrino Telescopes*, page 276, Zeuthen (Germany), 1999.

[Jac62] John David Jackson. *Classical Electrodynamics*. John Wiley & Sons Inc., 1962.

[K+81a] H. Kühr et al. A catalogue of radio sources. *MPIfR Preprint*, 55, 1979/1981.

[K+81b] H. Kühr et al. A catalogue of extragalactic radio sources having flux densities greater than 1 Jy at 5 GHz. *Astronomy and Astrophysics Supplement*, 45:367–430, 1981.

[K+81c] H. Kühr et al. The 5-GHz strong source surveys. V - Survey of the area between declinations 70 and 90 deg. *Astronomical Journal*, 86:854, 1981.

[K+04] H. Krawczynsk et al. Multiwavelength observations of strong flares from the TeV-blazar 1ES 1959+650. *Astrophysical Journal*, 601:151–164, 2004.

[K+05] J.A. Kollmeier et al. Black hole masses and eddington ratios at $0.3<z<4$. *ArXiv Astrophysics e-prints*, 2005, astro-ph/0508657. Submitted to ApJ.

[KM3] http://www.km3net.org.

[Kon99] A. Konopelko. Performance of the stereoscopic system of the HEGRA imaging air Čerenkov telescopes: Monte Carlo simulations and observations. *Astroparticle Physics*, 10:275–289, 1999.

[L+83] R.A. Laing et al. Bright radio sources at 178 MHz - flux densities, optical identifications and the cosmological evolution of powerful radio galaxies. *Monthly Notices of the Royal Astronomical Society*, 204:151–187, 1983.

[L+99] Y. C. Lin et al. EGRET Spectral Index and the Low-Energy Peak Position in the Spectral Energy Distribution of EGRET-detected Blazars. *Astrophysical Journal*, 525:191, 1999.

[Lip93] P. Lipari. Lepton spectra in the earth's atmosphere. *Astroparticle Physics*, 1:195–227, 1993.

[LM83] T.-P. Li and Y.-Q. Ma. Analysis methods for results in gamma-ray astronomy. *Astrophysical Journal*, 272:317–324, 1983.

[LM00] J. G. Learned and K. Mannheim. High-energy neutrino astrophysics. *Annu. Rev. Nucl. Part. Sci.*, 50:679–749, 2000.

[Lon92] M.S. Longair. *High Energy Astrophysics*, volume 1. Cambridge University Press, 1992.

[M+90] M. Moshir et al. IRAS faint source catalogue, version 2.0. *Bulletin of the American Astronomical Society*, 22, 1990.

[M+02] S.S. Murray et al. Discovery of X-Ray Pulsations from the Compact Central Source in the Supernova Remnant 3C 58. *Astrophysical Journal*, 568:226, 2002.

[M+03] T. Montaruli et al. ANTARES status report. In *Proceedings of 28th International Cosmic Ray Conference (ICRC 2003)*, 2003.

[M+05a] T. Messarius et al. A software-trigger for the AMANDA neutrino detector. In *Proceedings of the 29th ICRC, Pune*, 2005.

[M+05b] K. Münich et al. Search for a diffuse flux of non-terrestrial muon neutrinos with the AMANDA detector. In *Proceedings of the 29th ICRC, Pune*, 2005.

[Man95] K. Mannheim. High-energy neutrinos from extragalactic jets. *Astroparticle Physics*, 3:295, 1995.

[Man97] K. Mannheim. AGN models: High-energy emission. 1997. Review talk given at the XXXIInd Rencontres de Moriond, "Very High Energy Phenomena in the Universe", Les Arcs, France.

[Man99] K. Mannheim. Frontiers in high-energy astroparticle physics. *Reviews in Modern Astronomy*, 12:167, 1999, astro-ph/9902185.

[MB] A. Meli and P.L. Biermann. CR X. The cosmic ray knee and beyond: Diffusive shock acceleration at oblique shocks. To be published.

[MH96] D.A. Moffett and T.H. Hankins. Multifrequency radio observations of the crab pulsar. *Astrophysical Journal*, 468:779, 1996.

[Mir01] I. F. Mirabel. Microquasars: A major topic for INTEGRAL. In A. Gimenez, V. Reglero, and C. Winkler, editors, *Exploring the gamma-ray universe. Proceedings of the 4th INTEGRAL workshop, 4-8 September 2000, Alicante, Spain*, pages 249–253, 2001.

[Mir02] I. F. Mirabel. Microquasars as sources of high energy phenomena, invited review at the iau symposium no.214: High energy processes and phenomena in astrophysics. 2002. astro-ph/0211085.

[MP01a] A. Mücke and R. J. Protheroe. A Proton Synchrotron Blazar Model for Flaring in Markarian 501. *Astroparticle Physics*, 15:121–136, 2001.

[MP01b] A. Mücke and R. J. Protheroe. Neutrino emission from HBLs and LBLs. In *Proc. 27th Int. Cosmic Ray Conf*, 2001.

[MPR01] K. Mannheim, R. J. Protheroe, and J. P. Rachen. On the cosmic ray bound for models of extragalactic neutrino production. *Physical Review D*, 63:023003, 2001.

[MRS03] A. D. Martin, M.G. Ryskin, and A.M. Stasto. Prompt neutrinos from $c\bar{c}$ and $b\bar{b}$ and the gluon at very small x. *Acta Phys.Polon. B*, 34:3273–3304, 2003.

[MWMF96] K. Mannheim, S. Westerhoff, H. Meyer, and H.-H. Fink. Beacons at the gamma ray horizon. *Astronomy & Astrophysics*, 315:77–85, November 1996.

[NED] NASA Extragalactic Database, http://nedwww.ipac.caltech.edu/.

[NEM] Nemo. http://nemoweb.lns.infn.it.

[Neu04] T. Neunhöffer. Estimating the angular resolution of tracks in neutrino telescopes based on a likelihood analysis. *ArXiv Astrophysics e-prints*, 2004.

[NMB93] L. Nellen, K. Mannheim, and P. L. Biermann. Neutrino production through hadronic cascades in AGN accretion disks. *Physical Review D*, 47:5270, June 1993.

[OB97] C. P. O'Dea and S. A. Baum. Constraints on radio source evolution from the Compact Steep Spectrum and GHz Peaked Spectrum radio sources. *Astronomical Journal*, 113:148–161, 1997.

[O'D98] C. P. O'Dea. The Compact Steep-Spectrum and Gigahertz Peaked-Spectrum Radio Sources. *The Publications of the Astronomical Society of the Pacific*, 110:493, 1998.

[OUS02] M. O'Dowd, C. M. Urry, and R. Scarpa. The host galaxies of radio-loud AGN: The black hole galaxy connection. *Astrophysical Journal*, 580:96–103, 2002.

[P+72] I. I. K. Pauliny-Toth et al. The NRAO 5-GHz radio source survey. II. The 140-ft "Strong", "Intermediate", and "Deep" source surveys. *Astronomical Journal*, 77:265, 1972.

[P+78] I. I. K. Pauliny-Toth et al. The 5 GHz strong source surveys. IV - Survey of the area between declination 35 and 70 degrees and summary of source counts, spectra and optical identifications. *Astronomical Journal*, 83:451, 1978.

[PDR03] R.J. Protheroe, A.-C. Donea, and A. Reimer. TeV gamma rays and cosmic rays from the nucleus of M87, a mis-aligned BL Lac object. *Astroparticle Physics*, 19:559–568, 2003.

[PK72] I. I. K. Pauliny-Toth and K. I. Kellermann. The NRAO 5-GHz radio source survey. III. The 140-ft "strong" source survey. *Astronomical Journal*, 77:797, 1972.

[PM99] D. Petry and MAGIC Telescope Collaboration. The MAGIC Telescope - prospects for GRB research. *Astronomy and Astrophysics Supplement*, 138:601, 1999.

[Pro98] R. J. Protheroe. Origin and Propagation of the Highest Energy Cosmic Rays. In *Towards the Millennium in Astrophysics, Problems and Prospects. International School of Cosmic Ray Astrophysics 10th Course*, page 3, 1998, astro-ph/9612212.

[R+04a] G.E. Romero et al. Unidentified gamma-ray sources and microquasars. *astro-ph/0402285*, 2004. Paper presented at the fifth INTEGRAL workshop.

[R+04b] A. H. Rots et al. Absolute timing of the Crab Pulsar with RXTE. *Astrophysical Journal*, 605:L129–L132, 2004.

[RC01] W. Rhode and D. Chirkin. Muon monte carlo: a new high-precision tool for tracking of muons in medium. In *Proceedings of the 27th International Cosmic Ray Conference. Hamburg, Germany.*, 2001.

[RD+96] W. Rhode, K. Daum, et al. Limits on the flux of very high energy neutrinos with the Fréjus detector. *Astroparticle Physics*, 4:217–225, 1996.

[RT90] M.T. Ressell and M.S. Turner. The grand unified photon spectrum: A coherent view of the diffuse extragalactic background radiation. *Bulletin of the American Astronomical Society*, 22:753, 1990. FERMILAB-PUB-89-214-A.

[S+85] H. Spinrad et al. A third update of the status of the 3CR sources - further new redshifts and new identifications of distant galaxies. *The Publications of the Astronomical Society of the Pacific*, 97:932–961, 1985.

[S+89] D.B. Sanders et al. Continuum energy distribution of quasars - shapes and origins. *Astrophysical Journal*, 347:29–51, 1989.

[S+91] F. W. Stecker et al. High-energy neutrinos from active galactic nuclei. *Physical Review Letters*, 66:2697–2700, 1991.

[S+98] C. Stanghellini et al. A complete sample of GHz-peaked-spectrum radio sources and its radio properties. *Astronomy and Astrophysics Supplement*, 131:303–315, 1998.

[S+03] D. N. Spergel et al. First year Wilkinson Microwave Anisotropy Probe (WMAP) observations: Determination of cosmological parameters. *Astrophysical Journal*, Suppl. 148:175, 2003.

[Sch02] T. Schmidt. *Aufbau und Funktionsnachweis eines Optischen Moduls mit optisch-analoger Pulsübertragung für den AMANDA–II– und ICECUBE– Detektor*. PhD thesis, Humboldt Universität Berlin, Germany, 2002.

[SERM03] D. Sowards-Emmerd, R. W. Romani, and P. F. Michelson. The Gamma-Ray Blazar Content of the Northern Sky. *Astrophysical Journal*, 590:109–122, 2003.

[SG83] M. Schmidt and R.F. Green. Quasar evolution derived from the Palomar Bright Quasar Survey and other complete samples. *Astrophysical Journal*, 269:352–374, 1983.

[SMR04] A. W. Strong, I. V. Moskalenko, and O. Reimer. Diffuse Galactic Continuum Gamma Rays: A Model Compatible with EGRET Data and Cosmic-Ray Measurements. *Astrophysical Journal*, 613:962–976, October 2004.

[SS96] F. W. Stecker and M. H. Salamon. High energy neutrinos from quasars. *Space Sci.Rev.*, 75:341–355, 1996.

[Sta04] T. Stanev. *High Energy Cosmic Rays*. Springer, 2004.

[Ste00] R. Steenkamp. H.E.S.S. - An Array of Gamma Ray Telescopes in Namibia. *African Skies*, 5:6, 2000.

[Tab02] I. Taboada. *Search for High Energy Neutrino Induced Cascades*. PhD thesis, University of Pennsylvania, 2002.

[Tas04] O. Tascău. The nearby black holes as sources of ultra high energy cosmic rays. Master's thesis, Bonn, 2004.

[TC05] F. Tegenfeldt and J. Conrad. On baysian treatment of systematic uncertainties in confidence interval calculation. *Nuclear Instruments & Methods*, 539:407–413, 2005.

[UP95] C.M. Urry and P. Padovani. Unified schemes for radio-loud Active Galactic Nuclei. *The Publications of the Astronomical Society of the Pacific*, 107:803–845, 1995.

[V+99] W. Voges et al. The ROSAT all-sky survey bright source catalogue. *Astronomy & Astrophysics*, 349:389–405, 1999.

[V+05] J. S. Villasenor et al. Discovery of the short γ-ray burst GRB 050709. *Nature*, 437:855, 2005.

[VZ80] L.V. Volkova and G.T. Zatsepin. Prompt lepton generation-atmospheric muon and neutrino spectra at high-energies. *Soviet Journal of Nuclear Physics*, 37:212, 1980.

[W+84] K.S. Wood et al. The HEAO A-1 X-ray source catalog. *Astrophys.J.Suppl. Ser.*, 56:507–649, 1984.

[W+02] T. Weekes et al. VERITAS: the Very Energetic Radiation Imaging Telescope Array System. *Astroparticle Physics*, 17:221–243, 2002.

[W+04] K. Woschnagg et al. New results from the Antarctic Muon And Neutrino Detector Array. In *Proceedings of the XXIst International Conference on Neutrino Physics and Astrophysics, Paris*, 2004.

[Wag04] W. Wagner. *Design and Realisation of a new AMANDA Data Acquisition System with Transient Waveform Recorders.* PhD thesis, Uni Dortmund, 2004.

[Wal00] H.J. Walker. A brief history of infrared astronomy. *Astronomy & Geophysics*, 41:10, 2000.

[WB97] E. Waxman and J. Bahcall. High Energy Neutrinos from Cosmological Gamma-Ray Burst Fireballs. *Physical Review Letters*, 78:2292, 1997.

[Wee03a] T.C. Weekes. TeV Gamma-ray Observations and the Origin of Cosmic Rays: I. *ArXiv Astrophysics e-prints*, 2003, astro-ph/0312179. Planary talk held at the 28th Int. Cosmic Ray Conf.

[Wee03b] T.C. Weekes. *Very high energy gamma-ray astronomy.* Institue of Physics Publishing, Bristol and Philadelphia, 2003.

[Wie98] B. Wiebel-Sooth. *Measurement of the allparticle energy spectrum and chemical composition of cosmic rays with the HEGRA detector.* PhD thesis, University of Wuppertal, 1998.

[Y+95] S. Yoshida et al. The cosmic ray energy spectrum above 3x10^18 eV measured by the Akeno Giant Air Shower Array. *Astroparticle Physics*, 3:105, 1995.

[ZK66] G.T. Zatsepin and V.A. Kuzmin. Upper limit of the spectrum of cosmic rays. *JETP Lett.*, 4:78, 1966.

[ZM04] B. Zhang and P. Mészáros. Gamma-Ray Bursts: progress, problems and prospects. *International Journal of Modern Physics A*, 19:2385–2472, 2004.

Acknowledgement

I would like to acknowledge to all people who contributed to the success of this thesis. There are many, so I probably could not mention everybody personally.

Especially, I would like to thank Prof. Dr. Dr. Wolfgang Rhode for the possibility to compose this thesis. He gave very important advice in all central issues of this thesis in the wide range from theoretical concepts to experimental techniques.

I am grateful to Prof. Dr. P.L. Biermann for many enlightning discussions about Active Galactic Nuclei. In particular, he gave great support concerning the selection of astronomical source catalogs.

I acknowledge to Prof. Dr. B. Spaan for time and effort he took for evaluating this thesis as the second referee.

I have to thank everybody in the IceCube collaboration who supported this work. In particular, Prof. Dr. Francis Halzen encouraged me to follow the ansatz of this thesis. Furthermore, I had many interesting discussions about the phenomenological approach with Elisa Resconi.

I feel thankful to all members of the Dortmund Astroparticle Physics group for their continous support.

I would like to thank Julia Becker for many interesting discussions on AGN physics. Special thanks go to Kirsten Münich and to Klaus Münich for their never-failing advice concerning the presentation of scientific results. Wolfgang Wagner contributed to the success of this thesis in various ways. I am particularly grateful that he generously lent me his laptop whenever I needed it. I have to thank Athina Meli for several helpful suggestions, e.g., concerning the description of particle acceleration.

I would like to thank my room mates, Valentin Curtef, Timo Messarius and Frank Refflinghaus, for the nice atmosphere in the office.

I acknowledge the support of Matthias Bartelt, Vanessa Cirkel, Jens Dreyer, Dominik Leier and Jan Lünemann who helped me to find errors in the draft of this thesis.

Finally, I would like to thank my parents, Marlies Groß and Klaus Groß, and my sister, Kirstin Groß, for their emotional support during the last three years.